Section C

MECHANICS OF SOLID BODIES

THIN-WALLED OPEN-SECTION BEAMS – ONE VIEW TO THE OPTIMIZATION ACCORDING TO STRESS CONSTRAINTS

N. Anđelić[1], V. Milošević-Mitić[1], T. Maneski[1]

[1] Faculty of Mechanical Engineering,
The University of Belgrade, Kraljice Marije 16, 11120 Belgrade 35
e-mail: nandjelic@mas.bg.ac.rs
           vmilosevic@mas.bg.ac.rs
           tmaneski@mas.bg.ac.rs

Abstract. One approach to the optimization of the thin-walled cantilever open sections beams subjected to complex loads - bending and constrained torsion, are considered. In most structures, it is possible to find the elements in which, depending on loading cases and the way of their introductions, the effect of constrained torsion is present and its consequences are particularly evident in the case of thin-walled profiles. The problem is reduced to the determination of minimum mass i.e. minimum cross-sectional area of structural thin-walled I-beam and Z-beam elements for given loads, material and geometrical characteristics. The area of the cross-section is assumed to be the objective function. The stress constraints are introduced. Applying the Lagrange multiplier method, the equations, which solutions represent the optimal values of the ratios of the parts of the chosen cross-section, are formed. The obtained results are used for numerical calculation.

1. Introduction

In most structures it is possible to find the elements in which, depending on loading cases and the way of their introductions, the effect of constrained torsion is present and its consequences are particularly evident in the case of thin-walled profiles. The most prominent contributor to the development of this theory was S.P.Timoshenko [1]. Kollbruner and Hajdin [2, 3] expanded the field of thin-walled structures by a range of their works. V.Z.Vlasov [4, 5] also contributed largely to the theory of thin-walled structures by developing the theory of thin-walled open section beams. Thin-walled open section beams are widely applied due to their low weight in many structures.

Among the authors who developed theoretical fundamentals of the optimization method, Fox [6], Brousse [7] and Prager [8] should be given the most prominent place. Also, Fletcher [9] and Bertsekas [10] should be mentioned as the authors of some recent developments in optimization approaches. Many studies have been conducted on the optimization problems, treating the cases where geometric configurations of structures are specified and only the dimensions of members, such as areas of members cross-sections, are determined in order to attain the minimum structural weight or cost. Many authors, Farkas [11] being among them too, applied mathematical problems of the conditional extreme of the function with more variables onto the cross-sectional area of the structure and defined optimum cross-section from the aspect of load and consumption of the material. Then, a series of works appear where the problem of optimization of various

cross-sections, such as triangular cross-section [12], I-section [13, 14], channel-section beams [15], Z-section [16], are solved by using the Lagrange multiplier method.

The main purpose of this paper is to present one approach to the optimization of a thin-walled I-section and Z-section beams.

1. Definition of the problem

During the process of dimensioning of a structure, it is often very important to find the optimal values of the dimensions. The starting points during the formulation of the basic mathematical model are the assumptions of the thin-walled-beam theory, on one side, and the basic assumptions of the optimum design, on the other.

The I-section and the Z-section beams as very often used thin-walled profiles in steel structures are considered in the present paper as the objects of the optimization. The formulation is restricted to the stress analysis of thin-walled beams with open sections. The I-section of the considered cantilever beam (Fig. 1a) with principal centroidal axes X_i (i = 1, 2) have the axis of symmetry. The Z-cross-section (Fig. 2b, c) has the centre and not the axis of symmetry. It is assumed that its flanges have equal widths $b_1 = b_3$, and thicknesses $t_1 = t_3$, and that its web has the width b_2 and thickness t_2. The ratios of thicknesses and widths of flanges and web are treated as not constant quantities.

a)   b)   c)
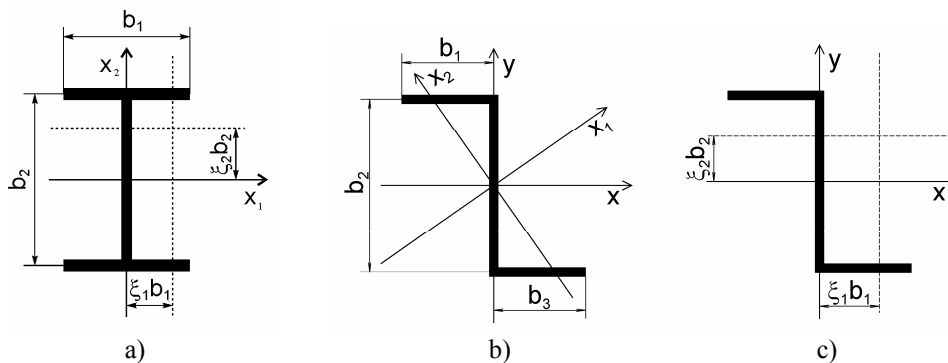
Figure 1. a) I-section; b) Z-section

It is also assumed that the loads are applied in two longitudinal planes, parallel to the longitudinal centroidal axes at the distances $\xi_i b_i$ (i = 1,2) (Fig. 1a,c). If applied in such a way, the loads will cause the bending moments acting in the above mentioned two planes parallel to the longitudinal axis of the beam, and as their consequence the effects of the constrained torsion will appear in the form of the bimoment causing the stresses that depend on the boundary conditions [2, 17].

The aim of the paper is to determine the minimal mass of the beam or, in other words, to find the minimal cross-sectional area

$$A = A_{\min} \tag{1}$$

for the given loads and material and geometrical properties of the considered beam, while satisfying the constraints.

Formulation of the structural design optimization problem plays an important role in the numerical solution process [6].

2.1   Objective function

The process of selecting the best solution from various possible solutions must be based on a prescribed criterion known as the objective function. In the considered problem the cross-sectional area will be treated as an objective function and it is obvious from the Fig. 1 that

$$A = \sum b_i t_i, \quad i = 1,2,3, \tag{2}$$

or (because $b_1 = b_3$)

$$A = A (b_1, b_2) = 2\, b_1\, t_1 + b_2\, t_2 .$$

The ratios of thickness and length of the cross-sectional walls are assumed to be non-constant variables (Fig.1)

$$\frac{t_i}{b_i} \neq const, \quad i = 1,2,3, \tag{3}$$

where b_i and t_i are widths and thicknesses of the parts of the considered cross-sections.

2.2   Constraints

Only normal stresses will be taken into account in the consideration that follows and the constraints treated in the paper are the stress constraints.

The cross-section of the considered Z-beam (Fig. 1b,c) with principal centroidal axes X_i (i = 1, 2) has the center and not the axis of symmetry and because of that, the expressions (4) for equivalent bending moments $\overline{M_x}$ and $\overline{M_y}$ [16] taking into account the influence of the bending moments around centroidal axes x and y, denoted as M_x and M_y respectively, will be used

$$\overline{M_x} = \frac{M_x - M_y\left(\dfrac{I_{xy}}{I_y}\right)}{1 - \dfrac{I_{xy}^2}{I_x \cdot I_y}}, \qquad\qquad \overline{M_y} = \frac{M_y - M_x\left(\dfrac{I_{xy}}{I_x}\right)}{1 - \dfrac{I_{xy}^2}{I_x \cdot I_y}}, \tag{4}$$

where I_x, I_y are the moments of inertia of the cross-sectional area about the centroidal axes x and y, and I_{xy} is the product of inertia.

The normal stresses are caused by the bending moments M_{X1} and M_{X2} in the case of the I-section beam, odnosno $\overline{M_x}$ and $\overline{M_y}$ in the case of the Z-section beam, and by the bimoment B that appears in the case of constrained torsion. The normal stresses caused by the bending moments will be denoted as σ_{X1} and σ_{X2}, for the I-section, odnosno $\overline{\sigma_x}$ and $\overline{\sigma_y}$ for the Z-section beam, respectively. The normal stresses caused by the bimoment will be denoted as σ_ω [2, 17].

In the case when the bending moments are acting in planes parallel to the longitudinal axis (Fig. 1) at the distances $\xi_i b_i$ (i=1, 2) the bimoment as their consequence will appear and it can be expressed as the function of the bending moments and the eccentricities of their planes $\xi_i b_i$ (i=1, 2) in the following way [2, 17]

- for the I-section beam: $B = \xi_1 b_1 M_{X1} + \xi_2 b_2 M_{X2}$, (5)

and

- for the Z-section beam: $B = \xi_1 b_1 \overline{M_x} + \xi_2 b_2 \overline{M_y}$. (6)

For the allowable stress σ_0 the constraint function can be written as

- for the I-section beam: $\varphi = \varphi(\sigma) = \sigma_{X1\max} + \sigma_{X2\max} + \sigma_{\omega\max} \leq \sigma_0$ (7)

and

- for the Z-section beam: $\varphi = \varphi(\sigma) = \overline{\sigma_x}_{\max} + \overline{\sigma_y}_{\max} + \sigma_{\omega_{\max}} \leq \sigma_0$. (8)

The maximal normal stresses [2, 17] are defined in the forms

- for the I-section beam

$$\sigma_{Xi\max} = \frac{M_{Xi}}{W_{Xi}} \quad (i = 1,2), \quad \sigma_{\omega\max} = \frac{B}{W_\omega},$$ (9)

where W_{Xi} (i = 1,2) are the section moduli for the principal axes for the channel-section, and

- for the Z-section beam

$$\overline{\sigma_x}_{\max} = \frac{\overline{M_x}}{W_x}, \quad \overline{\sigma_y}_{\max} = \frac{\overline{M_y}}{W_y}, \quad \sigma_{\omega\max} = \frac{B}{W_\omega},$$ (10)

where W_x and W_y are the section moduli for the longitidunal axes for the Z-section and W_ω is the sectorial section modulus for the considered cross-sections.

After the introduction of Eq. (9) into Eq. (7), and Eq. (10) into Eq. (8), the constraint function becomes:

- for the I-section beam: $\varphi = \dfrac{M_{X1}}{W_{X1}} + \dfrac{M_{X2}}{W_{X2}} + \dfrac{B}{W_\omega} - \sigma_0 \le 0$, $\qquad$ (11)

and

- for the Z-section beam: $\varphi = \dfrac{\overline{M_x}}{W_x} + \dfrac{\overline{M_y}}{W_y} + \dfrac{B}{W_\omega} \le \sigma_0$. $\qquad$ (12)

The constraint functions (11) and (12) are reduced to:

- for the I-section beam:

$$\varphi = \varphi(b_1, b_2) = 6M_{X1} \frac{1}{t_1 b_1 b_2 \left(6 + \dfrac{t_2}{t_1}\dfrac{b_2}{b_1}\right)} + 3M_{X2}\frac{1}{t_1 b_1^2} + 6B\frac{1}{t_1 b_1^2 b_2} - \sigma_0 \le 0 , \qquad (13)$$

and
- for the Z-section beam:

$$\varphi = \varphi(b_1, b_2) = 30M_x \frac{1}{t_1 b_1 b_2 \left(3 + 2\dfrac{t_2}{t_1}\dfrac{b_2}{b_1}\right)} + $$

$$+ 3M_y \cdot z \cdot \frac{9 + \dfrac{t_2}{t_1}\dfrac{b_2}{b_1}}{t_1 b_1 b_2 \left(3 + 2\dfrac{t_2}{t_1}\dfrac{b_2}{b_1}\right)} + 6B \frac{1 + \dfrac{t_2}{t_1}\dfrac{b_2}{b_1}}{t_1 b_1^2 b_2 \left(1 + 2\dfrac{t_2}{t_1}\dfrac{b_2}{b_1}\right)} - \sigma_0 \le 0 \qquad (14)$$

The expressions (13) and (14) represent the constraint functions corresponding to the given stress constraints.

3. Results and discussion

3.1 Analytic solution

One of the most common problems is that of finding maxima or minima (in general, "extrema") of a function. The Lagrange multiplier method [6, 7, 10, 18, 19] is a powerful tool for solving this class of problems and represents the classical approach to the constraint optimization. It is a method for finding the extremum of the function of several variables when the solution must satisfy a set of constraints, and for the analogous problem in the calculus of variations. Lagrange multiplier, labeled as λ, measures the change of the objective function with respect to the constraint.

Applying this method to the vector depending on two parameters b_i , (i = 1, 2), the system of Equations (13) of the form

$$\frac{\partial}{\partial b_i}\left[A\left(b_1, b_2\right) + \lambda\,\varphi\left(b_1, b_2\right)\right] = 0, \quad (i = 1, 2) \tag{15}$$

will be obtained and after the elimination of the multiplier λ, it will become

$$\frac{\partial A\left(b_1, b_2\right)}{\partial b_1} \cdot \frac{\partial \varphi\left(b_1, b_2\right)}{\partial b_2} = \frac{\partial A\left(b_1, b_2\right)}{\partial b_2} \cdot \frac{\partial \varphi\left(b_1, b_2\right)}{\partial b_1}\ . \tag{16}$$

The beams of the given cross-sections (Fig.1) are the objects of the optimization.

Let the ratio

$$z = b_2 / b_1 \tag{17}$$

be the optimal ratio of the parts of the considered cross-section and let

$$\psi = t_2 / t_1\ , \tag{18}$$

be the ratio of the flange and web thicknesses.

After the introduction of the expression for the bimoment into the Equations (13) and (14), the Equations (16) can be reduced to the equation whose solutions give the optimal values of the ratio (17). The solutions are in the form

- of the fourth order for the considered I-beam

$$\sum_{k=0}^{k=4} c_k z^k = 0\ , \tag{19}$$

where the coefficients c_k in Eq.(19) are defined by Eqs. (20)

$$c_0 = -12\left(1 + 6\xi_1\right),$$
$$c_1 = 2\left[\psi\left(1 + 24\xi_1\right) - 36\xi_2\frac{M_{X2}}{M_{X1}}\right],$$
$$c_2 = 2\psi\left[11\psi\xi_1 + 6\left(3 + 4\xi_2\right)\frac{M_{X2}}{M_{X1}}\right],$$
$$c_3 = 2\psi^2\left[\psi\xi_1 + \left(6 + 11\xi_2\right)\frac{M_{X2}}{M_{X1}}\right],$$
$$c_4 = \psi^3\left(1 + 2\xi_2\right)\frac{M_{X2}}{M_{X1}}\ , \tag{20}$$

and

- of the sixt order for the considered Z-section beam

$$\sum_{k=1}^{6} c_k z^k = 0 , \tag{21}$$

where the coefficients c_k in Eq. (21) are defined by Eqs. (22)

$$c_0 = 60 + 144(\xi_1 + \xi_2) ,$$

$$c_1 = 2\psi(145 + 276\xi_1 + 264\xi_2) + 36(3\xi_1 + 4\xi_2)\frac{M_y}{M_x} ,$$

$$c_2 = 2\psi\left\{ 4\psi(55 + 38\xi_1 + 27\xi_2) - 3[4 - 23(3\xi_1 + 4\xi_2)]\frac{M_y}{M_x} \right\} ,$$

$$c_3 = \psi^2\left\{ 4\psi(50 - 75\xi_1 - 84\xi_2) - [123 - 76(3\xi_1 + 4\xi_2)]\frac{M_y}{M_x} \right\} ,$$

$$c_4 = -\psi^3\left\{ 8\psi(31\xi_1 + 24\xi_2) + [208 + 75(3\xi_1 + 4\xi_2)]\frac{M_y}{M_x} \right\} ,$$

$$c_5 = -2\psi^4\left[16\psi\xi_1 + 31(2 + 3\xi_1 + 4\xi_2)\frac{M_y}{M_x} \right] ,$$

$$c_6 = -8\psi^5(2 + 3\xi_1 + 4\xi_2)\frac{M_y}{M_x} . \tag{22}$$

It is obvious that the coefficients c_k ($k = 1, 2, \ldots, 6$) depend on the ratio of the bending moments and on the eccentrities ξ_1 and ξ_2 of their planes.

The results that follow were obtained by the analytical approach.

3.2   Optimal values $z = b_2 / b_1$

From the general case, when bending moments about both principal axes appear simultaneously with the bimoment, some particular cases can be considered, depending on the ratio M_{X2}/M_{X1} for the I-secton and M_y / M_x for the Z-section beam.

The optimal ratios z (17) obtained from the equations (19) and (21) are calculated for M_{X2}/M_{X1} (M_y / M_x) = 0, 0.1, 0.5, 1; $\psi = 0.5, 0.75, 1$ and $\xi_1, \xi_2 = 0, 0.2, 0.4, 0.6, 0.8, 1.0$, or in other way for $0 \leq \xi_1 \leq 1; 0 \leq \xi_2 \leq 1$.

I-beam

The highest and the lowest optimal values of z for $M_{X2}/M_{X1} = 0, 0.1, 0.5, 1$ and $\psi = 0.5, 0.75$ and 1.0, are shown in a shortened form in Table 1.

Table 1. I-beam: Optimal $z = b_2 /b_1$ for M_{X2}/M_{X1}= 0.1, 0.5, 1 and $\psi = 0.5; 0.75; 1$

M_{X2} /M_{X1}	ψ	z
	0.5	$2.19 \leq z \leq 12$
0	0.75	$1.46 \leq z \leq 8$
	1	$1.09 \leq z \leq 6$
	0.5	$2 \leq z \leq 2.02$
0.1	0.75	$1.37 \leq z \leq 1.58$
	1	$1.04 \leq z \leq 1.32$
	0.5	$1.02 \leq z \leq 1.72$
0.5	0.75	$0.82 \leq z \leq 1.20$
	1	$0.69 \leq z \leq 0.93$
	0.5	$0.75 \leq z \leq 1.59$
1	0.75	$0.59 \leq z \leq 1.11$
	1	$0.51 \leq z \leq 0.86$

From the Table 1 it can be concluded that the values of z are decreasing when the ratio $\psi = t_2 / t_1$ is increasing and that they are decreasing when the load ratio is increasing.

Z-section beam

Like in the case of the channel-section, the optimal values $z = b_2 /b_1$ for the Z-section beam for ratios $M_y /M_x = 0$, 0.1, 0.5, 1 and $\psi =$0.5, 0.75 and 1.0, are given in a shortened form in Table 2.

Table 2: Optimal $z = b_2 /b_1$ for $M_y /M_x = 0$, 0.1, 0.5, 1 and $\psi = 0.5; 0.75; 1$

M_y /M_x	ψ	z
	0.5	$2.57 \leq z \leq 8.99$
0	0.75	$1.67 \leq z \leq 6.04$
	1	$1.25 \leq z \leq 4.53$
	0.5	$2.61 \leq z \leq 5.54$
0.1	0.75	$1.75 \leq z \leq 4.38$
	1	$1.31 \leq z \leq 3.70$
	0.5	$2.53 \leq z \leq 2.74$
0.5	0.75	$1.70 \leq z \leq 2.19$
	1	$1.28 \leq z \leq 1.86$
	0.5	$2 \leq z \leq 2.49$
1	0.75	$1.60 \leq z \leq 1.67$
	1	$1.26 \leq z \leq 1.37$

From the Table 2, also, it can be concluded that the values of z are decreasing when the ratio $\psi = t_2 / t_1$ is increasing and that they are decreasing when the load ratio is increasing.

3.3   The loading cases

From the general case, when bending moments about both principal axes appear simultaneously with the bimoment, some particular cases can be considered depending on the loading case.

In this section an I-beam and Z-section beam are fixed at one end and subjected to the concentrated bending moment M_{X1} (M_x)= 10 kNcm; M_{X2} (M_y) = 0 at the free end of the beam in two ways (Figs. 2 and 3) as: a) Loading case 1: $\xi_1 = \xi_2 = 0$ and b) Loading case 2: $\xi_1 = 0.5$, $\xi_2 = 0$.
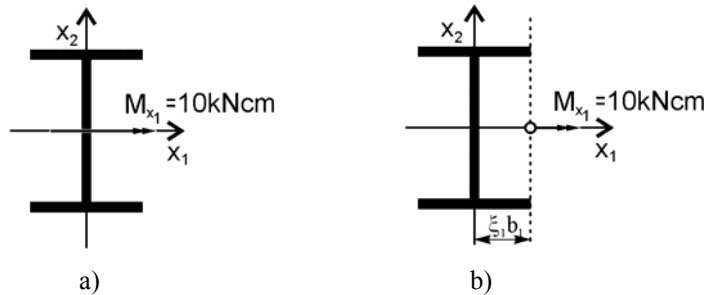
Figure 2. I-section: a) Loading case 1, b) Loading case 2
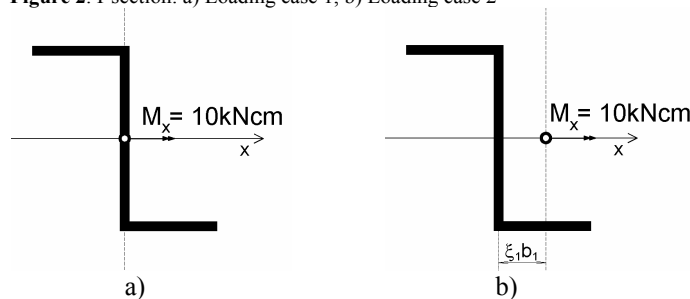
Figure 3. Z-section: a) Loading case 1, b) Loading case 2

4.   Numerical example

As the numerical example, considered cantilever beams with the lengths l=150 cm, fixed at one end are subjected to the bending moments M_{X1} (M_x) = 10 kNcm; M_{X2} (M_y) = 0.

The initial cross-sectional geometrical characteristics are calculated taking into account the initial dimensions of the I and the Z-sections. It is assumed that considered sections have the same initial cross-sectional geometrical characteristics: $b_1 = 5.175$ cm, $b_2 = 9.2$ cm, $t_1 = 0.8$ cm, $t_2 = 0.65$ cm. For the given loads (Figs. 2 and 3) and the defined geometry of the profile, the initial stresses are calculated.

4.1   Determination of the minimum cross-sectional area

The problem is considered in two ways:

1) The optimal dimensions of the cross-section $b_{1optimal}$ and $b_{2optimal}$ are obtained by equalizing the "Initial" and the "Optimal area" ($A_{initial}=A_{optimal}$) and by using the calculated optimal relation z. In that case the normal stress lower than the initial one is obtained ($\sigma_{optimal}<\sigma_{initial}$). It represents the model used for the control or **Optimal model no. 1**.

2) From the condition prescribing that the stresses must be lower than the allowable one, i.e. the "Initial stress", the optimal values $b_{1optimal}$ and $b_{2optimal}$ are obtained by using the calculated optimal relation z and by comparing the stress defined by the optimal geometrical characteristics to the "Initial stress". It represents the **Optimal model no. 2**. Starting from the optimal cross-sectional dimensions ($b_{1optimal}$ and $b_{2optimal}$), the optimal-minimum cross-sectional area A_{min} is calculated for each loading case and the results including the saved mass of the material are given in Tables 3 and 4.

Table 3. I-beam: Normal stresses and saved mass: $z_{initial} = 1.78$

Loading case	$z_{optimal}$	$\sigma_{initial}$ [kN/cm²]	$\sigma_{optimal\ no.1}$ [kN/cm²]	$\sigma_{optimal\ no.2}$ [kN/cm²]	$A_{initial}=A_{optimal\ no.1}$ [cm²]	$A_{min}=A_{optimal\ no.2}$ [cm²]	Saved mass [%]
1	7.38	0.20	0.19	0.20	14.26	12.60	11.64
2	1.46	0.94	0.94	0.94		14.23	0.22

Table 4. Z-beam: Normal stresses and saved mass: $z_{initial} = 1.78$

Loading case	$z_{optimal}$	$\sigma_{initial}$ [kN/cm²]	$\sigma_{optimal\ no.1}$ [kN/cm²]	$\sigma_{optimal\ no.2}$ [kN/cm²]	$A_{initial}=A_{optimal\ no.1}$ [cm²]	$A_{min}=A_{optimal\ no.2}$ [cm²]	Saved mass [%]
1	5.58	1.34	0.75	1.34	14.26	10.33	27.56
2	2.99	2.59	2.46	2.59		13.98	1.96

From the Tables 3 and 4 it can be seen that greater saved mass of the material was obtained for Z-section than for I-section. Also, for all loading cases the level of stresses is decreased in the Optimal model no.1 with the area of the cross-section having the same value as in the "Initial model" and the saved mass of material is increased with respect to the initial stress limits in the Optimal model no.2 where the area is smaller than the initial one. The calculation showed that the maximum saved material is obtained in the Loading case 1 and the minimum in the Loading case 2 for both shapes of cross-sections. This allows to conclude that if the distance of the loading plane from the shearing plane is increased the optimization of the cross-section is less necessary to be done.

5.   Conclusions

The paper presents one approach to the optimization of the thin-walled open section beams, loaded in a complex way, using the Lagrange multiplier method.

Accepting the cross-sectional area as the objective function and the stress constraints as the constrained function, it is possible to find the optimal relation between the dimensions of the web and the flanges of the considered thin-walled profiles in a very simple way.

In addition to the general case, some particular loading cases are considered. As the result of the calculation the modified constrained functions are derived as the polynomials of the fourth and eight order.

Particular attention is directed to the calculation of the saved mass using the proposed analytical approach. It is also possible to calculate the saved mass of the used material for different loading cases.

The aim of the paper is the optimization of thin-walled elements subjected to the complex loads, and it may be concluded that the paper gives the general results permitting the derivation of the expressions that can be recommended for technical applications.

References

[1]   Timoshenko S P and Goodier J N (1951) *Theory of elasticity*, McGraw-Hill Book Comp Inc., New York.
[2]   Kollbruner C F and Hajdin N (1972) *Dunnwandige Stabe*, Band 1, Springer Verlag.
[3]   Kollbruner C F and Hajdin N (1975) *Dunnwandige Stabe*, Band 1, Springer Verlag.
[4]   Vlasov V Z (1961) *Thin walled elastic beams* (2nd ed.), National Science Foundation, Washington DC.
[5]   Vlasov V Z (1959) *Thin-Walled Elastic Beams*, second ed., Moscow (English translation, Israel Program for Scientific Translation, Jerusalem, 1961).
[6]   Fox R L (1971) *Optimization Methods for Engineering Design*, Addison-Wesley Publishing Company Inc.
[7]   Brousse P (1975) *Structural Optimization*, CISM, No.237, Springer-Verlag, Wien.
[8]   Prager W (1974) *Introduction to Structural Optimization*, CISM, No.212, Springer-Verlag, Wien.
[9]   Fletcher R (1996) *Practical Methods of Optimization (second edition)*, John Wiley & Sons, New York.
[10]   Bertsekas D P (1996) *Constrained Optimization and Lagrange Multiplier Methods*, Athena Scientific, Belmont.
[11]   Farkas J (1984) *Optimum Design of Metal Structures*, Akademiai KIADO, Budapest.
[12]   Selmic R, Cvetkovic P, Mijailovic R and KastratovicG (2006) Optimum Dimenzions of Triangular Cross-Section in Lattice Structures, *Meccanica*, **41**(4) pp. 391-406.
[13]   Ružić D, Anđelić N and Milošević V (1996) One More View on The Problem of Optimization of an I-Beam, *Bulletins for Applied Mathematics*, LXXIX, PC-116, God, TU Budapest, Hungary, pp. 367-372.
[14]   Andjelić N (2003) Thin walled I-beam under complex loads - Optimization according to stress constraint, *FME Transactions*, **31**(2), pp. 55 – 60.
[15]   Andjelić N and Milosevic-Mitic V (2006) Optimization of a thin-walled cantilever beam at constrained torsion, *Structural integrity and life*, **6**(3), pp. 121-128.

[16]   Andjelić N, Milosevic-Mitic V and Maneski T (2009) An approach to the optimization of Thin-walled Z-beam, *Strojniški vestnik - Journal of Mechanical Engineering*, 55(12), pp. 742-748.

[17]   Ružić D (1995) *Strength of Structures* (in Serbian), University of Belgrade, Faculty of Mechanical Engineering.

[18]   Onwubiko C (2000) *Introduction to Engineering Design Optimization*, Prentice Hall, New Jersey Inc.

[19]   Zoller K (1972) Zur anschaulichen Deutung der Lagrangeschen Gleichungen zweiter Art, *Ingenieur-Archiv*, **41**(4), Springer-Verlag, pp. 270-277.

THE INFLUENCE OF LOAD AND BOUNDARY CONDITION SIMULATION ON THE STRUCTURAL EVALUATION OF RAILWAY WAGONS WITH FINITE ELEMENT TOOLS

I. Atanasovska

Institute Kirilo Savic, Belgrade
Vojvode Stepe 51, 11010 Belgrade, Serbia
e-mail: iviatanasov@yahoo.com

Abstract. This paper investigates the influence of the load and boundary condition simulation during calculation of mechanical structures. The investigations are performed on the real freight wagon structure, as a case of very complex mechanical structure that can be analytically calculated approximately. The consequences of errors in research practice through the load and boundary condition simulation and their influence on the positions and values of the maximum stresses are shown and discussed. In the years of the rapid developing of methods for mechanical components and structures calculations, one of the essentials problems was definition of mathematical models of complex mechanical structures that can't be analytical calculated.

1. Introduction

Finite element procedures are at present very widely used in engineering analysis. For any Finite element analysis (FEA), a mathematical model must be selected and then solved. The Finite element method is employed to solve very complex mathematical models, but it is important to know that the finite element solution can never give more information than that contained in the mathematical model.
Finite element analysis bases on the physical discretization of treated continuum with parts of finite dimension and simple shape named finite elements. Thus, treated deformable body, i.e. continuum with infinite degrees of freedom becomes replaced by discrete model with joined finite elements with finite numbers of freedom. From mathematical standpoint, instead of system of differential equations which defines equilibrium of the whole model, by Finite element method we obtain system of plain algebraic equations.
In investigation of behavior of deformable body by finite elements, first step is choice of discrete model which should be best approximation of stress and strain state and boundary conditions. The choice of discrete model is the choice of finite element type that will be used (one or more different types); the choice of their particular properties (if there is some) and the choice of mesh density. There are no exact criteria for the best discrete model with the highest accuracy for the particular case. Therefore, besides understanding theory of finite element, the experience and qualitative knowledge of stress and strain state from case to case is necessary requirement. Above mentioned is the key thesis of the paper and will be demonstrated for one real case study.

2. The basic equations of Finite Element Method

During Finite element method (FEM) using, on the basis of the chosen finite element type, material properties and other values significant for problem solving, the relationships between basic values are defined with prime finite element equation. Arrangement of prime equations for all finite elements gives equation of construction – system of linear equations.
The Finite element method is based on the mechanics of continuum, [1]. The basic task is determination of the displacement functions, i.e. determination of displacement values for nodes of finite element mesh. For any construction divided on finite elements, displacement of any point of a finite element can be determinate as function of element's nodes displacements. It is accepted that displacements, deformations and stresses are continual functions of nodes coordinates.
Very often, equivalent values of deformations and stresses are used for efficient results tracking. First, main deformations (ε_1, ε_2 and ε_3) and main stresses (σ_1, σ_2 and σ_3) must be calculated. These values correspond to the solutions for ε_0 (three values) and σ_0 (three values) from cubic equations with following matrix form:

$$
\begin{vmatrix}
\varepsilon_x - \varepsilon_0 & \dfrac{1}{2}\varepsilon_{xy} & \dfrac{1}{2}\varepsilon_{xz} \\[2mm]
\dfrac{1}{2}\varepsilon_{xy} & \varepsilon_y - \varepsilon_0 & \dfrac{1}{2}\varepsilon_{yz} \\[2mm]
\dfrac{1}{2}\varepsilon_{xz} & \dfrac{1}{2}\varepsilon_{yz} & \varepsilon_z - \varepsilon_0
\end{vmatrix} = 0 \; ;
\begin{vmatrix}
\sigma_x - \sigma_0 & \sigma_{xy} & \sigma_{xz} \\[2mm]
\sigma_{xy} & \sigma_y - \sigma_0 & \sigma_{yz} \\[2mm]
\sigma_{xz} & \sigma_{yz} & \sigma_z - \sigma_0
\end{vmatrix} = 0 \tag{1}
$$

More often, for results tracking FEA used VonMises equivalent deformations $\varepsilon_{VonMises}$ and VonMises equivalent stresses $\sigma_{VonMises}$:

$$
\varepsilon_{VonMises} = \frac{1}{1+\nu}\left(\frac{1}{2}\left[\left(\varepsilon_1 - \varepsilon_2\right)^2 + \left(\varepsilon_2 - \varepsilon_3\right)^2 + \left(\varepsilon_3 - \varepsilon_1\right)^2\right]\right)^{\frac{1}{2}} \tag{2}
$$

$$
\sigma_{VonMises} = \left(\frac{1}{2}\left[\left(\sigma_1 - \sigma_2\right)^2 + \left(\sigma_2 - \sigma_3\right)^2 + \left(\sigma_3 - \sigma_1\right)^2\right]\right)^{\frac{1}{2}} \tag{3}
$$

2.1. Finite element equation

By neglecting temperature induced stress, obtained link between node translations and forces on nodes, known as equation of finite element, [1], has following form:

$$
\{F\} = \left[K^e\right]\{S\} \tag{4}
$$

In this expression, matrix $[K^e]$ is stiffness matrix of finite element, which elements are influenced by physical properties of material, characteristic of finite element type and by chosen interpolation functions.

2.2. Equation of construction

With combining of basic equations based on (4) of all finite elements included in mesh of a construction or a body, equation of construction is obtained in following form:

$$\{F\} = [K]\{S\} \tag{5}$$

where is :

$$\{F\} = \begin{Bmatrix} \{\overline{F}^{(1)}\} \\ \{\overline{F}^{(2)}\} \\ \vdots \\ \{\overline{F}^{(n)}\} \end{Bmatrix} \; ; \; \{S\} = \begin{Bmatrix} \{\overline{S}^{(1)}\} \\ \{\overline{S}^{(2)}\} \\ \vdots \\ \{\overline{S}^{(n)}\} \end{Bmatrix} \tag{6}$$

In these vectors n represents total number of nodes of constructions, which is equal to the sum of total number of nodes in mesh and the number defined by boundary conditions (supports). The number of elements of each sub-matrix in vectors (6) is equal to the number of degree of freedom of the finite element p, so the vectors $\{F\}$ and $\{S\}$ have pxn elements. Certain node translations are known and determined by support of the construction. Known node translations represent the boundary conditions. When those boundary conditions are inserted in construction equation (5) certain number of equations can be eliminated, having as a result reduced number of degrees of freedom.

External forces that act on the constructions are involved in equations as force components in directions of a coordinate system axis at the nodes. If construction has concentrated loadings, mesh nodes are set up in manner that in the each point of acting concentrated loads there is only one mesh node of finite element. For the case of continuous loading the nodes are loaded by equivalent node loading, where is necessary to known the function of loading over the line or the surface.

3. Finite element analysis of a wagon

The Finite element method is often used for the calculations of wagon parts or whole wagons, [2], [3]. This paper analyzed the structural analysis for the wagon of the Falns type.

3.1. Used finite element types

For model discredization one or few finite element types can be used. When few different finite element types are used in the model discredization (that is case of the analyzed problem) used element types must be join each other. The elements selected for modeling the wagon are 4 node shell elements and 2 node beam elements with elastic behavior. These element types simulate the behavior of wagon construction parts better of solid elements.

Shell elements are a special class of elements that are designed to efficiently model thin structures. They take advantage of the fact that the only shear on the free surfaces is in-plane. Normals to the shell middle surface stay straight, but not necessarily normal. As a

result, the in-plane strain variation through the thickness cannot be more complex than linear. The chosen 4-Node Finite Strain Shell is suitable for analyzing thin to moderately-thick shell structures. It is a 4-node element with six degrees of freedom at each node: translations in the x, y, and z directions, and rotations about the x, y, and z-axes. The degenerate triangular option should only be used as filler elements in mesh generation. The geometry, node locations, and the element coordinate system for this element are shown in Figure 1. The element is defined by four nodes: I, J, K, and L. The element formulation is based on logarithmic strain and true stress measures. To define the thickness and other information, either real constants or section definition can be used.
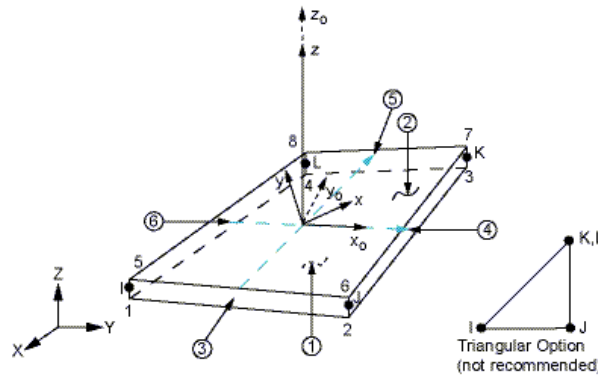
Figure 1. 4-Node Finite Strain Shell geometry.

Beam elements are used to create a mathematical one-dimensional idealization of a 3-D structure. They offer computationally efficient solutions when compared to solid and shell elements. Cross section defines the geometry of the beam in a plane perpendicular to the beam axial direction. 3-D Linear Finite Strain Beam is suitable for analyzing slender to moderately stubby/thick beam structures. This element is based on Timoshenko beam theory which is a first order shear deformation theory: transverse shear strain is constant through the cross-section; that is, cross-sections remain plane and undistorted after deformation. Shear deformation effects are included and in 3-D has six degrees of freedom at each node. These include translations in the x, y, and z directions and rotations about the x, y, and z directions. This element is well-suited for linear, large rotation, and/or large strain nonlinear applications. 3-D Linear Finite Strain Beam can be used with any beam cross-section. The cross-section associated with the beam may be linearly tapered.
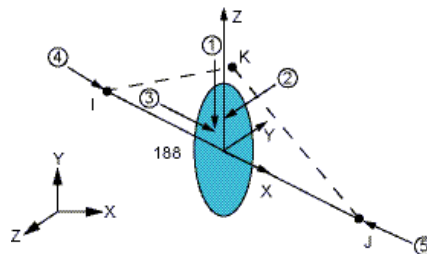
Figure 2. 3-D Linear Finite Strain Beam geometry.

The geometry, node locations, and coordinate system for this element are shown in Figure 2. 3-D Linear Finite Strain Beam is defined by nodes I and J in the global coordinate system. Node K is a preferred way to define the orientation of the element.

3.2. FEM model of wagon

The used model takes advantage of the longitudinal and transversal symmetry of the wagon. A quarter of wagon was used taking in consideration the correspondent symmetry of the load cases. For the unsymmetrical load cases, a half wagon model and a full model were used. The model general characteristics are summarized in table 1. The used material properties are in accordance with EN 10025-2, [4] and are presented in table 2. Table 3 shows allowable stresses for static loads.

Table 1 – Model characteristics

Characteristic	Value
General element dimension (side length)	40 mm
Number of shell elements (quarter wagon)	41456
Number of beam elements quarter wagon)	614
Total number elements (quarter wagon)	42070
Model Mass (full structure)	10 887,2 kg

Table 2 – material characteristics

Properties	Value
Young modulus	201 GPa
Poisson ratio	0.3
Density	7 850 kg/m^3

Table 3– Allowable stresses for static loads

Material	Tensile Strength Rm [MPa]	Yield Point Rp e<16 [MPa]	Yield Point Rp e<40 [MPa]	Condition	Allowable Stress e<16 [MPa]	Allowable Stress e<40 [MPa]
				Welds	323	314
S355	490	355	345	Plain Material	355	345

The 3D model developed for research of freight wagon of Falns type is shown at fig.3. Figure 4 shows the finite element discretization of ¼ of wagon with chosen and described finite element types and figure 5 shows finite element model of whole wagon.
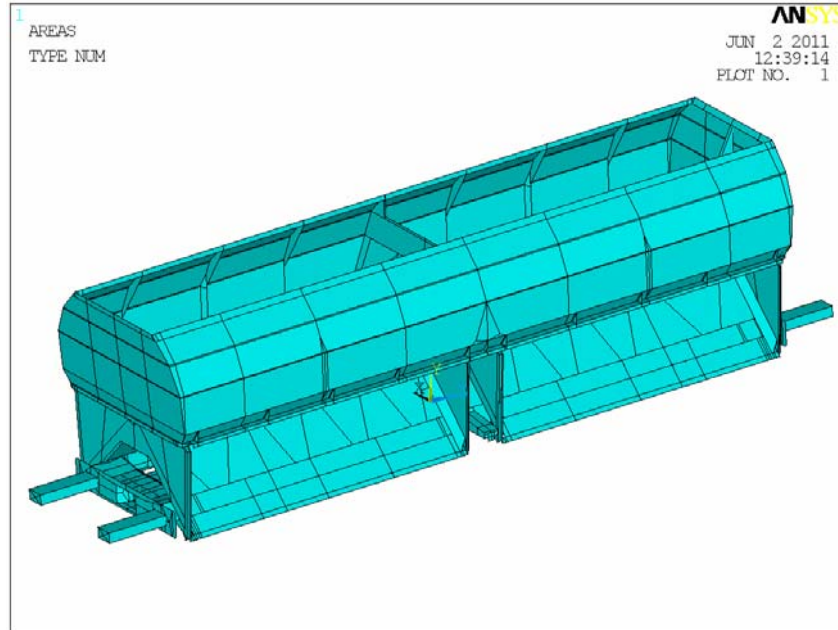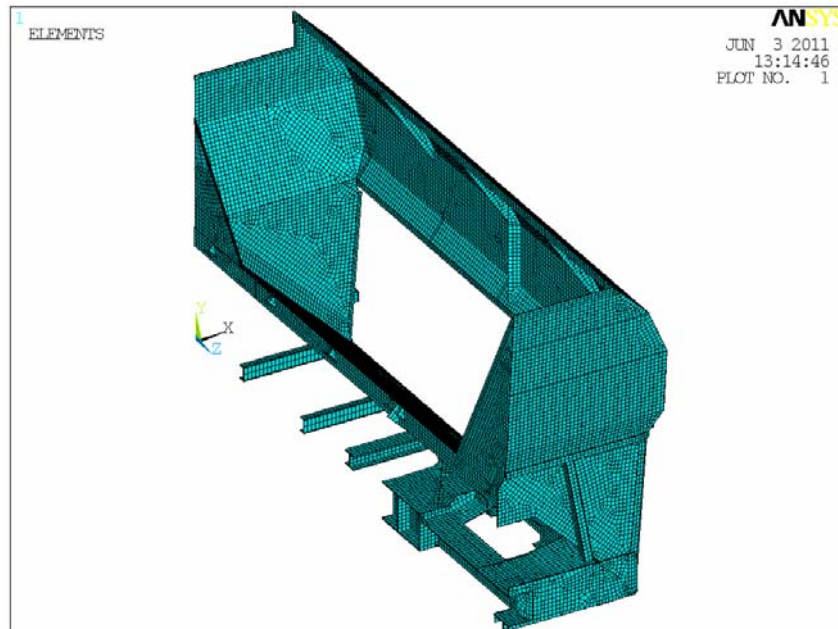
Figure 3. Falns wagon 3D model.

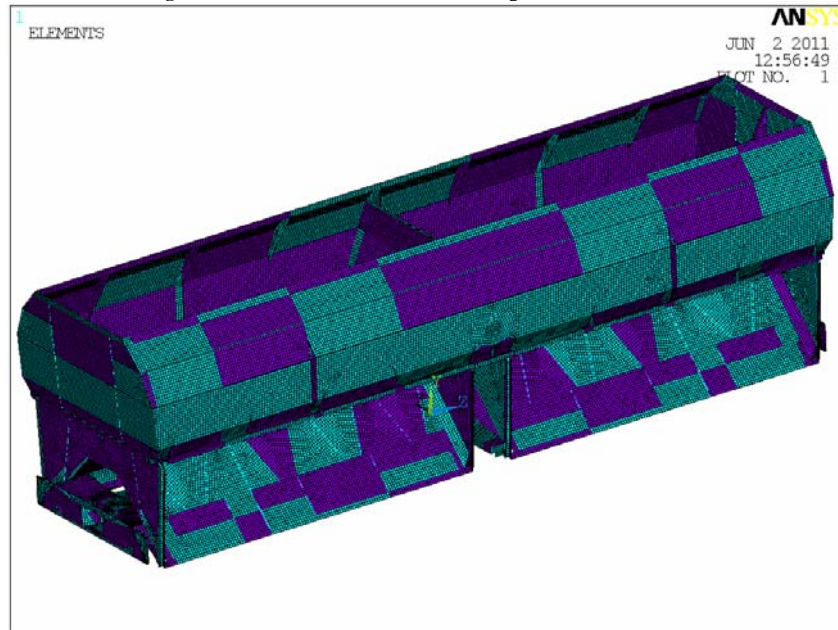**Figure 4.** Finite element model for 1/4 of wagon.

Figure 5. Finite element model of whole wagon.

4. Influence of boundary condition simulation on FEA results

In accordance with international standards for freight wagon verifying, [5], [6], the characteristics for testing load cases are defined. In this paper, two of these load cases are chosen for the research of boundary conditions simulation:

First researched load case: Compression force of 1000 KN applied in the two buffers in buffers centerline. For FEA a quarter of wagon model has been used.

Second researched load case: Diagonally compression forces of 400 KN applied in buffers. For FEA a whole wagon model has been used.

4.1. First load case

Figure 6 shows two simulations of external load for first load case: external load applied as concentrated force in one node of finite element mesh (*a*) and external load applied through contact with bar loaded with same concentrated force (*b*).

VonMises equivalent stresses of wagon body obtained with finite element analysis of *a* simulation and *b* simulation of external force are show on figure 7 and figure 8, respectively. Both of figures show stress contours states of whole wagon body (a) and wagon body with deselected areas on force applied region (b). It is very obviously how concentrated force application can influence on increasing of calculated maximum stresses

358

(in the analyzed case it obtained value of 760MPa instead 269 MPa in the case without direct applying of concentrated force).
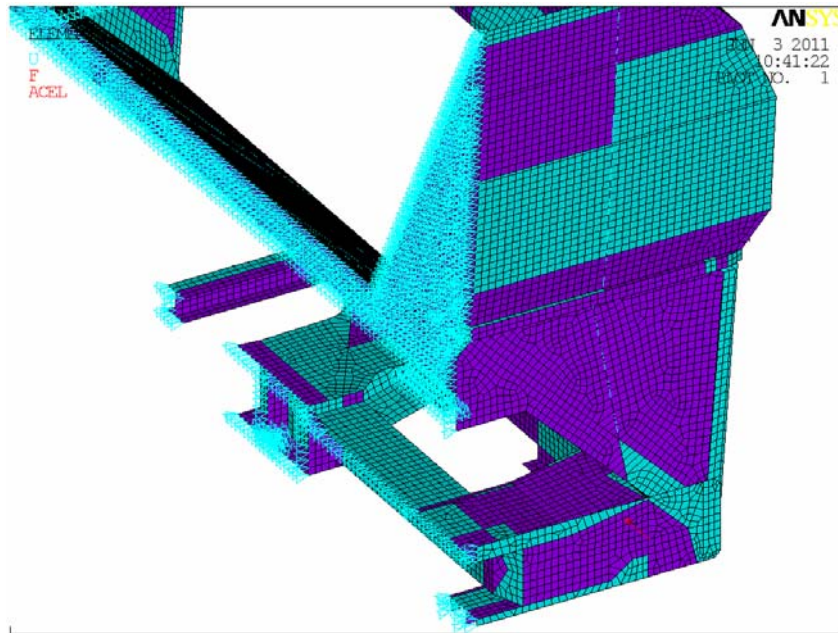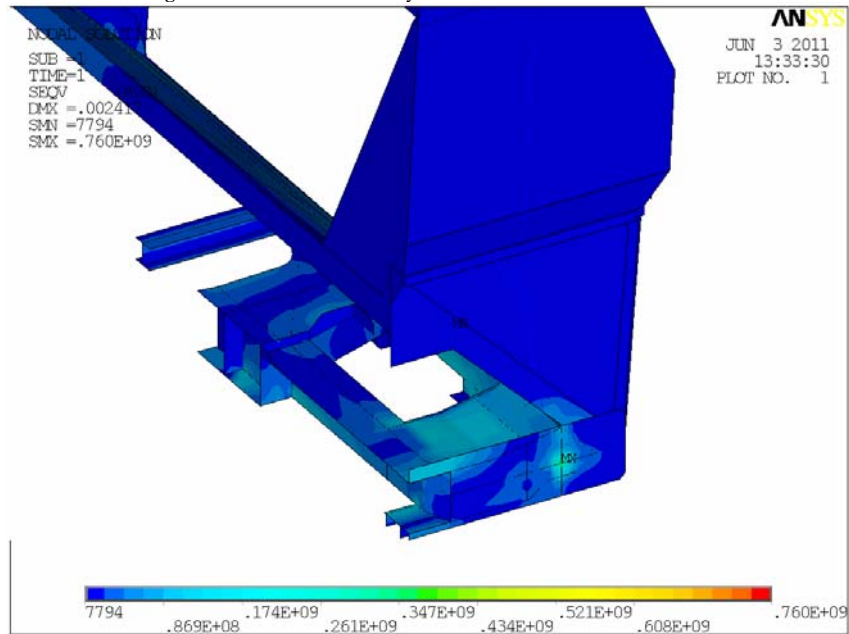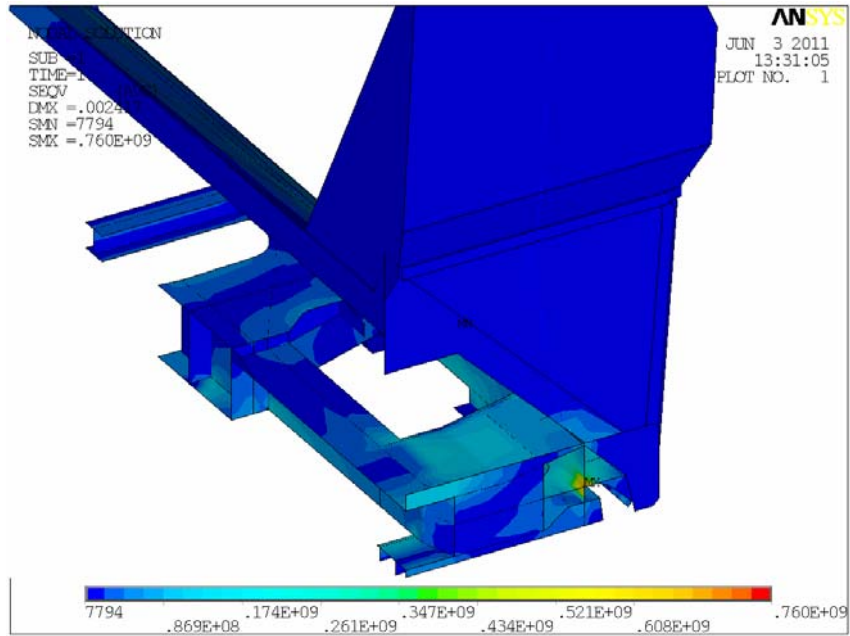

a)
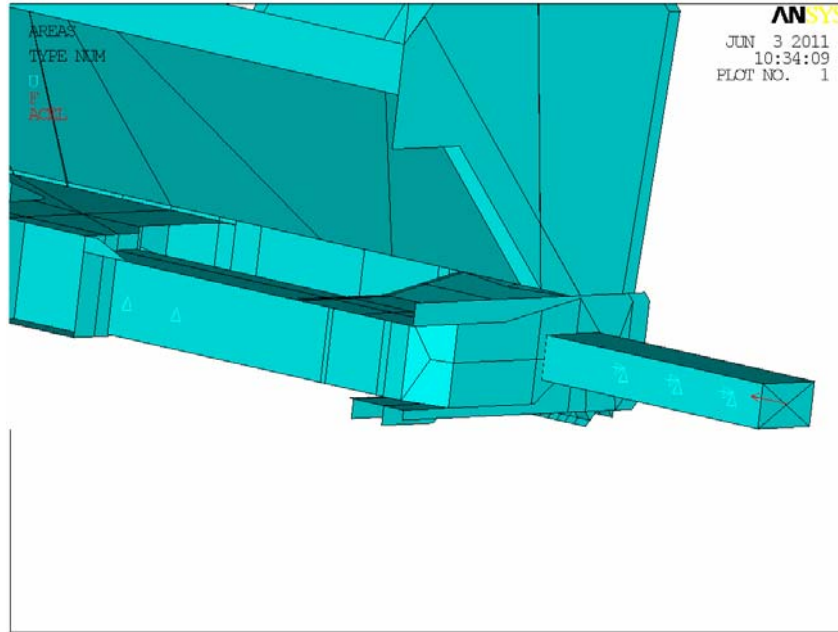
b)

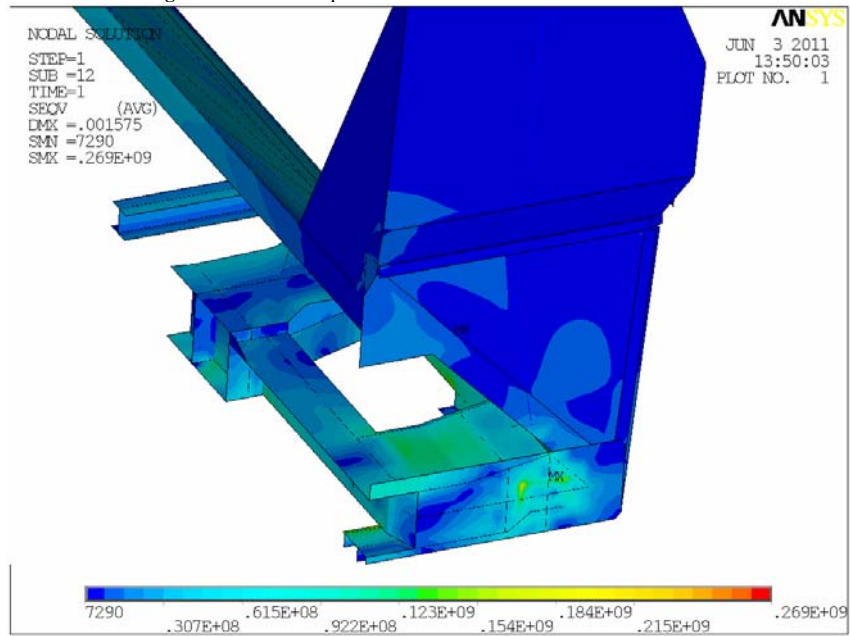**Figure 6.** Two cases of boundary conditions simulations for first load case.
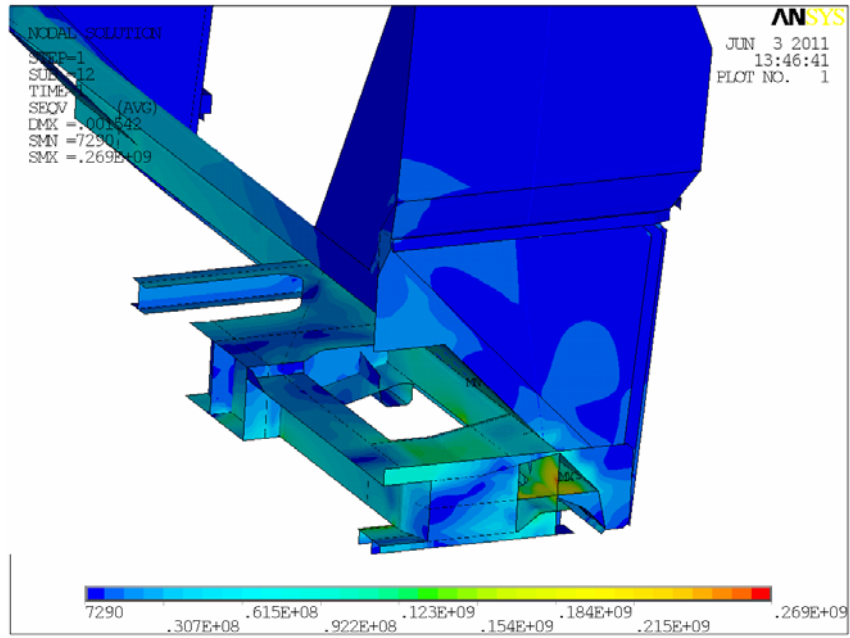

a)

b)

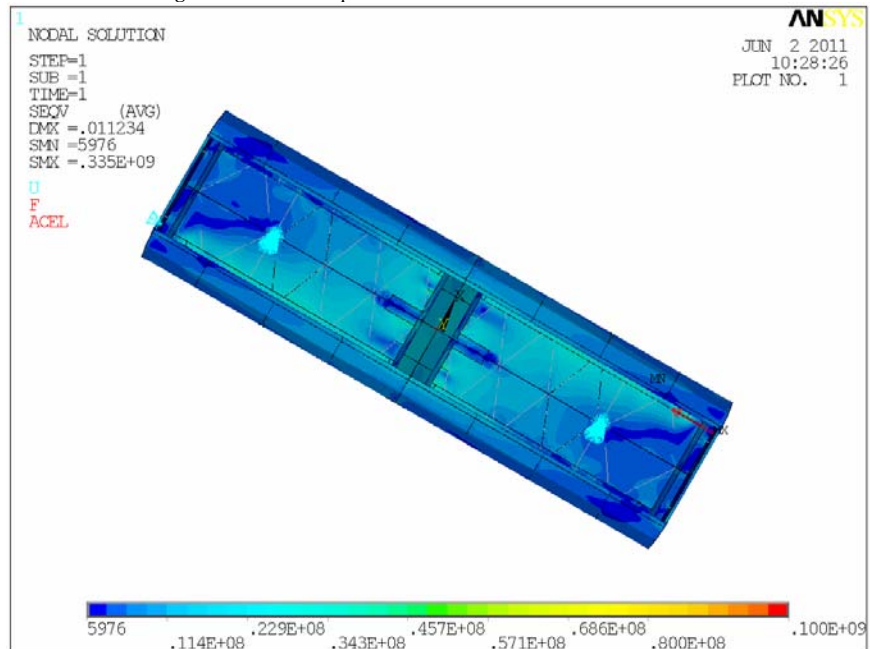**Figure 7.** VonMises equivalent stresses for *a* simulation of first load case.

a)

361

b)

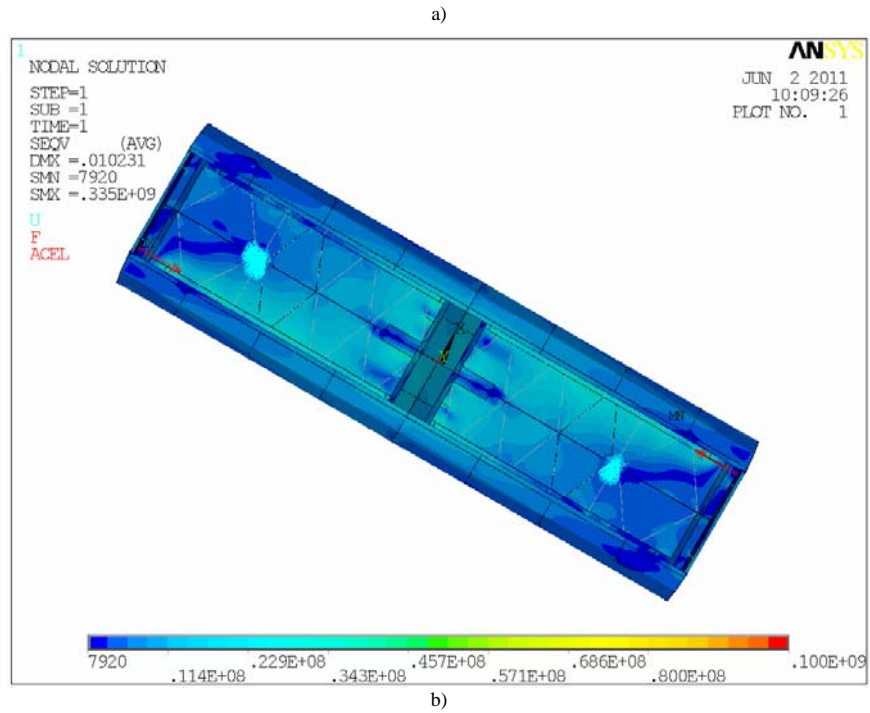**Figure 8.** VonMises equivalent stresses for *b* simulation of first load case.
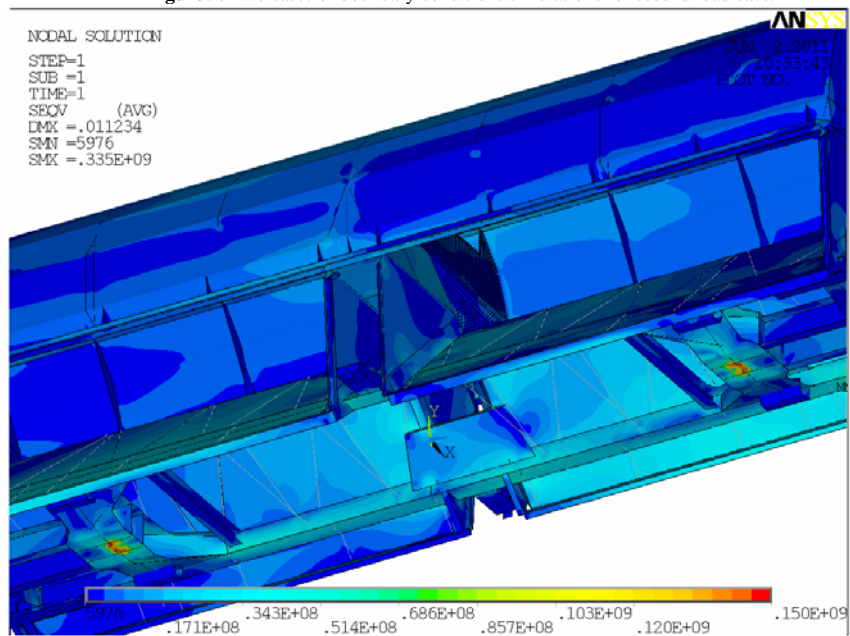
a)

b)

Figure 9. Two cases of boundary conditions simulations for second load case.
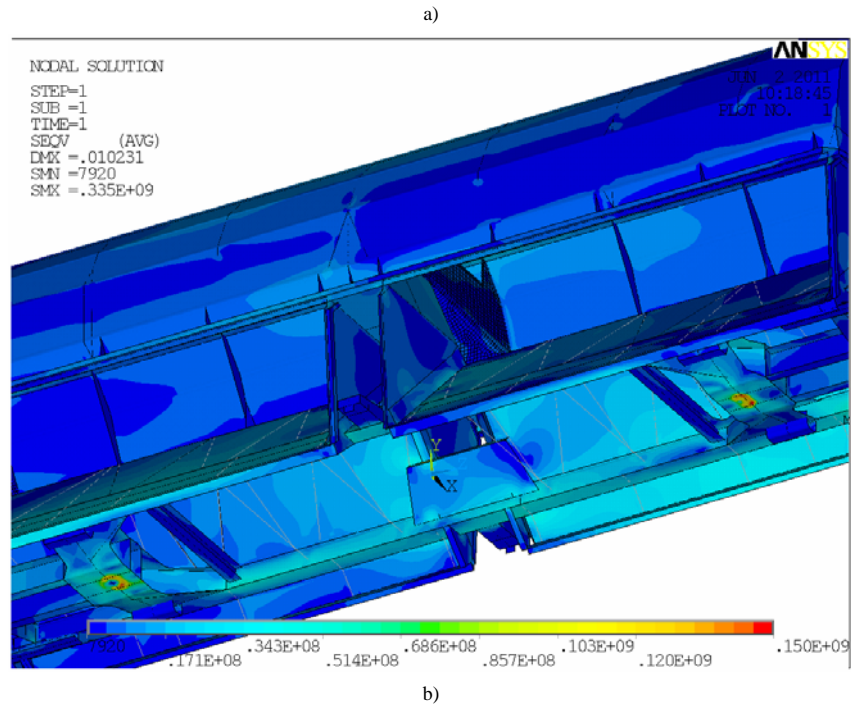
a)

b)

Figure 10. VonMises equivalent stresses for two simulations of second load case.

4.2. Second load case

Figure 9 shows two simulations of external load and displacement constraints for second load case:

- (*a*) diagonally compression forces of 400 KN in buffers are simulated with a compression force applied in one buffer at centerline and reacted at the same vertical level by the diagonally opposed buffer; displacement constraint in direction of applied force are defined only in the reaction node, the displacement constraints in the direction of other two axes of global coordinate system are defined in the place of both of bogie supports
- (*b*) diagonally compression forces of 400 KN in buffers are simulated with two compression forces applied in two diagonal buffers; displacement constraint in direction of applied force are defined in the place of one of bogie supports and the displacement constraints in the direction of other two axes of coordinate system are defined in the place of both of bogie supports

VonMises equivalent stresses of wagon body obtained with Finite element analysis of *a* simulation and *b* simulation of boundary conditions are show on figure 10. Both of figures show stress contours states of whole wagon body for (*a*) simulation case and (*b*) simulation case. The results show the significant influence of boundary condition simulation on stress distribution, i.e. on the nodes with maximum stresses.

5. Conclusion

In the era of increased use of computers, very often researches forgot that definition of the mathematical model that simulate real load conditions is the most important thing during mechanical parts and structures calculations. For young researches it is vary easy to train for one of many commercial applicable finite element tools, since the commercial finite element software is evermore adjusted for users with medium or low level of knowledge about the finite element method theory. These facts lead to problems of wrong load definitions in finite element analysis of real mechanical structures, which further lead to wrong calculation results and cancel all researcher time and effort. This paper shows that chosen mathematical model of real construction and boundary condition simulations are very important step in calculation process for all mechanical constructions and structures.

References

[1] Bathe K. J.: (1982) Finite element procedures in engineering analysis, *Prentice-Hall, Englewood Cliffs*, New Jersey
[2] San Roman J L, Alvarez-Caldas C., Quesada A. (2005) Structural Validation of Railway Bogies and Wagons using Finite Element Tools, *Proc. ImechE, Part F: Rail and Rapid Transit*, Vol.219, pp. 139-150.
[3] Park B. H., Lee K. Y.(2006) Bogie Frame Design in Consideration of Fatigue Strength and Weight Reduction, *Proc. ImechE Part F: Rail and Rapid Transit*, Vol.220, pp. 201-206.
[4] DIN 17100 / EN 10025 Hot Rolled products of non-alloy structural steels. 1994
[5] TSI 2006/861/EC (2006)- technical specification of interoperability relating to the subsystem 'rolling stock — freight wagons' of the trans-European conventional rail system.
[6] EUROPEAN STANDARD EN 12663-2 (2010) Railway applications - Structural requirements of railway vehicle bodies - Part 2: Freight wagons

Trapped waves and end effects in elastic waveguides

Atul Bhaskar
Faculty of Engineering and the Environment
University of Southampton, Southampton, SO17 1BJ, UK
e.mail: A.Bhaskar@soton.ac.uk

Abstract. Traveling acoustic waves conf ned to the straight edge of a semi-inf nite membrane are reported here–they provide an elastic analogue of the skin. The possibility of trapped waves for the transverse motion of membranes is explored for two support conditions. It is shown that waves localize near the edge but propagate along it, when the edge is laden with distributed line mass. Such membranes exhibit edge-guided trapped acoustic waves with or without elastic foundation in the interior. The decay behavior of such localized waves away from the edge depends on the wavenumber–shorter waves decay faster.

1. Introduction

The physics of membranes is of great current interest because of its signif cance to a range of biologically and technologically relevant matter. Stretched f lms frequently surround biological tissues and f uid-f lled anatomical 'structures' such as the eardrum (tympanic membrane) or the cochlea. A good understanding of the dynamic behavior of such elastic media is of interest to a range of potential biomedical applications involving wound care and acoustic/ultrasonic manipulation of tissues and bio-membranes. Membranes are also technologically important (e.g., in the form of thin wafers in electronics) and they are frequently studied in musical acoustics due to their presence in a variety of percussion instruments. Perhaps the simplest geometry that enables the study of dynamic effects at the boundaries is one of semi-inf nite extent with a straight edge. With this motivation, here we consider a generic abstraction of the geometry and explore the possibility of observing conf ned acoustic waves in semi-inf nite membranes. Finite geometries, although more realistic, may sometimes obscure the physics because of the overly complex details of the ref ections contributing to the overall dynamic response.

It is well known that strings, beams and membranes on elastic foundation possess a critical frequency known as the cut-on (or the cut-off) frequency below which traveling waves do not exist and the motion is spatially localized in all directions. As opposed to this behavior, here we explore the possibility of traveling waves that are localized in one direction but propagate in another and are associated with localized motion *above* the cut-on frequency. This distinguishes the present study from well known cases of evanescent motion [1] in that here we explore genuinely trapped waves characterized by a skin-depth which is reminiscent of the edge-bound localized motion. The acoustic skin-effect does not appear to have been previously reported for membranes. Although the results obtained here are not directly applicable to membranes of f nite extent, the present study affords a useful length
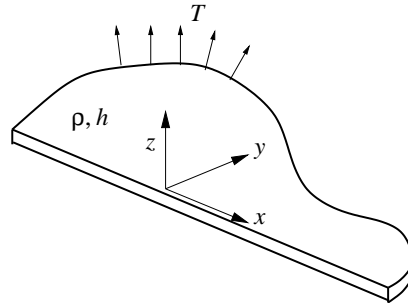
Figure 1. Schematic diagram of a semi-inf nite stretched membrane in transverse motion. The remote tension T is isotropic.

scale in terms of an acoustic skin-depth. When the length scale of a f nite-sized domain is much greater than the skin-depth, approximate conclusions can be drawn on the basis of the physics of the unbounded problem–a generic usefulness of studies involving inf nite geometries.

In unbounded elastic continua, two types of waves freely propagate: they are associated with compression (or pressure) and shear, respectively [2]. Waves in unsupported inf nite plates and those resting on distributed foundation have been studied extensively in the past mainly motivated by a range of applications in engineering and those in geophysics [3]. In comparison, membranes have received relatively little attention. Freely propagating waves in plates are dispersive (shorter waves travel faster) whereas those in membranes are non-dispersive [1]. In all these cases the spatio-temporal variation of the f eld variables (usually displacement) during wave motion is harmonic. As opposed to these, trapped modes are spatially conf ned in at least one direction that extends to inf nity. These waves are also known as the 'bound states'.

Trapped modes have been reported in a host of wave phenomena such as water waves [4, 5, 6, 7, 8], electromagnetism & optics, elastodynamics [9] and acoustics. They are generally associated with spatial localization of the wave motion. Whispering gallery modes in acoustics and water waves guided by the shore-line are waves that decay away from the boundaries and are guided by them: they can also be considered to be trapped waves. The well-known Anderson localization is a phenomenon that is due to scattering induced by disorder in a periodic lattice–we are not concerned with localized motions of this type here. In this paper, we study spatially conf ned wave motion that is due to a boundary surface (or an edge). Perhaps the oldest known example of this type of motion is that of Rayleigh waves. They propagate at the surface of an elastic half-space but are localized depth-wise.

Localized waves at the boundary of an elastic continuum possess interesting propagation behavior [2]. Rayleigh waves [10], Love waves [11] and Stoneley waves [12] possess this character and are very important in geophysics and seismology. At the free surface of a half space, these waves are localized depth-wise, but they propagate on the surface. Such localized propagation behavior in the vicinity of a free surface (characterized by exponential decay in the depth direction [13]) is often known as the 'skin effect' (as in the propagation of electromagnetic waves at the surface of a conductor). For two-dimensional elastic continua, the existence of such waves was perhaps f rst discovered by Konenkov [14]. These waves were later re-discovered several times [15, 16, 17, 18] as Konenkov's work remained

unknown in the West [19]. There has been recent interest in this area and such localized elastic waves at the edge of plates and shells have been reported [20, 21, 22]. Perhaps the simplest 'toy problem' that illustrates the trapped elastic waves is provided by Kaplunov [23]. Trapped modes in curved and slowly varying waveguides have also been reported [24, 25, 26]: we are looking for such trapped waves along an infinite *straight* edge of a membrane here.

2. Localized waves traveling along the edge of a membrane

Consider a semi-infinite membrane under remote tension T (force per unit length) as shown in fig. 1. The stiffness of the elastic support, provided by the distributed foundation, in the interior of the membrane, is modeled by the Winkler parameter κ which represents the stiffness per unit area. This may be an oversimplified model of a membrane on soft tissues, for example, however it could be used as the simplest linear model to include the stiffness of a foundation when the entire membrane is supported and not just the edge. The equation of motion is given by

$$T\nabla^2 w - \kappa w = \rho h \ddot{w} \tag{1}$$

where $w(x,y,t)$ is the transverse deflection of the membrane that depends on the in-plane coordinates x and y and time t. A dot represents differentiation with respect to time. The dispersion relation for plane waves in this medium is well-known and is given by $\omega = c_M \sqrt{k^2 + (\tilde{k})^2}$, where $\tilde{k} = \sqrt{\frac{\kappa}{T}}$; the positive square root has been kept for a right-propagating wave. Below the cut-on frequency, given by $\omega^* = c_M \tilde{k}$, the wavenumber is not real–waves do not propagate spatially and are evanescent. A plane transverse wave in an unsupported membrane is non-dispersive and it travels at a speed $c_M = (T/\rho h)^{1/2}$ (the subscript stands for 'membrane'). All this background is well known.

We now look for a wave solution of eq. (1) of the form

$$w(x,y,t) = W(y)\exp[i(kx - \omega t)] \tag{2}$$

traveling along the edge $y = 0$ of the membrane. The profile of the waveform $W(y)$ is as yet an unknown function. Substituting this separable solution into (1), we have

$$W'' = \left(\frac{k^2 T + \kappa - \omega^2 \rho h}{T}\right) W, \tag{3}$$

where a prime represents differentiation with respect to y. The above differential equation admits solutions of the form $W(y) = e^{-sy}$, where

$$s_{\pm} = \pm\sqrt{k^2 + (\kappa/T) - (\omega^2/c_M^2)}. \tag{4}$$

The general solution for the y-dependent part of the wave is then given by

$$W(y) = c_1 \exp(-s_+ y) + c_2 \exp(-s_- y) \tag{5}$$

where c_1 and c_2 are arbitrary constants. At this stage we have four unknowns: ω, k, c_1 and c_2; whereas we have two boundary conditions on y: one each at $y = 0$ and $y \to \infty$. Applying these conditions will lead to the determination of one of the two 'amplitude parameters' c_1 and c_2; the second will remain unresolved. The frequency ω will be expressed as a function of the wavenumber k which is the dispersion relation. If a dispersion relation $\omega(k)$, when inserted into eq. (4), leads to a positive decay rate s, then the corresponding motion will be
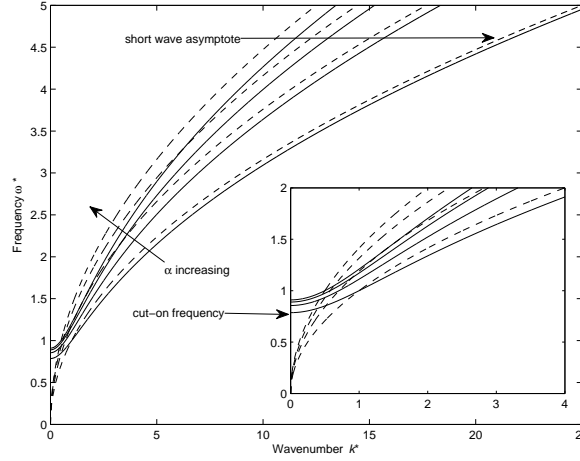
Figure 2. Dispersion relations for the trapped wave in semi-inf nite membrane supported on springs at the edge (solid lines). The short wave asymptote is a parabola in each case shown using dashed lines. The four solid curves correspond to $\alpha = 1, 2, 3, 4$, respectively.

associated with a trapped wave. In the following, we explore this possibility for a range of support and edge conditions.

The term with negative root in (5) must be discarded due to the boundary condition at inf nity (because the amplitude cannot grow monotonically with y). This means that $c_2 = 0$. If the membrane were free on its edge, then the boundary condition at the free edge would be given by $w'(x, 0, t) = 0$, which leads to $W'(0) = 0$. Substituting $W = c_1 \exp(-s_+ y)$ into this boundary condition, we obtain $-s_+ e^{-s_+ y}|_{y=0} = 0$ which implies that $s_+ = 0$. This means that the decay length scale for the sought edge wave is inf nite. Thus the 'edge wave' (2) is y-wise extended and it cannot be distinguished from the the straight-crested plane waves of the form $w(x, y, t) = W_0 e^{i(kx - \omega t)}$ traveling within the membrane. We, therefore, conclude that *localized edge waves in a semi-infinite membrane with a free edge are impossible to observe*. This is in contrast with the situation of thin plates and shells where such edge waves are known to exist. The case of laden edge, however, is qualitatively different and is discussed next.

Consider now the edge $y = 0$ laden with mass per unit length M (as a line mass) and the stiffness of the distributed spring at the edge per unit length K. The second boundary condition now becomes

$$Tw'(x, 0, t) - Kw(x, 0, t) - M\ddot{w}(x, 0, t) = 0. \tag{6}$$

If trapped waves exist, then we must have solutions having $s_+ > 0$ that are consistent with the above boundary condition. Substituting $W = c_1 \exp(-s_+ y)$ into (6) and combining with (4), we obtain an expression for the decay rate of the trapped wave–if it exists–as

$$s_+ = \frac{\omega^2 M - K}{T} = \sqrt{(k^2 T + \kappa - \omega^2 \rho h)/T} > 0. \tag{7}$$

The above equation contains both x-wise and y-wise dynamics. The edge-wise dynamics is characterized by the real wavenumber k–thus implying propagation. The y-wise dynamics is described by a real decay rate which is associated with imaginary wavenumber. Indeed,
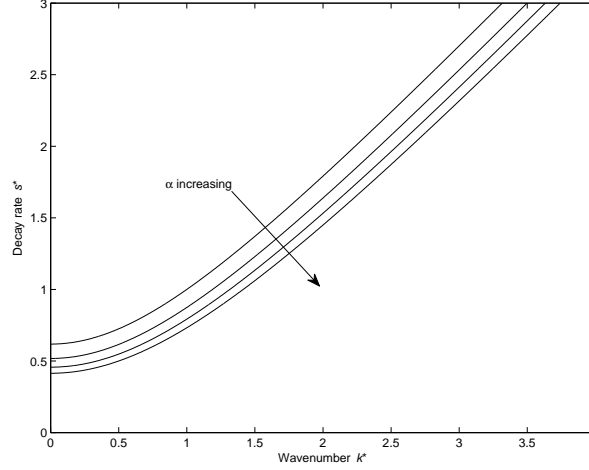
Figure 3. Decay rates for the trapped wave for $\alpha = 1, 2, 3, 4$. Increasing α decreases the decay rate for a given wavelength. Shorter waves decay faster.

we could have started with an assumed waveform having real wavenumber along the edge and an imaginary wavenumber in the direction perpendicular to it–instead of the one chosen here which has real wavenumber along and real decay rate across the edge. The edge-wise propagation behavior is described by a dispersion relation. Across the edge, a relationship between the decay rate and the frequency exists, which is the analogue of the dispersion relation for trapped motion. In this general setting, two conditions at the edge will be discussed, in turn, now–(a) when the edge is supported on distributed spring only; (b) when the edge is laden with distributed line mass but it is not supported.

2.1. (a) *Spring supported edge*

For this case, $M = 0$ and $K \neq 0$. Because we are looking for trapped waves, we require $s_+ > 0$. From equation (7), this is ruled out when $M = 0$ because $s_+ = (-K/T) < 0$. Therefore, trapped waves are not possible when the edge is not laden with mass.

2.2. (b) *Mass laden edge*

Consider the other extreme when the edge spring stiffness $K = 0$ but $M \neq 0$. Equation (7) now simplifes to

$$s_+ = \frac{\omega^2 M}{T} = \sqrt{(k^2 T + \kappa - \omega^2 \rho h)/T}.$$

(8)

For a specifed real wavenumber k, the second equality can be solved for the frequency compatible with traveling wave propagation which is the dispersion relation $D(\omega, k)$ in an implicit form. Squaring both sides, we obtain the following non-dimensionalized quadratic equation for the variable ω^{*2}

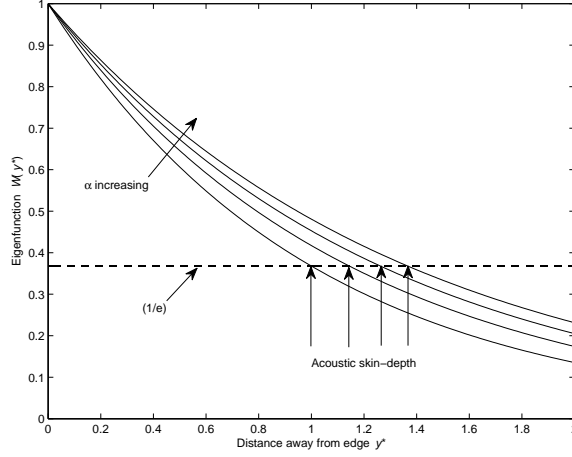$$(\omega^*)^4 + \alpha \omega^{*2} - \alpha(1 + k^{*2}) = 0$$

(9)

Figure 4. The across-the-edge part of the eigenfunctions $W^*(y^*)$ for the trapped mode. The skin-depth is def ned at $(1/e)$ attenuation in the wave amplitude. The non-dimensional parameter $\alpha = 1,2,3,4$ and the wavenumber $k^* = 1$.

where $\omega^* = \omega/(\sqrt{\kappa/\rho h})$, $k^* = k/\sqrt{\kappa/T}$, and $\alpha = T(\rho h)^2/(\kappa M^2)$. Solving this quadratic gives two solutions of which one is spuriously introduced while squaring (8) and must be rejected because ω^{*2} is positive. The result is the following dispersion relation that relates the wavenumber and the frequency

$$\omega^*(k^*) = \alpha^{1/2}\left[\frac{\sqrt{1+4\alpha^{-1}(1+k^{*2})}-1}{2}\right]^{1/2}, \tag{10}$$

which involves the properties of the membrane via the non-dimensional number α. The group velocity of the trapped wave as a function of wavenumber can be calculated by differentiating the above expression. In the long wave limit, the group velocity turns out to be zero. The dispersion relation possesses a cut-on frequency which is obtained by setting $k^* = 0$ in eq. (10). Below this critical frequency, there are no trapped waves traveling along the edge. This is fundamentally not a new behaviour for structures supported on elastic foundation. *Above* this critical frequency, however, waves localize away from the edge for all frequency and such waves must be termed 'trapped'. For membrane acoustics such trapped waves do not seem to have been reported so far. The dispersion curves for the trapped waves are plotted in f g. 2 using solid lines. The detail for long waves is shown in the inset of f g. 2. The cut-on frequency increases with increase in the non-dimensional parameter α and the whole curve shifts up. The short wave asymptote to the dispersion curve of the trapped wave in the limit $k^* \to \infty$ is given by

$$\omega^* \sim \alpha^{1/4}\sqrt{k^*}. \tag{11}$$

These asymptotes are shown in f g. 2 using dashed lines.

While the second equality in (8) describes the propagation behavior in the *x*-direction, the f rst part contains the spatial distribution of the wave in the *y*-direction which is conf ned
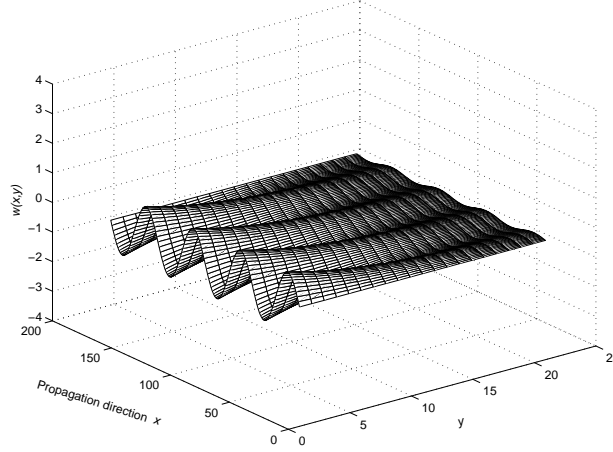
Figure 5. A snapshot of the trapped wave (8) traveling along the edge of a membrane supported elastically on its edge.

to the edge. The decay rate of the localized wave is given in the non-dimensional form by

$$s^* = \alpha^{-1/2}\omega^{*2}, \tag{12}$$

where $s^* = s\sqrt{(T/\kappa)}$. The plus subscript has been removed from the notation here onwards. Such localized dynamics is known in other physical contexts, e.g. the skin effect in conductors when they interact with electromagnetic waves. The skin-depth is given by δ; the current density scales as $e^{-d/\delta}$ at a distance d away from the surface. Mass laden membranes, therefore, afford an acoustic analogue of this physical behaviour. Drawing this analogy, the skin-depth for acoustic waves in laden membranes is the reciprocal of the decay rate and is given in the non-dimensional form by

$$\delta^* = 1/s^* = \sqrt{\alpha}/\omega^{*2} \tag{13}$$

which is in terms of the properties of the membrane and the frequency. Here the coordinate away from the edge and the skin-depth have been non-dimensionalized according to $y^* = y\sqrt{\kappa/T}$ and $\delta^* = \delta\sqrt{\kappa/T}$, respectively, so that the wave amplitude decays as e^{-y^*/δ^*}. It is evident that the skin-depth thus defined is the distance away from the edge where the wave amplitude becomes $1/e$ of its value at the edge.

The minimum value of the decay rate is in the long wave limit $k^* \to 0$. As we increase the wavenumber, the shorter the wave the greater is the decay rate. The decay rate is plotted as a function of the wavenumber for various values of the parameter α in fig. 3. In the short wave limit, the decay rate of the trapped wave and the acoustic skin-depth scale as

$$s^* \sim k^*, \quad \delta \sim \lambda \tag{14}$$

respectively, where λ is the wavelength. The straightening trend of the curves with increasing k^* in fig. 3 is consistent with this.

The eigenfunctions of the trapped mode are shown in fig. 4. The skin-depth could be defined arbitrarily as the depth at 50% attenuation (in the spirit of other decay processes, e.g. as in half-life). Instead we have chosen to define it as the depth at $1/e$ attenuation

in amplitude which is customary in skin-effect related physical phenomena. The acoustic skin-depth increases with increasing α as shown in f g. 4. A snapshot of the trapped wave decaying in the y-direction and propagating in the x-direction, which is described by (8), is shown in f g. 5. The wavenumber and the decay rate are arbitrarily chosen for illustration.

3. Conclusions

Trapped waves in semi-inf nite membranes having a straight edge were explored for two support conditions. Membranes with free edge do not possess edge waves. It was shown that waves propagating along the edge, but localized away from it, are admissible when the edge is laden with line mass. The resulting edge wave is dispersive and possesses a rich propagation behavior. The decay behavior is wavenumber dependent–shorter waves decay faster. The attenuation of these waves away from the edge was characterized in terms of suitable non-dimensional numbers.

[1] GRAFF K.F. *Wave motion in elastic solids* Dover, New York (1991).
[2] BREKHOVSKIKH L.M., *Waves in layered media*, Academic Press, New York (1960).
[3] PEKERIS C.L., *Proc. Nat. Acad. Sci.*, **41** (1955) 469.
[4] MCIVER P. and MCIVER M., *J. Fluid Mech.* **558** (2006) 53.
[5] LINTON C.M. and MCIVER P., *Wave Motion*, **45** (2007) 16.
[6] EVANS D. V. and LINTON C.M., *J. Fluid Mech.*, **225** (1991) 153.
[7] COBELLI P.J., PAGNEUX V., MAUREL A. and PETITJEANS P., *EPL*, **88** (2009) 20006.
[8] EVANS D.V., LEVITIN M., and VASSILIEV D., *J. Fluid Mech.* (1994) **261**, 21.
[9] OLINER A.A. Waveguides for surface waves (in *Acoustic Surface Waves*), Springer-Verlag, Berlin (1978).
[10] LORD RAYLEIGH, *Proc. London Math. Soc.* **17** (1885) 4.
[11] LOVE A.E.H., *Some problems in geodynamics*, Cambridge University Press (1911 and 1926).
[12] STONELEY R., *Proc. Roy. Soc.* **A106** (1924) 416.
[13] VIKTOROV I.A., *Rayleigh and Lamb waves: physical theory and applications*, Plenum Press, New York (1967).
[14] KONENKOV YU. K. *Sov. Phys. Acoust.* **6** (1960) 122-123.
[15] SINHA B.K. *J. Acoust. Soc. Am.* **56**, 16-18 (1974).
[16] THURSTON R.N. and MCKENNA J., *IEEE Trans. Sonics Ultrason.* **21** (1974) 296-297.
[17] NORRIS A.N., *J. Sound Vib.*, **171** (1994) 571.
[18] KAUFFMANN C., *J.. Acoust. Soc. Am.* **104**, (1998) 2220.
[19] NORRIS A.N., KRYLOV V.V., and ABRAHAMS I.D., *J. Acoust. Soc. Am.*, **107** (2000) 1781.
[20] KAPLUNOV J.D., KOSSOVICH L. YU., and WILDE M.V., *J. Acoust. Soc. Am.* **107** (2000) 1383.
[21] ZAKHAROV D.D., *Acoustical Phys.* **48** (2002) 171 [Translated from *Akust. Zhur.* **48**, (2002) 205.
[22] PORTER R., *Wave Motion*, **45**, (2007) 3.
[23] KAPLUNOV J.D. and SOROKIN S.V., *J. Acoust. Soc. Am.*, **97**, (6), (1995) 3898.
[24] KAPLUNOV J.D., ROGERSON G.A. and TOVSTOK P.E., *Quart. J. Mech. App. Math.*, **58** (2005) 645.
[25] GRIDIN D., CRASTER R.V., and ADAMOU A.T.I., *Proc. Roy. Soc. Lond.* **A461**, (2005) 1181.
[26] EWING M., JARDEZKY W.S., AND PRESS F., *Elastic Waves in Layered Media*, MCGRAW-HILL, NEY YORK (1957).

DETERMINATION OF STRESS INTENSITY FACTORS OF STRUCTURAL ELEMENTS BY SURFACE CRACKS

Marija Blažić[1], Katarina Maksimović[2], Yasmina Assoul[3]

[1]Military Technical Institute, Ratka Resanović 1, Belgrade
e-mail: blazicmarija@yahoo.com
[2] Republic Serbia, City Administration of City of Belgrade,
Secretariat for Utilities and Housing Services Water Management,
Kraljice Marije 1, 11120 Belgrade, Serbia
[3] Faculty of Engineering, Université Saâd Dahleb Blida, ALGÉRIA

Abstract. Stress analysis of the fractured structure is needed for estimation of its safety and reliability. Various methods have been used to obtain stress-intensity factors for surface and corner cracks in plates. The finite element technique had become an indispensable tool for the numerical solution of engineering problems and had appeared to be an ideal method to simulate the crack extension in structures. In this paper, stress intensity factors (SIF) are considered using finite element method, FEM with singularity elements. Attention is focused on a 3-d plate with elliptical surface crack under tension load. Graphic review of stress intensity factors (SIF) for a wide range of crack sizes is also determined. Accurate stress intensity factors for such cracks are necessary for reliable prediction of fatigue crack growth rates or fracture. Forman type fatigue growth law is used in this paper.

Key words: 3-d plate, elliptical crack, finite element analysis, stress intensity factors, cyclic loading, fatigue crack growth

1. Introduction

The use of the stress intensity factor in examining cracked structural problem requires an accurate knowledge of the stress field in the vicinity of the crack tip for the structural geometry, loading and boundary condition in question. Unfortunately, analytical solutions exist only for relatively simple cases wherein: the domain is considered to be infinite, the material is homogeneous, in most cases, is isotropic, and the boundary conditions are not complicated. To deal with practical problems of fracture mechanics, structures with finite size, arbitrary shape, general boundary conditions, and arbitrary material properties, numerical techniques such as finite elements and boundary integral methods are mandatory.

Semi-elliptic surface cracks frequently initiate and grow in the vicinity of high stresses, stress concentrations, thermal stresses and other non-linear stress fields. Such cracks are present during a large percentage of the useful life of these components. Hence, understanding the severity of surface cracks is important in the development of life prediction methodologies. Accurate stress intensity factors for such cracks are necessary for

reliable prediction of fatigue crack growth rates or fracture. Three-dimensional (3-D) stress analysis of crack configurations have received considerable attention in the literature in the last three decades [1-6].

The fatigue failure of plates often develops from surface defects, and therefore several authors have examined the stress-intensity factor variation along the front of these flaws. The assumption that an actual part-through crack can be replaced by an equivalent elliptical-arc edge flaw is experimentally supported, and therefore many analyses have been carried out related to this equivalent configuration [1-3]. The problem of fatigue propagation is very complex because the crack front can be modeled quite accurately by an elliptical arc during the whole phenomenon, but the aspect ratio of the ellipse changes under cyclic loading.

An elliptical-arc surface crack in a plate subjected to cyclic tension loading with constant amplitude is considered, Fig.1 . Surface fatigue cracks are frequently initiated in such components at the stress concentrating locations (such in the vicinity of the hole), then propagate into the interior of the parts and can cause final fracture abruptly. The three-dimensional elliptical arc has been used to model the crack front in plate under axial loading. In the first section of the present artical the stress intensity factors along the crack front are computed. The other part is reserved for fatigue crack propagation.

2. Stress Intensity Factor for elliptic surface crack in the plate

Many numerical analyses, theoretical studies and experimental investigations have been conducted to obtain stress intensity factors (SIFs) for three-dimensional (3D) cracked bodies. In the beginning, finite element method offers simple procedures for extrapolation of the crack tip intensity factors. But the limitation of the number of the finite elements around the crack tip and the precision of the determination of the toughness lead to the development of special crack elements which simulate the complete crack zone stress eld.
Three-dimensional finite elements were used to model a plate containing a semi-elliptic surface crack. The finite element analyses were made using MSC/NASTRAN, with 20-noded isoparametric three-dimensional solid elements. In order to model the inverse square root singularity at the crack tip, three-dimensional prism elements with four mid-side nodes at the quarter points (a degenerate cube with one face collapsed) were used and the separate crack tip nodal points were constrained to have the same displacements [3]. The quarter-point displacement FEM was employed in present work to evaluate stress intensity factors along semi-elliptic crack front. This method uses the out-of –plane displacement value at the quarter-point behind the crack tip, as shown in Fig. 1, to extract the SIF through the following relationships

$$K_I = \frac{E\, u_{z(1/4)}}{4(1-\nu^2)} \sqrt{\frac{2\pi}{r_{(1/4)}}} \qquad (1)$$

where E is the Young's modulus and $r_{(1/4)}$ is the distance of the quarter-point away the crack tip. Note that the $r^{-1/2}$ singularity of the near crack tip stress field vanishes at the intersection of three free surfaces [3] such as the surface point of the crack. Hovever, for

375

engineering material with Poisson`s ratio of 0.3, the dominant singularity is $r^{-0.4523}$, which is not a large deviation from $r^{-1/2}$.
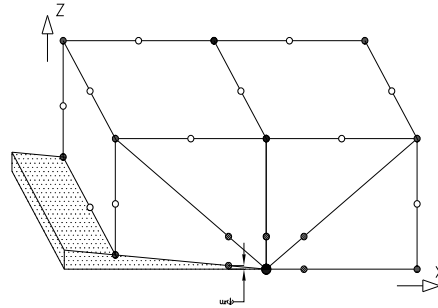

Fig. 1. The quarter-point displacement method (Super-element)

The equation (1) is valid for the plane strain assumption, which is employed throughout this work, and can be derived from the well-known displacement solution adjacent to the crack tip for Mode I crack, i.e.

$$u_z = \frac{2(1+v)K_I}{E}\sqrt{\frac{r}{2\pi}}\sin\frac{\theta}{2}\left(2-2v-\cos^2\frac{\theta}{2}\right) \qquad (2)$$

With the square-root singularity simulated this method has been verified to be of good accuracy for calculating of the stress intensity factors of a variety of practical cracked geometries [3,7].

For this purpose, the finite-element models of plate with semi-elliptic surface crack are subjected to tensile loading, $\sigma_{max} = 10\frac{daN}{mm^2}$. Plate made of 7075 T7351 is being analyzed. Young's modulus, E = 73174[daN/mm²] and Poisson's ratio, v=0.33 are assumed. Axial tensile stress has been applied to the end of the plate and the last layer of elements at the end of the plate has been constrained to move in the axial direction.

Geometry properties of this plate are: width 2W=120 mm, thickness t=10 mm, height 2H=70mm, the hole radius R=10 mm, length of surface crack a=10 mm, b depth of surface crack, a=b Fig. 2. The half height of the plate and width are chosen to be large enough to have a negligible effect on the stress intensity factors (W/H=1.714) and W/R is selected to be 6.
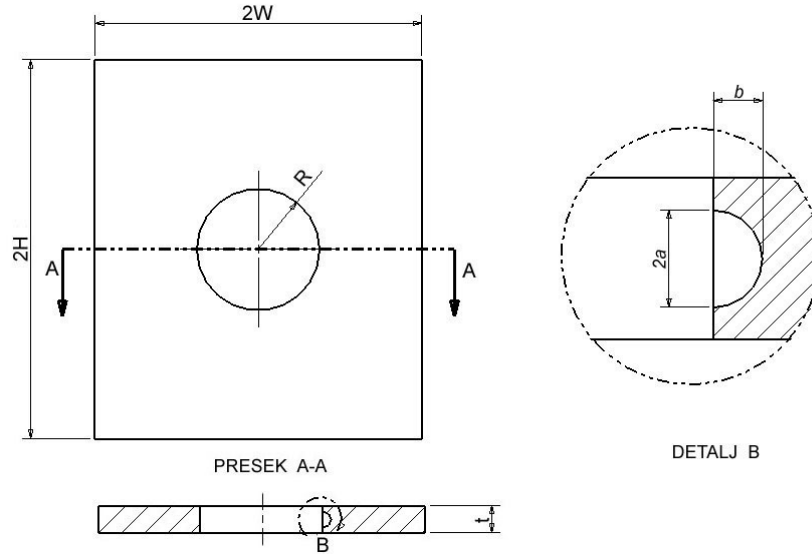
Figure 2.   Elliptical-arc surface flaw in a round bar, geometrical parameters

Three-dimensional finite element (FE) models with 20-node singular finite elements arranged around the crack tip will be used to calculate the SIFs of elliptical surface cracks in plate.

The fact that the crack geometry must be explicitly meshed and that significant refinement in the vicinity of the crack fronts is needed to achieve reasonable accuracy renders finite element based methods particularly difficult to implement. This meshing difficulty is particularly acute in three dimensions. Meshing and re-meshing become, in such circumstances, a particularly large part of the computation time. High mesh density in the crack front region is required. The stress-intensity factor is obtained for all values of geometrical parameters b. These direction of tensile loads cause only mode I deformations. The resultants are given in the Table 1.

Parameters b	Stress intensity factor
b (mm)	$\mathrm{K_I}\left(\dfrac{daN}{mm^{3/2}}\right)$
1.18	45.5
1.76	52.1
2.05	54.7
2.63	63
2.83	67.5
3.21	71.8

Table 1. Stress-intensity factor against crack depth b at deepest point

Using discrete values of the of the stress intensity factors Table 1, determined by FEM, the analytic expression of the (SIF) can be defined in the next form:

$$K_I = 286.57 - 690.97b + 752.11b^2 - 390.12b^3 + 97.856b^4 - 9.485b^5 \qquad (3)$$

The corrective function can be defined in the next form:

$$Y = 3.3078 - 1.2314b + 0.4158b^2 - 0.0416b^3 \qquad (4)$$

where b depth of surface crack, a=b Fig. 2.
Figures 3., 4., 6. and figure 7. shows the stress field, σ obtained for next values of b : 1.18 , 1.76 , 2.05, 2.63, 2.83 and 3.21. The values for σ are given in daN/mm^2.
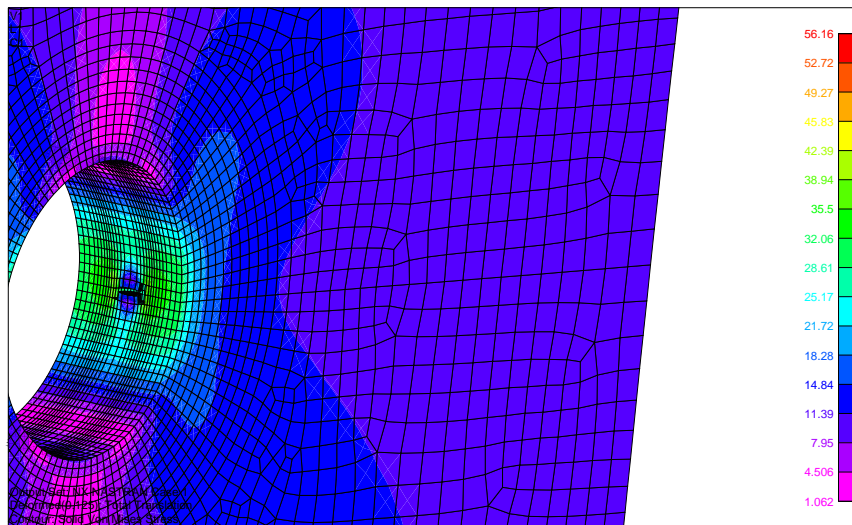
Figure 3. Stress field in the plate with hollow surface crack, crack depth b=1.18mm

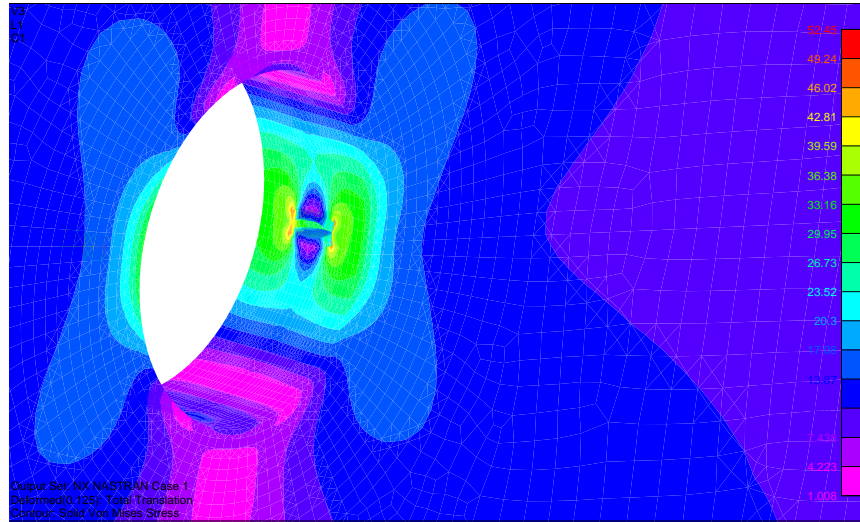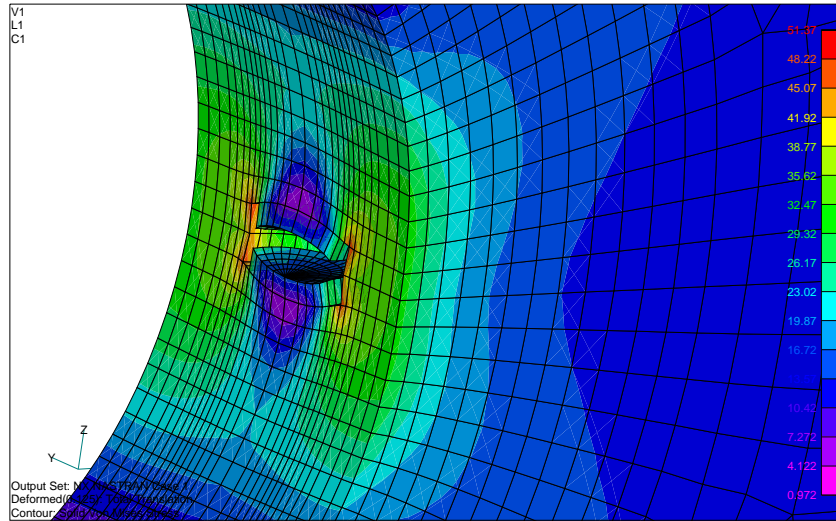**Figure 4.** Stress field in the plate with hollow surface crack, crack depth b=1.76mm

Figure 5. Stress field in the plate around crack tip b=2.05mm

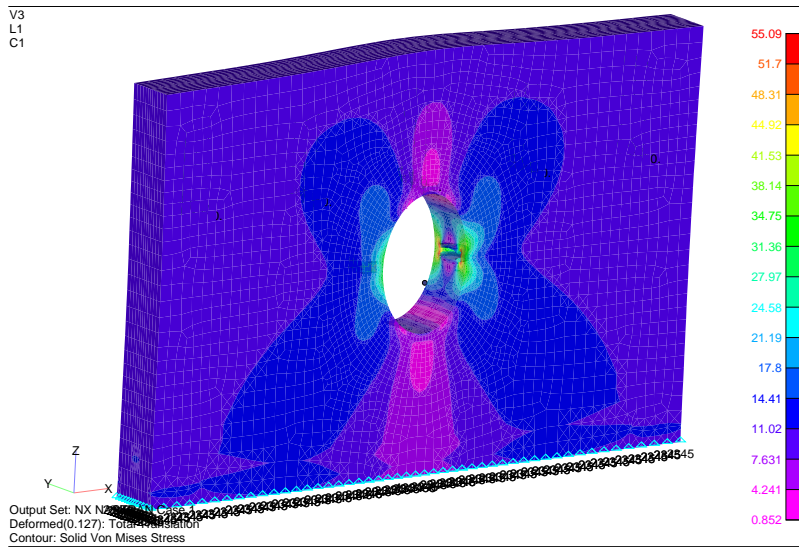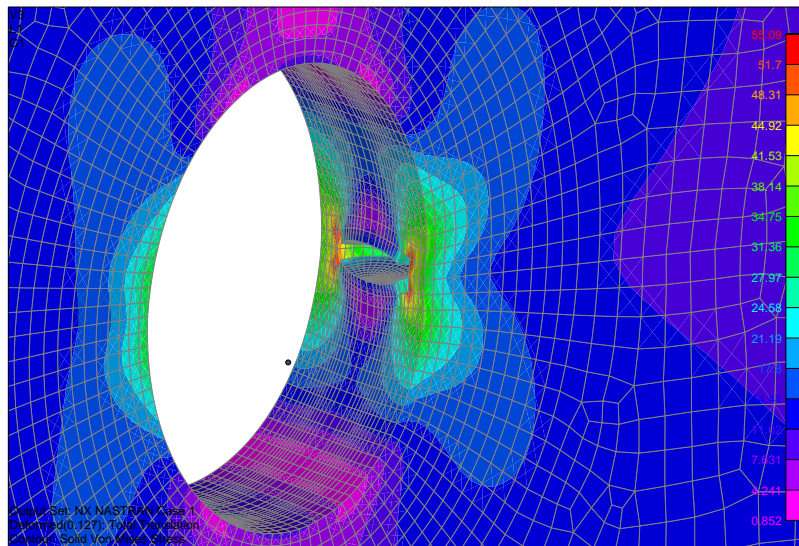**Figure 6.** Stress field in the plate with crack , b=3.21mm

Figure 7. Stress field in the plate around crack tip, b=3.21mm

4. Fatique Crack Growth

Accurate prediction of fatigue crack growth for cracks initiating and developing along the bores of fastener holes in plate are required because of the wide existence of this problem in practical components and structure. Several authors have analytically [6] and experimentally deduced that the front of a surface flaw in a metallic plate can be modeled quite accurately by an elliptical arc during the whole fatigue growth [4,5].

Plate of previously mentioned geometry has been subjected to cyclic axial loading with constant amplitude. The stress-intensity factor equations developed for surface cracks are used herein to predict fatigue-crack-growth patterns under load spectra. For this purpose Foreman`s model is used.

Forman's equation has been developed primarily in order to model the domain of unstable crack growth. The area of unstable crack growth is basically interesting in situations where the crack growth time due order of 10^3 cycles. It is certainly good to point out that Paris equation is regularly used in the domain of stable crack growth. Under stable crack growth inplies the area where the slope log(da)/dN (as a function of logΔK) has approximately linear character.

The initial crack size is b_o= 0.00118m. Cyclic characteristics aluminum 7075 T7351 for Forman model are $C_f = 3 \cdot 10^{-7}$, $n_f = 2.39$ and fracture toughness is $K_{IC} = 2225 \dfrac{N}{mm^{3/2}}$.
The fatigue life prediction is examined for four different values of loading ratio, R(0, 0.1, 0.3, 0.5).

Plate is loaded by cyclic loads with different values of the loading ratio R but with constant amplitude. The value of maximum stress is always the same, $\sigma_{max} = 100 \dfrac{N}{mm^2}$, the value σ_{min} changes depending on the loading ratio. All calculated values for the number of cycles till failure for different R are shown in Fig. 8.
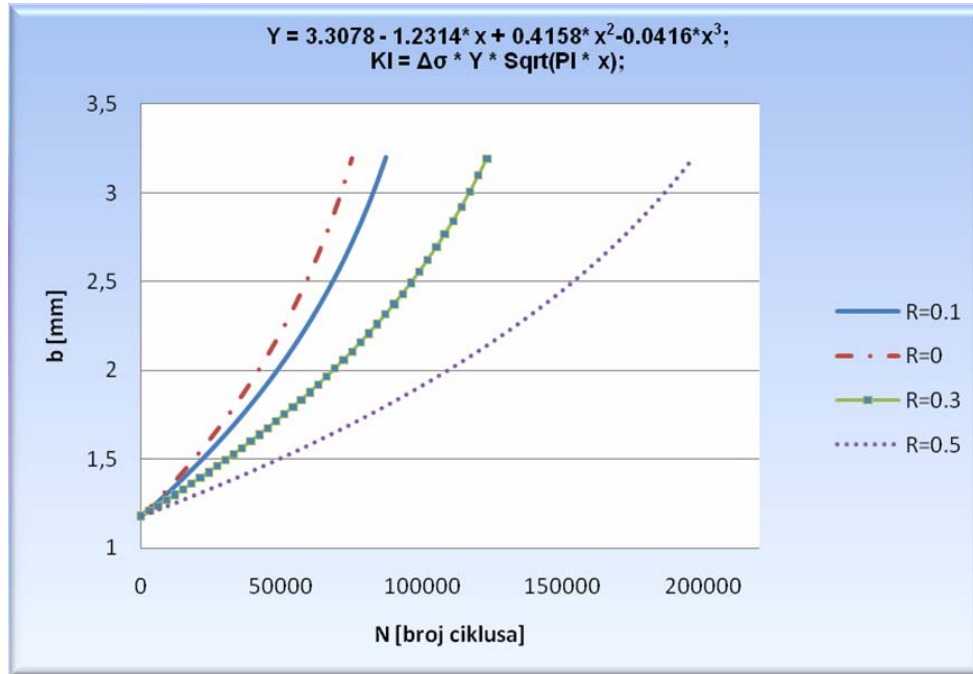
Figure 8. Surface crack growth under load spectra (four cases of stress range)

5. Conclusions

In this work the fracture mechanics parameters are considered. Attention is focused on a plate with elliptical surface crack under tension load. SIFs of surface cracks in plate are studied systematically by using the 3D FE method with 20-node singular elements arranged around the crack border.

Stress intensity factors are determined by singular finite elements for various the crack depth. Using these discrete values of the stress intensity factors analytic expressions are derived for general stress intensity factors. An empirical expression for the SIFs as a function of crack geometry is obtained by fitting the numerical results. These analytic expressions are used in crack growth analysis of cracked structural component. Therefore, the empirical expression can be used conveniently in life prediction of notched bars with various notch geometry and stress concentration coefficients at least within the range of parameters studied in this work.

Acknowledgments

5. References

[1]   Maksimović K (2006) Vera Nikolić-Stanojević, Stevan Maksimović, Modeling of the Surface Cracks and Fatigue Life Estimation, ECF 16, *16th European Conference of Fracture*, Alexandroupolis, Grčka.

[2]   Максимовић С и Блажић М (2006) Неки аспекти примене густине енергије деформације и МКЕ у анализи лома конструкција, *Техничка дијагностика*, бр 3-4.

[3]   D.M Tracey, 3D elastic singularity element for evaluation of *K* along an arbitrary crack front. Int. J. Fracture 9, 340-343 (1973).

[4]   Carpinteri, A. in 'Handbook of Fatigue Crack Propagation in Metallic Structures' (Ed. A. Carpinteri), Elsevier Science Publishers, Amsterdam, 1994, pp. 653-705

[5]   Boukharouba, T., Chehimi, C., Gilgert, J. and Piuvinage, G. (1994) in '*Handbook of Fatigue Crack Propagation in Metallic Structures*' (Ed. A. Carpinteri), Elsevier Science Publishers, Amsterdam, pp. 707-731

[6]   Nishioka T, Alturi SN (1983) Analytical solution for elliptical cracks and finite element alternating method for elliptical surface cracks subjected to arbitrary loadings, *Engineering Fracture Mechanics;*17:247–68.

[7]   J. C. Newman, Jr and I. S. Raju, Analysis of surface cracks in finite plates under tension and bending loads. NASA TP-1578 (1979).

STABILITY ANALYSIS OF LAYERED COMPOSITE PANELS BY FINITE ELEMENTS

Marko Bojanić[1]

[1] Military Technical Institute
Ratka Resanovića 1, 11000 Belgrade, Serbia
e-mail: bojanic.marko@gmail.com

Abstract: Buckling and postbuckling of anisotropic laminated thin shells by finite element method is compared with analytical and empirical data. The material of each layer of the shell is assumed to be linearly elastic, anisotropic and fiber-reinforced. A postbuckling analysis is presented for axially loaded anisotropic laminated cylindrical shells with different values of shell parameters and stacking sequence. The effects of material orthotropy on geometric nonlinear behavior are analyzed. For this purpose high-quality 4-node shell finite elements are used. Numerical examples demonstrate validity of the computation procedure in domain of geometric nonlinear problems.

Key words: Geometric nonlinearity, Finite elements, Plates and shells, Composite panels

1. Introduction

Composite laminated structures are being increasingly used in aeronautical and aerospace construction. Their components are often subjected to combinations of mechanical and thermal loading. In fact, many structures are subjected to high load levels that many results in nonlinear load-deflection relationships due to large deformations of the plate. One of the important problems deserving special attention is the study of their nonlinear response to large deflections and postbuckling.

Many studies according to classical plate theory for the large deflection of multilayered composite plates subjected to mechanical or thermal loading are available in literature [1,2]. Numerous studies involving the application of the shear deformation plate theory to nonlinear bending analysis can be found in Refs. [3-5]. The analysis of the buckling and postbuckling behaviour of isotropic or composite laminated shells is a topic of considerable technical importance in number of branches of engineering. Such behaviour may result from mechanical loading or from thermal loading or from a combination of the two, i.e. from thermomechanical loading. A book edited by Turvey and Marshall [8] contains much information on available methods, particularly as related to flat, rectangular plates, and includes details of several hundred pertinent references dating up until the mid-1990s. A large part of this literature, however, is naturally concerned with buckling under mechanical loading. In this paper the particular concern is with the nonlinear analysis under thermo-mechanical loading of isotropic/composite shell type structures.

Present paper gives description of the use of finite element method (FEM) in predicting the buckling and postbuckling response of axially loaded laminated cylindrical shells with different values of shell parameters and stacking sequence.

2. Nonlinear Analysis

The nonlinearity in structural problems can be of two types: (1) the geometric nonlinearity, which is associated with the changing geometry of a structure, and (2) material nonlinearity which is associated with the nonlinear behavior (stress-strain relations). Often a combination of the two is present when materials are loaded to their ultimate loads. The phenomena of plasticity, creep or other complex constitutive relations come under the class of material nonlinearity. The geometric nonlinearity enters the equations of equilibrium via the strain-displacement relations and the govering equations. Since the finite element method has proved to be a very powerful tool for analyzing elastic structural problems, involving complex geometries, variety of loading and boundary conditions, it is quite natural to extend this technique to the solution of nonlinear problems.

The governing equation can be used to study the linear/nonlinear static and eigenvalue buckling analysis.Governing equation for the deformation of the shell can be written as [4, 11]

$$[[K] - [K_T] + [K_G] + \frac{1}{2}[N_1(\delta)] + \frac{1}{3}[N_2(\delta)]]\{\delta\} = \{F_M\} + \{F_T\} \quad (2.1)$$

where $[K]$ is the linear stiffness matrix, $[N_1]$ and $[N_2]$ are nonlinear stiffness matrices linearly and quadratically dependent on the field variables, respectively, $[K_T]$ and $[K_G]$ are the geometric stiffness matrices due to thermal and initial stress resultants. $\{F_M\}$ and $\{F_T\}$ are mechanical and thermal load vectors, δ is the vector of degrees of freedom associated to the displacement field in a finite element discretisation.

The governing equation (2.1) can be used to study the linear/nonlinear static and eigenvalue buckling analysis by neglecting the appropriate terms as:

a) Linear static analysis:

$$[K]\{\delta\} = \{F_M\} + \{F_T\} \quad\quad\quad (2.2)$$

b) Nonlinear static analysis:

$$[[K] - [K_T] + \frac{1}{2}[N_1(\delta)] + \frac{1}{3}[N_2(\delta)]]\{\delta\} = \{F_M\} + \{F_T\} \quad\quad (2.3)$$

c) Eigenvalue buckling analysis:

$$[K]\{\delta\} = \Delta T[K_G^*] \quad\quad\quad (2.4)$$

where $[K_G^*]$ is the geometric stiffness due initial state of stress developed because of unit uniform temperature rise and ΔT is the temperature rise. It may be noted here that for the purpose of evaluating $[K_G^*]$, firstly the static analysis of the shell using Eq. (2.2) for unit temperature rise is carried out. The resulting deformation filed is used to calculate the initial state of stress resultants using Mindlin formulation [1, 4] for displacements of plate and in turn, for evaluating the $[K_G^*]$ matrix. The nonlinear prebuckling axisymmetric deformation followed by postbuckling equilibrium path (a symmetric deformation) is traced by solving Eq. (2.3) using Newton–Raphson iteration procedure coupled with displacement control

method [12]. The equilibrium is achieved for each load/displacement step until the convergence criteria suggested by Bergan and Clough [13] are satisfied within the specific tolerance limit of less than 1%.

3. Numerical Examples

To illustrate nonlinear behavior of laminated composite structures numerical examples are included.

D = 701.2 mm, L = 540 mm

Material properties:

Material 1:
$E_{11} = E_{22} = 52,0$ GPa, $G_{12} = 2,35$ GPa,
$\nu = 0.302$,
t = 1,32 mm

Material 2:
$E_{11} = 113,0$ GPa, $E_{22} = 9,0$ GPa,
$G_{12} = 3,82$ GPa,
$\nu = 0.73$; t = 1,2 mm

Material 3:
$E_{11} = 113,0$ GPa, $E_{22} = 9,0$ GPa,
$G_{12} = 3,82$ GPa,
$\nu = 0.73$; t = 1,5 mm

Stacking sequences:
$(0/\pm45/0)_T$, material 1
$(\pm45)_S$, material 1
$(\pm45)_{2S}$, material 2
$(90/0)_{2S}$, material 2
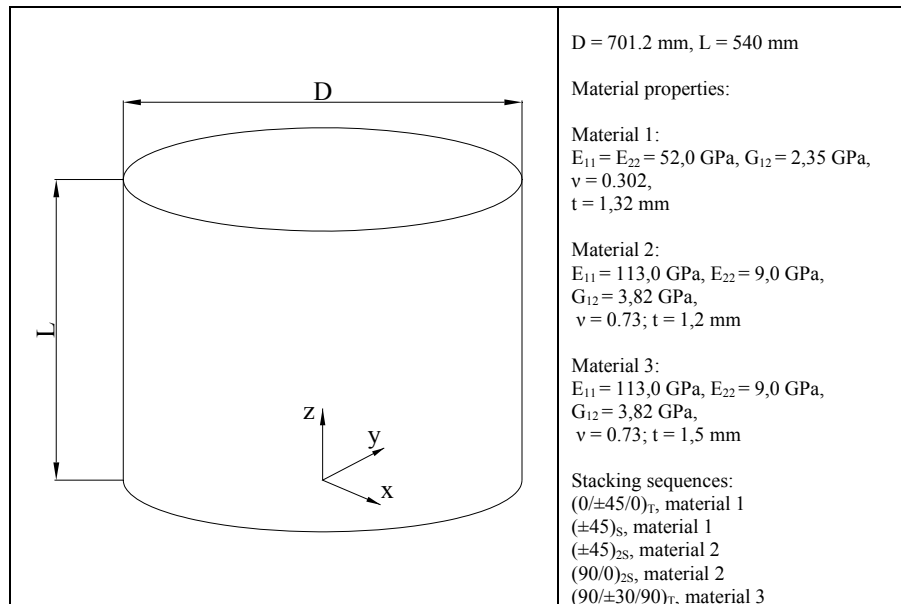$(90/\pm30/90)_T$, material 3

Figure 3.1 Geometry and material properties of cylindrical shell

This validation problem concerns the buckling and postbuckling response of a laminated cylindrical shell to axial compression. In design processes where such loading is a concern, this type analysis is important to identify the effects of variations in laminate stacking sequence, fiber orientation, and number of layers and aspect ratio of the shells on their stability. Experimental and analytical results /1/ are given in Table 3.1 along with results of finite element method. Geometry, material properties and stacking sequences are given in Figure 3.1. All models have identical basic geometry but differ in stacking sequences and material properties. The boundary conditions imposed on the model are along the top and bottom edges :

Along the bottom edge (z = 0): u = v = w = 0
Along the top edge (z = L): axial load is applied via rigid element.

Axial loading is achieved by applying translation in negative z direction. Resulting deformations for linear buckling FE analysis as well as for nonlinear FE analysis is shown in Figures 3.2 to 3.5. Postbuckling load–shortening curves for $(0/\pm45/0)_T$ and $(\pm45)_{2S}$

laminated cylindrical shells under axial compression aquired by FEM are compared in Figures 3.6 and 3.7 with data from [1].

Table 3.1

Material/Stacking	$F_{crEXP/1/}$ [kN]	$F_{crAN1/1/}$ [kN]	$F_{crAN2/1/}$ [kN]	Present FEM	
				F_{crLB} [kN]	F_{crNL} [kN]
$(0/\pm45/0)_T$, material 1	172.9	240.0	246.0	240.7	262
$(\pm45)_S$, material 1	120.2	120.6	149.7	118.4	113
$(\pm45)_{2S}$, material 2	92.3	173.7	147.6	119.7	115
$(90/0)_{2S}$, material 2	92.0	170.0	118.5	118.7	209
$(90/\pm30/90)_T$, material 3	196.2	289.0	248.8	174.2	244
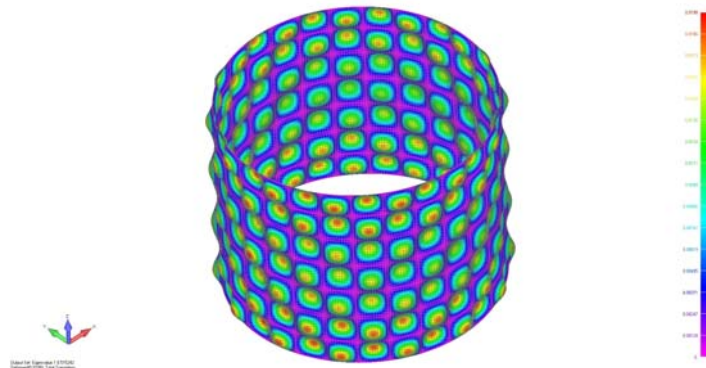
Figure 3.2 The first buckling mode using linear Eigen-value method for model with $(0/\pm45/0)_T$ stacking sequence and material 1
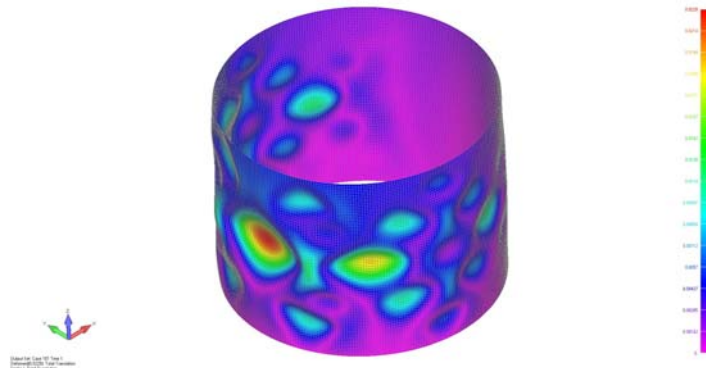

Figure 3.3 Displacement distribution obtained with nonlinear analysis for model with $(0/\pm45/0)_T$ stacking sequence and material 1
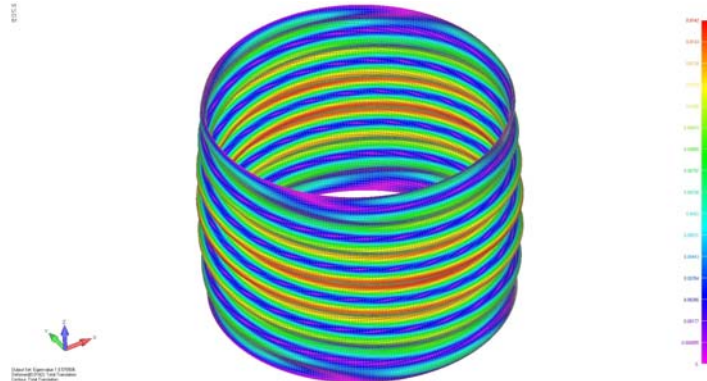
Figure 3.4 The first buckling mode using linear Eigen-value method for model with $(\pm45)_{2S}$ stacking sequence and material 2
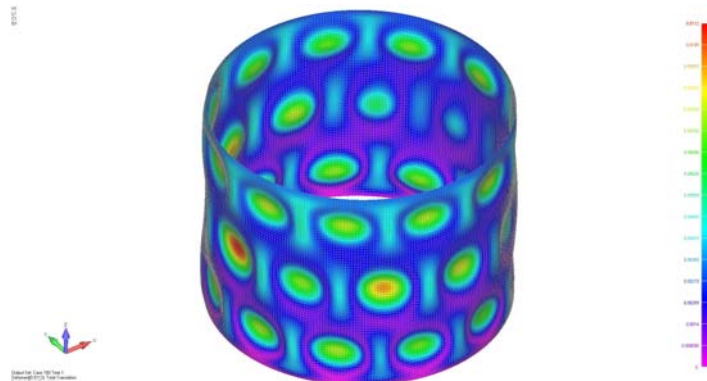

Figure 3.5 Displacement distribution obtained with nonlinear analysis for model with $(\pm45)_{2S}$ stacking sequence and material 2
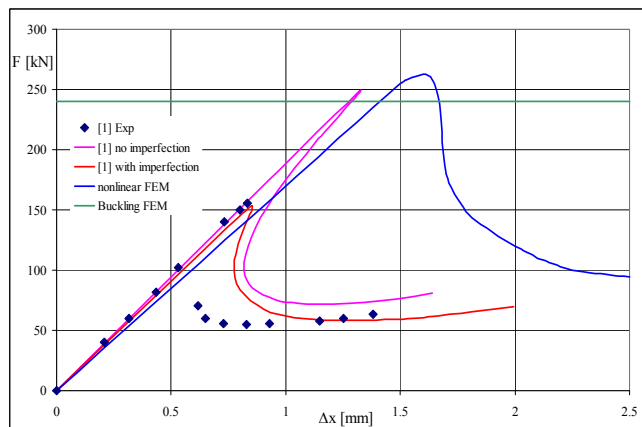

Figure 3.6 Comparison of postbuckling load-shortening curves with values obtained by FEM for model with $(0/\pm45/0)_T$ stacking sequence and material 1
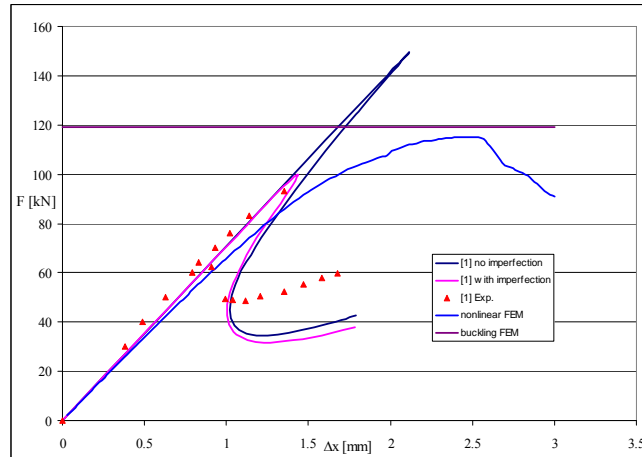
Figure 3.7 Comparison of postbuckling load-shortening curves with values obtained by FEM for model with $(\pm 45)_{2S}$ stacking sequence and material 2

4. Conclusions

Finite element method capability has been considered for predicting the geometric nonlinear behavior including buckling and postbuckling response of axially loaded composite laminated cylindrical shells.

Results presented in Table 3.1 show that nonlinear analysis as well as linear buckling analysis are in reasonable agreement with other analytical methods and in fact, in some cases (such as $(\pm 45)_S$, material 1), give results comparable with experimental data. One of the main reasons for result discrepancies is inability to accurately apply axial loading to finite element model. The problem with loading is best described by post buckling curves in Figures 3.6 and 3.7. The postbuckling path in Figure 3.6 has the correct general form but is offset by a large margin. Figure 3.7 paints even worse picture. Also FEM considers ideal geometry and every ply is identical in dimensions and characteristics (initial imperfection must be introduced) while in practice it is not so. Further exploration of this problem could provide better results for postbuckling behavior.

Nonlinear analysis can be used to determine buckling and postbuckling behavior of composite cylindrical shells, but great attention must be given to application of boundary conditions as well as to size and position of initial imperfection.

References

[1]   Hui-Shen Shen. Boundary layer theory for the buckling and postbuckling of an anisotropic laminated cylindrical shell. Part I: Prediction under axial compression. Composite Structures 2008; 82:346-361.
[2]   Reddy, J.N., Exact Solutions of moderately thick laminated shells, J. Engng. Mechanics, ASCE, Vol. 110, 1984, 794-809.

389

[3]   Maksimović, S., Improved geometrically nonlinear finite element analysis and failure fiber reinforced composite laminates, Proc. of Fourth Int. Symp. on Brittle Matrix Composites, Warsaw, Poland, 13-15 Sept. 1994, Eds. Brandt, A. M., Li, V. C. and Marshall, I. H., Woodhead Publ. Lim. Cambridge 1994

[4]   Maksimović, S. Instability analysis of layered composite structures using shell finite elements based on the third order theory, J. Applied Composite Materials, Vol.3, 301-309, 1996.

[5]   Turvey G.J., Marshall I.H., editors, Buckling and postbuckling of composite plates, London: Chapman & Hall; 1995.

[6]   Bojanić M., Stability Analysis of Thin Walled Structures Subjected to Thermal and Mechanical Loads, Scientific Technical Review,Vol. LVIII, No. 3-4, 2008; 21-25.

[7]   Maksimović, S., Kojić, M.,..., Geometric and material nonlinear analysis of layered fiber reinforced composite structures: Numerical and experimental study, IV Int. Conference on Computational Plasticity, 3-6. April 1995, Barcelona, Spain.

NUMERICAL MODELING OF SEMI-ELLIPTICAL CRACK GROWTH UNDER CYCLIC LOADING

Slobodanka Boljanović[1], Stevan Maksimović[1], Andrea Carpinteri[2]

[1] VTI – Aeronautical Department
Ratka Resanovića 1, 11000 Belgrade, Serbia
e-mail: djobo@beotel.rs, s.maksimovic@open.telekom.rs
[2] Faculty of Civil Engineering,
The University of Parma, Viale G.P. Usberti 181/A, 43100 Parma, Italy
e-mail: andrea.carpinteri@unipr.it

Abstract. The objective of the present paper is to develop a mathematical model for simulation of the fatigue life of structural components with semi-elliptical crack. For this purpose authors used adequate criteria. Applied criteria are based on the fact that during cyclic loading near the crack tip, plastic deformations occur and they leave behind the crack tip at a growing crack. Moreover, knowledge of the crack tip stress intensity factor as a function of applied load and geometry of the structure is necessary for fatigue life evaluation of cracked structures. In this paper, the stress intensity factors are examined using analytical and numerical approaches. As a numerical approach finite element method is applied.
A proposed mathematical model is validated using results of available experiments. A comparison of the numerically determined fatigue crack growth life with the experimental data shows a good agreement.

1. Introduction

Fatigue is perhaps the most common cause of crack initiation and growth which ultimately results in the fracture of a structure or components. The primary concerns of a fatigue designer are to achieve life of structural component and minimize the consequence of failure. The ability to predict fatigue crack propagation is essential to damage tolerance design in engineering application.

So far engineering practice has shown that often besides the through thickness cracks, surface cracks must be analyzed, too. As a special type of surface cracks in crack growth analysis, semi-elliptical cracks could be analyzed. These cracks must be carefully analyzed in the case of aircraft and aerospace vehicle components but also with many primary coolant piping systems in nuclear power plants. In this paper is considered fatigue life estimation of a semi-elliptical circumferential surface crack in a pipe subjected to a bending moment as well as aircraft component subjected to tensile loading. Several scientists, [1-9] have examined and analyzed the behavior of a semi-elliptical surface cracks. In fracture mechanics, different mathematical/numerical methods with the availability of powerful computers can be used for stress analysis of surface crack problems. The most widely applied technique is the finite element method [1-3] for solving fracture related problems. The weight function method [4,5], the alternating method [6] and the line-spring model [7]

are also used for dealing with semi-elliptical crack problems. Additionally, the boundary integral equation method [8] is applicable to solve semi-elliptical crack problems.

In this study, the computational model for fatigue crack growth analysis of components with external semi-elliptical crack is proposed. The stress intensity factors are computed by applying analytical and numerical approaches. In fatigue crack growth estimation, authors have examined how adequately, by application of equations of a stress intensity factor for a plate with semi-elliptical crack, residual service life of a pipe with external semi-elliptical crack could be calculated. The estimations of proposed fatigue crack growth model under a constant amplitude loading are compared with experimental fatigue results available in the literature

2. Stress intensity factor

Highly stressed engineering structures may contain crack-like flaws, and they may develop in complex surface crack problems during their service life. The existence of such cracks and their subsequent growth can cause a loss of strength and a reduction in the service life of a structure. It is therefore very important that the stress field around a cracked structure subjected to various kind of loading conditions is accurately determined The effects of the stress field, the crack size and shape, and the local structural geometry are analyzed by the parameter known as stress intensity factor.

Generally, experimental tests, analytical and numerical approaches can be used to analyze stress intensity factors for surface cracked components. However, it is known that fatigue tests are very time-consuming and crack initiation and propagation are extremely difficult to be monitored accurately. Due to that fact, present authors considered both, analytical and numerical approaches for the calculation of stress intensity factor in order to formulate numerical procedure for fatigue life estimation of surface cracked component, i.e. the pipe with external semi-elliptical crack (Fig.1). Actually, it is analyzed if fatigue life up to failure of the pipe can be adequately calculated by applying analytical relations for stress intensity factor which are commonly used in the case of a finite plate [9,10]. Thereby, the pipe is approximated by the plate with width $2\pi R_0$ and thickness t. In addition, it is assumed that the plate is subjected to tensile stress which is equal to the bending stress.
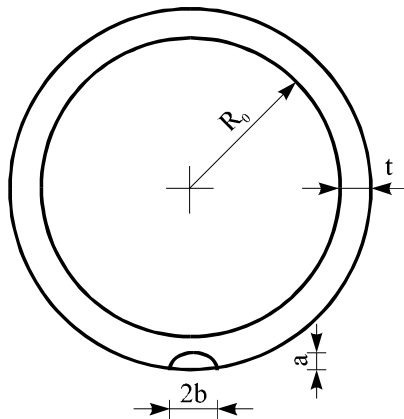

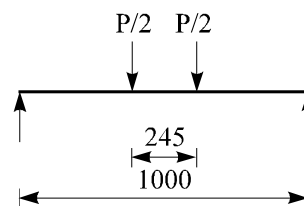**Figure 1.** Geometry of a pipe.   **Figure 2.** Loading condition. All dimensions are in mm.

The relation for stress intensity factor range in the case of a finite plate, at a point on the semi-elliptical crack front defined by the angle ϕ can be expressed as:

$$\Delta K_I(\phi) = \Delta S \sqrt{\frac{\pi a}{Q}} \left(M_1 + M_2 \left(\frac{a}{t}\right)^2 + M_3 \left(\frac{a}{t}\right)^4 \right) f(\phi) g\, f_w \qquad (1)$$

where ΔS is external stress range, Q presents the shape factor. Expression in apprentices together with $f(\phi)$, g, f_w presents the boundary correction factor and M_1, M_2, M_3 are factors depending of depth crack length a and surface crack length b, i.e.:

$$M_1 = 1.13 - 0.09\frac{a}{b}, \qquad (2)$$

$$M_2 = -0.54 + \frac{0.89}{0.2 + \dfrac{a}{b}}, \qquad (3)$$

$$M_3 = 0.5 - \frac{1}{0.65 + \dfrac{a}{b}} + 14\left(1 - \frac{a}{b}\right)^{24}, \qquad (4)$$

$$Q = 1 + 1.47\left(\frac{a}{b}\right)^{1.64}, \qquad (5)$$

$f(\phi)$ is factor depending of depth crack length a, surface crack length b and angle ϕ:

$$f(\phi) = \left(\left(\frac{a}{b}\right)^2 \cos^2\phi + \sin^2\phi\right)^{0.25}, \qquad (6)$$

g is factor depending of depth crack length a, thickness t, as well as angle ϕ:

$$g = 1 + \left(0.1 + 0.35\left(\frac{a}{t}\right)^2\right)(1 - \sin\phi)^2 \qquad (7)$$

and factor f_w can be expressed like:

$$f_w = \left(\sec\left(\frac{\pi b}{2w}\sqrt{\frac{a}{t}}\right)\right)^{0.5}. \qquad (8)$$

In this paper, relations for the stress intensity factor (Eqs. (1)-(8)) are used for stress analysis and fatigue life estimation. Moreover, in the section 4, the stress intensity factors

for the pipe are calculated by applying numerical approach (Finite element method) but without an assumption for the pipe that it is the finite plate.

3. Fatigue crack growth estimation

Fracture mechanics is being successfully used for the fatigue crack growth analysis of components. In general, the most important is to formulate the relation between fatigue crack growth rate and stress intensity factor. Due to the fact that a surface crack is analyzed, it is necessary to define the fatigue crack growth rate in the depth direction A and surface length direction B. Two coupled Paris fatigue laws for surface crack can be expressed as:

$$\frac{da}{dN} = C_A \left(\Delta K_A \right)^{m_A}, \quad \frac{db}{dN} = C_B \left(\Delta K_B \right)^{m_B} \tag{9}$$

where C_A, C_B, m_A and m_B are the material constants, ΔK_A, ΔK_B denote the stress intensity factor ranges at crack depth A and surface directions, respectively.
Final number of loading cycles up to failure can be estimated by integration of both relations for fatigue crack growth rate. Fatigue life up to failure is calculated on a cycle-by-cycle basis for adequate crack length (i.e. the incremental crack growth is computed and added to the previous crack length, until the crack reaches a critical length) using following relations:

for the deepest point $\quad N = \int_0^N dN = \int_{a_i}^{a_c} \frac{1}{C_A \left(\Delta K_A \right)^{m_A}} \, da \tag{10}$

and the surface point $\quad N = \int_0^N dN = \int_{b_i}^{b_c} \frac{1}{C_B \left(\Delta K_B \right)^{m_B}} \, db \tag{11}$

where a_0, b_0 are the initial crack lengths for depth and surface directions. a_c, b_c present the critical lengths at failure for depth and surface directions and can be calculated using fracture toughness and applied load.

4. Numerical results

In this section, the formulated model for fatigue life estimation is examined on two structural components with semi-elliptical crack. The stress intensity factors were calculated using analytical and numerical approaches. Furthermore, authors have analyzed how adequately fatigue life up to failure of the pipe could be calculated when using relations for stress intensity factor used in the case of plate instead of equations for the pipe. The accuracy of the proposed model is validated with available experimental results.

4.1. Crack growth analysis for the pipe with a semi-elliptical crack

This example considers fatigue life estimation. The pipe made of carbon steel is with external semi-elliptical crack.. The material characteristics of carbon steel are: $E=2.05*10^5$ MPa, $S_y = 227$ MPa, $S_t = 406$ MPa, $m_A = m_B = 3.72$, $C_A = 3.2*10^{-13}$, $C_B = 2.15*10^{-13}$.

Geometry parameters of the pipe (Fig.1) are listed in Table 1. For all cases diameter is $R_0=51$ mm and the pipe is subjected to bending (Fig.2) with constant amplitude.

Crack growth analysis must start by determining the stress intensity factor for different values of crack length. Since semi-elliptical crack growth is considered, it is necessary to analyze depth direction and surface direction of crack growth. Based on known characteristics of geometry and loading, calculated values of the stress intensity factor for both directions are presented in Fig.3. For determination of the stress intensity factor range were used equations (1)-(8).
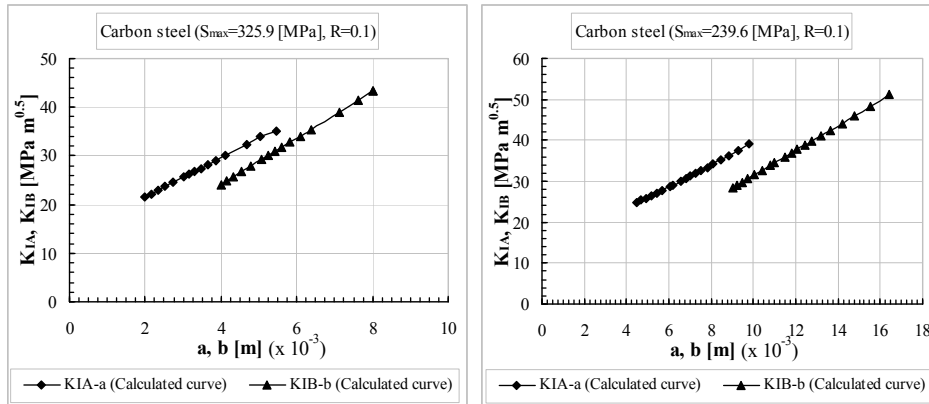

Figure 3. Stress intensity factor versus crack length
(a - Depth direction, b - Surface direction).

After the calculation of stress intensity factor for both directions and by applying fatigue parameters it is possible to estimate the fatigue life up to failure. Actually, by using equations for crack growth rate which were first integrated, the relations between depth crack length *a* as well as surface crack length *b* and the number of loading cycles up to failure (Eqs. (10),(11)) were formulated. Calculated results are shown in Fig.4 for both directions and two different levels of loading.
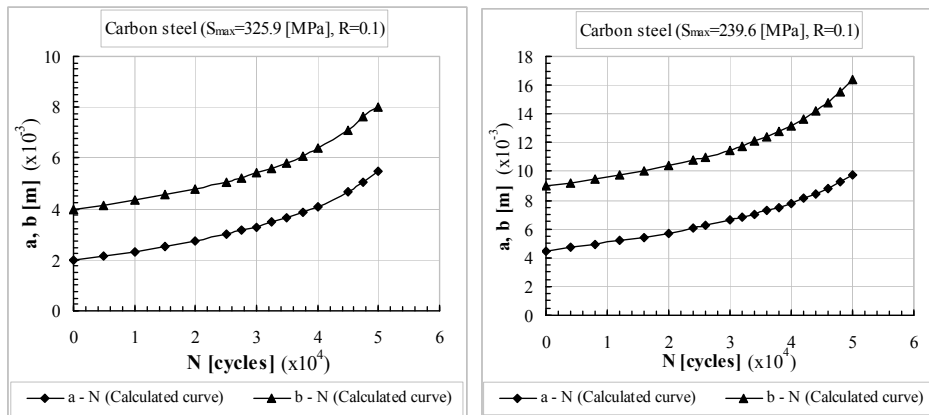

Figure 4. Crack length versus number of loading cycles for semi-elliptical crack
(a - Depth direction, b - Surface direction).

Moreover, estimated final number of loading cycles up to failure are compared with avaiable experimental data [11] in Table 1. The comparison shows that model formulated in this paper gives conservative solution than experimental results, so it is possible to use the presented model for fatigue life analysis of the pipe with external semi-elliptical crack

Table 1 Comparison of calculated number of loading cycles up to failure with experimental data for the pipe (R = 0.1).

No.	S_{max} [MPa]	a_0*10^{-3} [m]	b_0*10^{-3} [m]	$t*10^{-3}$ [m]	N_{final} [cycles] Experiment [11]	Calculated
1	325.9	2	4	8.5	52900	49046
2	325.9	3	6	8.5	21187	20000
3	239.6	4.5	9	12.7	88900	50000

4.2. Stress analysis for an aircraft nose landing gear with a semi-elliptical crack

In this example, stress intensity factor calculation of the aircraft nose landing gear with external semi-elliptical crack was carried out. For stress analysis analytical and numerical approaches are used. The main purpose/aspect, in this example, is to compare two different approaches for the calculation of stress intensity factor.

The aircraft nose landing gear made of steel is subjected to tensile loading with constant amplitude (S_{max} = 100 MPa and S_{max} = 273 MPa). Material characteristics are as follows: E= $2.10*10^5$ MPa, ν = 0.33, K_{IC} = 60 MPam$^{1/2}$ and geometry characteristics: R_0 = 32.75 mm, t = 3.5 mm, a_0= 1 mm with two different surface crack lengths: b_0 = 1 mm and b_0 = 2.5 mm (i.e. a/c = 1 and a/c = 0.4).

The present authors have computed the stress intensity factor by performing a finite element analysis as well as by using analytical approach (Eqs. (1) –(8)). The numerical calculation of the stress intensity factor is tackled by employing Q-P finite elements. For this purpose singular six-node finite elements [12] are applied. Based on the known geometry characteristics (Fig.1) and external loading, it is possible to model finite element meshes, step-by-step, for different crack increments by using super-elements around crack tip [13]. As a result of the finite element analysis, the stress intensity factors for both directions are defined for adequate crack growth increments up to the failure. A representation of the finite element analysis for the aircraft nose landing gear with semi-elliptical crack, made of steel is shown in Fig.5 and Fig.6.
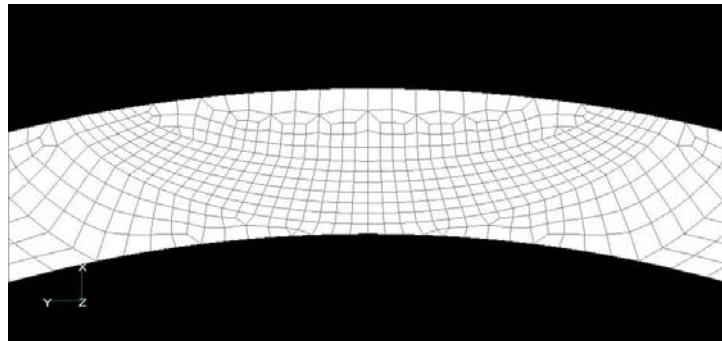
Figure 5. The part of finite element mesh of the aircraft nose landing gear with semi-elliptical crack.
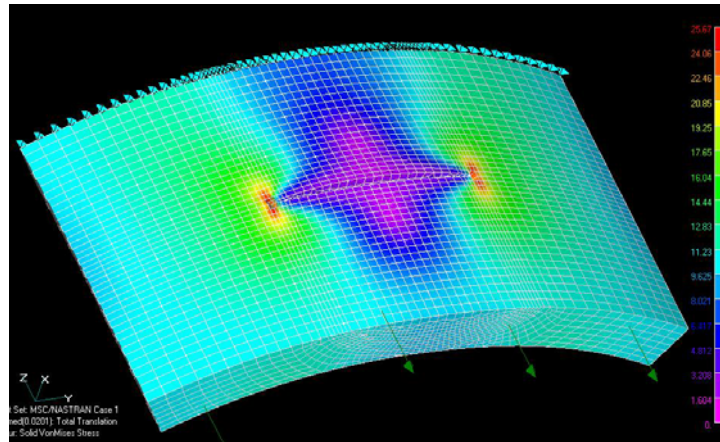

Figure 6. Stress distribution of the aircraft nose landing gear with semi-elliptical crack subjected to tensile load

Calculated results for stress intensity factor for both directions (surface and depth) are listed in Table 2 for different values of crack length as well as different levels of external loading by using proposed analytical method (Eqs. (1)-(8)) and a finite element method.

Table 2 Comparison of the computed stress intensity factors using analytical and numerical method
(*Positions: A - $\phi = 90^0$, B - $\phi = 0^0$*)

S_{max} [MPa]	$a*10^{-3}$ [m]	$b*10^{-3}$ [m]	a/b	K_{IA}^{FEM} [MPam$^{0.5}$]	$K_{IA}^{Anal.}$ [MPam$^{0.5}$]	K_{IB}^{FEM} [MPam$^{0.5}$]	$K_{IB}^{Anal.}$ [MPam$^{0.5}$]
100	2.75	7	0.4	12.73	12.16	10.91	15.99
100	2.75	2.75	1	6.73	6.58	9.03	8.67
273	2.75	2.75	1	18.85	17.74	20.43	23.65

From Table 3, it can be deduced that both approaches give almost the same evaluations for the stress intensity factors, so both numerical and analytical methods can be apply for stress analysis of the pipe with external semi-elliptical crack.

4. Conclusion

The computational model for fatigue life estimation up to failure is developed. The formulated model considers a pipe with external semi-elliptical crack. Analytical and numerical methods are applied for stress analysis i.e. the stress intensity factor calculations. Actually, due to the fact that as analytical relations for the stress intensity factors, expressions commonly used for finite plate are used, a comparison was performed of obtained calculations with results determined by applying finite element analysis for the pipe. Very good agreement was observed between the results for stress intensity factors by using two different approaches. Furthermore, fatigue life up to failure is estimated by

applying ″two-point plus semi-ellipse″ method. Comparison between the number of loading cycles up to failure point out the fact that estimations are in a good agreement with experimental results. Thus, formulated fatigue growth model is applicable in engineering practice for fatigue life estimation of the pipe with external semi-elliptical crack.

References

[1] Carpinteri A., Brighenti R., Spagnoli A. (1998) Part-through cracks in pipes under cyclic bending, *Nuclear Engineering and Design* 185, pp. 1-10.

[2] Carpinteri, A., Brighenti, R., Vantadori, S. (2006) Notched shells with surface cracks under complex loading. *Int J Mech Sciences*, Vol.48, pp.638-649.

[3] Boljanović S., Maksimović S., Posavljak S. (2011) Fatigue life estimation of cracked structural components In: Proceedings of International Conference DEMI 2011, Banja Luka, Republic of Srpska, May 26-28, pp.165-172.

[4] Ma C. C., Shen I. K. (1999) Calculation of stress intensity factors for elliptical cracks in finite bodies by using the boundary weight function method, *Journal Press. Ves. Technol. Trans. ASME*, 121(2), pp. 181-187.

[5] Ferahi M., Meguid S.A. (1998) Novel approach for evaluating weight functions for crack in finite bodies, *Engineering Fracture Mechanics*, 59(3), pp. 343-352.

[6] Smith, F.W., Sorensen, D.R. (1976) The semi-elliptical surface crack – A solution by the alternating method. *International Journal of Fracture*, vol. 12, no. 1, pp.47-57.

[7] Delale, F., Erdogan, F. (1981) Line-spring model for surface cracks in a reissner plate. *International Journal Engng. Sci.* vol.19. pp.1331-1340.

[8] Cruse, T.A. (1974) An improved boundary-integral equation method for three dimensional elastic stress analysis. *Computers and Structures*, vol. 4, pp.741-754.

[9] Raju I. S., Newman Jr. J. C. (1977) Improved stress-intensity factors for semi-elliptical surface cracks in finite-thickness plates. NASA TM X-72825.

[10] Raju I. S., Newman Jr. J. C. (1979) Stress-intensity factors for a wide range of semi-elliptical surface cracks in finite-thickness plates, *Engineering Fracture Mechanics*, 11(4), pp. 817-829.

[11] Ahn S.H., Ando K., Hidaka A. (1997) Fatigue crack growth and penentration behaviour in a pipe subjected to bending load. In: Proceedings of International Conference on Importance of Understanding the Fundamentals of the Fatigue Process in Counteracting its Effects in Engineering Components and Structures, Sheffield, March 17-21, pp.73-82.

[12] Sukumar N., Kumusa M. (1992) Application of the singular finite element to crack and sharp notches in orthotropic media. *International Journal of Fracture*, vol. 58, pp.177-192.

[13] Msc/NASTRAN, Theoretical Manuels.

APPLICATION OF FRACTURE MECHANICS PARAMETERS FOR WELDED JOINTS USABILITY TESTING

Ivica Čamagić[1], Nemanja Vasić[1], Zijah Burzić[2], Predrag Živković[1], Aleksandar Todić[1]

[1] Faculty of Technical Sciences,
The University of Priština, Kneza Miloša 7, 38220 Kosovska Mitrovica
e-mail: ivica.camagic@pr.ac.rs
[2] Military Institute of Techniques,
Katanićeva 15, 11030 Belgrade
e-mail: vti@vti.vs.rs

Abstract. Welded joint represents inhomogeneity by microstructure and mechanical properties, often by geometrical form, and by the stress field as well, which are affected by various factors as well as residual stresses after welding. Cracks of all kinds, problems of non-welded areas, presence of inclusions and similar, are problems of great significance for welded structures and at the same time problems considered in fracture mechanics. Full characterization of welded joints from exploitation properties angle, implies overview of their behaviour in presence of defects as well, or in other words, evaluation of their resistance towards crack initiation and propagation as the most dangers type of defect. Fracture mechanics deals with research of fracture phenomenon, crack propagation conditions and strength of material in final phase of deformation process. It represents scientific discipline in which connection of theoretical consideration with experimental results and occurrence of fracture and breakdowns in structure exploitation is inevitable. Problem of determination of fracture toughness K_{Ic} at a crack tip localized in a welded joint is placed in principle, because fracture mechanics assumes homogenous material, not only around crack tip but on a distance from it, in order to maintain valid theoretical assumptions and importance of a fracture toughness as a property measured by some of fracture mechanics methods.

Keywords: welded joints safety, defects, crack, fracture mechanics parameters, fracture toughness

1. Introduction

Fracture mechanics created new possibilities for structure safety insurance by theoretical and experimental analysis of the behaviour of a solid with a crack. Development of the standard for fracture toughness determination at plane strain, K_{Ic}, enabled application of linear-elastic fracture mechanics for real structures, made from high strength material. Validity condition for this testing is that only small plastic deformation zone is developed around a crack tip prior to crack development and fracture. According to Griffith energy criteria, crack in a certain solid propagates unstably if the crack propagation force (energy release rate) is higher than the material resistance to the crack propagation.

In linear-elastic fracture mechanics, the crack propagation force is identified by the stress intensity factor as:

$$K = Y\sigma\sqrt{\pi a} ,\tag{1}$$

where Y is dimensionless geometry factor, σ is remote stress and a is crack length.

Strength of materials to unstable crack propagation, within linear-elastic fracture mechanics, is presented by the critical value of stress intensity at plane strain state, K_{Ic}, or material property called fracture toughness. Fracture toughness determination procedure with homogenous materials at the plane strain state is precisely and in details established in the ASTM E399 [2] standard.

When values of fracture toughness and stress intensity factor are known, condition for the unstable crack propagation can be defined as:

$$K \geq K_{Ic}\tag{2}$$

Based on it, critical crack length a_c is determined, if fracture toughness, remote stress σ and geometry factor Y are known; or required fracture toughness (material selection) is determined if crack length a, remote stress σ and geometry factor Y are known. The unstable crack propagation condition, Eq. 2, can be used as a criterion for allowed loading determination (represented by stress σ), if crack length a, fracture toughness and geometry factor Y are known.

Direct determination of the fracture toughness, K_{Ic}, and its application is limited to the high strength materials only; because, with the most of structural materials, large zone of plastic deformation is developed around crack tip. Due to that, two additional parameters were introduced in the plastic behaviour analysis of material with crack, which is subject of elastic-plastic fracture mechanics:

- crack tip opening displacement *CTOD* (δ), and

- contour J integral, independent on the integration path.

In the linear-elastic area, when the plane strain conditions are satisfied, these two parameters represent critical values (δ_{Ic} and J_{Ic}) and they are directly connected with the K_{Ic} value. Convenience of *CTOD* and J parameters application is in possibility of their analysis even after development of significant plastic deformation, on one side, as well as their suitability for experimental determination according to the standards on the other side.

2. Testing of Welded Joint Fracture Mechanics

Generally accepted opinion that presence of cracks and other defects is possible, and even inevitable, is of particular importance for welded joints. Thence originates great interest to apply fracture mechanics parameters on welded joints and structures. However, two significant problems exist in the fracture mechanics parameters application for the welded joints behaviour analysis [3]:

- limited possibility for defects detection in terms of their size and position,

- heterogeneity of microstructure, shown in Fig. 1 [4] and mechanical properties of welded joints.
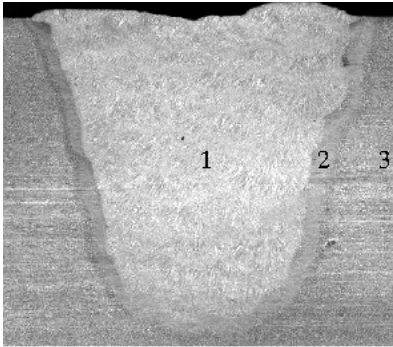

Figure 1. Macroscopic appearance of welded joint: 1-WM, 2-HAZ, 3-BM

Thus, welded joint safety estimation is not reliable enough, since where is not enough information on defects, and it is not certain how crack will develop through different parts of welded joint. Therefore, one of significant problems during testing of samples, with a crack, from welded joint is location of the crack tip [4, 5].

Considering different mechanical properties, it is clear that crack propagation conditions will differ, with a crack tip in different areas of welded joint. These difficulties are not obstacle to experimental determination of fracture toughness in critical zones of welded joint or the welded joint as whole, but difficulties appears during interpretation of measured values [5].

To get a complete image of the fracture mechanics testing application on welded joints it is necessary to describe specimens and indicate possible defects and deviations. Primarily, it is predicted to test fracture mechanics specimens by tension or bending. Among numerous shapes used in different researches, specimens for three point bending, shown Fig. 2, and compact specimens for tension, shown Fig. 3 [2, 6], are widely accepted. Specimens for three point bending (bending by force) proved to be appropriate in practice, and they are used in testing of all three listed fracture mechanics parameters (K_{Ic}, δ, J). Compact tension specimen enables significant material savings compared to different shapes of specimens, as well as relatively lower testing force.

Testing of specimens with a crack shows local behaviour of material around a crack tip of homogenous enough specimen material, so results of local behaviour can be treated globally, and they can be directly transferred to appropriate structure. Bearing in mind heterogeneous composition, shown in Fig. 1, such testing procedure is not reliable enough, since crack tip during fracture development can pass through the areas with different composition and mechanical properties of welded joint. That is why analysis of a welded joint is necessary from fracture mechanics application aspect.

Fig. 4, which shows low-alloyed, thermo-mechanically processed, high strength steel in multi-pass weld, illustrates complexity in terms of microstructure and geometry during determination of fracture toughness and other mechanical properties in the heat affected zone (HAZ). As a rule, places with lower fracture toughness (marked A and E in Fig. 4) appears in the narrow HAZ belt along the merge line due to repeated thermal cycles and plastic deformation [7].
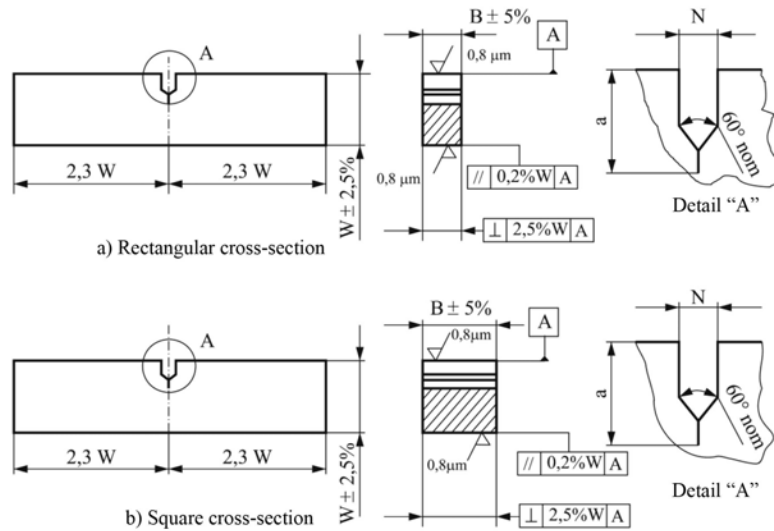

Figure 2. Specimen for three point bending

When it comes to the recommendation to use the lowest measured value during direct fracture toughness determination in the critical zone of joint, Fig. 4 illustrates numerous difficulties connected with such determination. When, like in case of steel, HAZ is critical area in which cracks typically occur, its size of 2-3 mm in the base metal, along the merging line, indicates experimental difficulties of setting starting fatigue crack tip on the critical place. Practical research experiences show that, even with the most caring handling, tens of samples must be tested in order to successfully locate crack tip in the narrow critical area and to reliably determine real minimal values of fracture toughness in HAZ, which in other words limits utilization degree to 10-20 % of tested samples [8].

Next difficulty in fracture toughness determination is the fatigue crack propagation trace, which has a tip located in HAZ (area A in Fig. 4), because it will penetrate HAZ areas with different microstructures and mechanical properties. Different properties in terms of crack propagation plane result in asymmetric forming of plastic zone in front of crack tip. Bearing in mind that real values of certain mechanical properties, i.e. yield strength, can not be directly determined for narrow brittle area A and E in HAZ, it is obvious that conditions for determination of fracture mechanics parameters values according to the procedures valid for homogenous materials are violated.

Because of the described constraints, different methods of fracture mechanics are not equally applicable for determination of the lowest value of fracture toughness in welded joint. If it is considered that the problem of fatigue crack tip placing on the critical position in HAZ is mutual for all methods, then criterion for applicability evaluation of certain methods could be its ability to measure fracture toughness directly in front of a crack tip, independent on material influence on larger distances from so called process zone at the crack tip. In this regard K_{Ic}, as the linear-elastic indicator of fracture toughness, is in advantage, since the limited plastic zone conditions for its determination are more severe than with the elastic-plastic indicators. In real situations, during welds testing, these severe conditions can rarely be satisfied, because it is usually steel with relatively high fracture toughness. Plastic zone size control by increment of a sample size is hardly attainable, first because the sample thickness would be multiple higher than the thickness of structure elements for softer steels, and due to additional complication of a crack tip positioning in the critical zone for samples cut out of welds with increased dimensions.
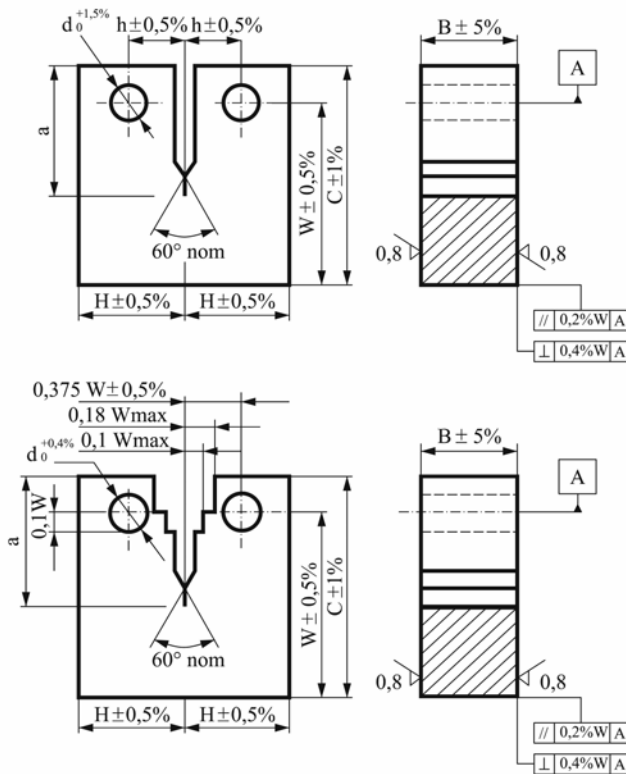

Figure 3. Compact tension specimen

As it was outlined above, heterogeneity of composition and mechanical properties of welded joints complicate the problem, primarily in terms of a fatigue crack tip position and properties of the areas through which fracture develops. But, if welded joint is treated as

structural set, then it is of interest to determine data for the weakest place when it comes to local testing, such as fracture mechanics parameters determination. Also it is clear that during tensile properties determination, especially tensile strength, information for welded joint as whole must be accepted as more authoritative for a welded structure than a single result for weld metal or for base metal.
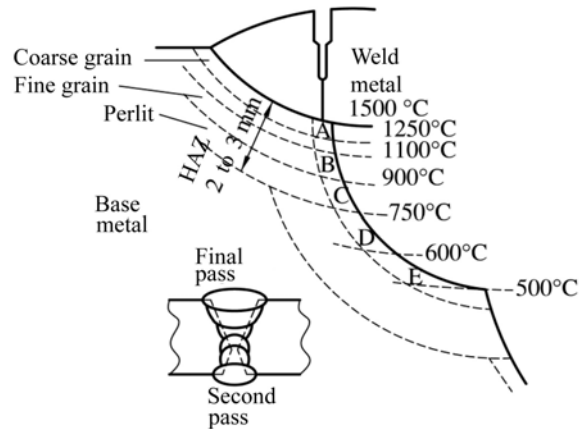

Figure 4. HAZ cross-section of high strength low alloyed steel weld

Large number of different weldability tests indicates that special attention was always given to crack problems in welded joints. Various defects can be discovered by nondestructive testing, but in many cases the decision is made to leave them. It means that welded joint can have defects and cracks that are not discovered and those that were discovered but were not removed. It can be easily concluded that in such case the evaluation of local behaviour of welded joint area near to the defect is at least as important as the evaluation of global joint behaviour. Although testing of V-notched specimens on the Scharpy pendulum provides precious data on local behaviour of a crack tip area. That data can not completely explain conditions of crack initiation and propagation.

Great interest for application of welded joints fracture mechanics testing has encountered the limitations in very beginning in terms of test cost and specimens number to be tested. Primarily, according to the already stated analysis at least 10 specimens must be tested in order to determine some of the welded joint fracture mechanics parameters. Such expensive testing will in many cases be economically justify if they contributes to structure safety or life increment, bearing in mind that more than half of the total steel production is embedded in welded structures [9]. It should be considered that fracture mechanics testing implies knowledge of mechanical properties. Reliable data on yield strength value, which is according to the standards for fracture mechanics parameters testing one of the basic comparative parameter of mechanical properties, is often missing for welded joints.

Despite all difficulties and uncertainty, application of fracture mechanics for welded joint testing is increasing. Reason is, primarily, in better and more complete understanding of behaviour of welded joint with a crack based on analysis of data obtained from those

testing. Standard BS 7448 [6, 10] predicts application of all three parameters (K_{Ic}, *CTOD*, *J* integral) for characterization of welded joint resistance to crack initiation and propagation, and prescribe cases in which every of them is competent.

In terms of position of notch and fatigue crack, standard goes further and defines different variants for X and K butt weld, as well as single pass weld. Requirements for crack position are:

- notch should be placed in such way that the fatigue crack plane is parallel to the longitudinal axis of the welded joint,

- crack tip should be in the tested area with greater length, to avoid local damages in small volume of material,

- notch is placed in the weld metal, on the merging line or in the heat affected zone.

For determination of convenience for additional material selection, weld metal (WM) is tested. Scheme for extraction of specimens with a notch and a fatigue crack in weld metal, is shown in Fig. 5.
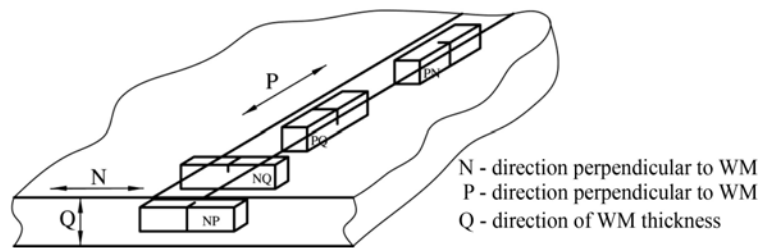

Figure 5. Specimen extraction method and crack position during weld metal testing

Specimens for fracture mechanics parameters determination are fabricated from associated tubes, the same way as real product. For plates with smaller thickness of 50 mm specimens in full thickness are used. Resistance to crack development in weld metal and heat affected zone is tested on specimens with a notch and a fatigue crack, which is schematically illustrated in Table 1 and Table 2 [9].
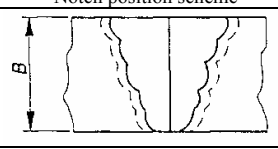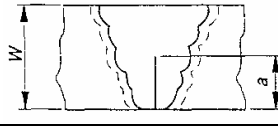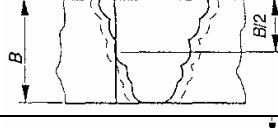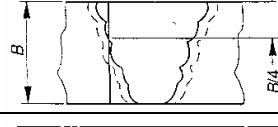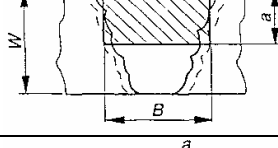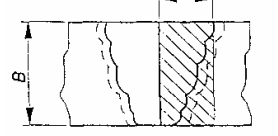
For the evaluation of collective influence of all areas in welded joint (WM, merging line and HAZ) and welding technological conditions, notch is placed to include narrow belt of all three areas, where tip slope is realized on the depth of 1,5-2,5 mm.

The heterogeneity of mechanical properties, expressed by K_{Ic} value, can be overviewed more clearly on the example of butt welded joint (2/3 X-weld) of high strength low alloyed steel Nionikral-70, welded with Tenacito-75 basic low-hydrogen electrode in diameters of 3,25 and 4 mm, supplied by Acroni Jesenice [10]. As requirements for plane strain state condition fulfilment:

$$B \geq 2,5 \cdot \left(\frac{K_{Ic}}{R_{p0,2}} \right)^2 ,$$ (3)

are not satisfied, instead of linear-elastic fracture mechanics defined by the ASTM E399 standard, elastic-plastic fracture mechanics according to the ASTM E 813 [11] were used. It allows determining the critical value of the stress intensity factor, K_{Ic}, by the critical J integral, J_{Ic}.

Table 1. Notch placement in fracture mechanics specimens for welded joint testing

Notch position scheme	Direction	Specimen geometry	Notch place
	NP	B x B or B x 2B	WM-along central line
	NQ	B x B	WM-from root along central line
	NP	B x B or B x 2B	HAZ-notch in the merging line on half of the thickness
	NP	B x B or B x 2B	HAZ- notch in the merging line on quarter of the thickness
	PQ	B x B	Transversally in WM
	PN	B x B	Transversally in WM along central line

The testing procedure consists of defining of R curve, or J-Δa curve, J integral dependency and crack increment Δa. Experiments were performed by single specimen testing method with successive partial unloading, or by compliance method, according to the ASTM E1152 standard [12]. The obtained F-(δ) and J- Δa diagrams for base metal (BM), weld metal and heat affected zone are shown in Fig. [10].
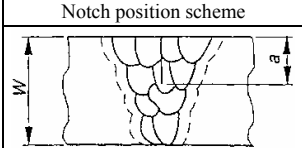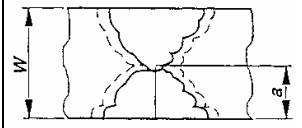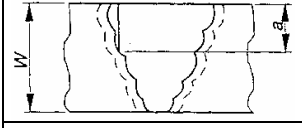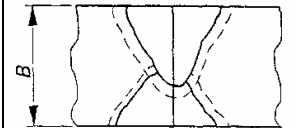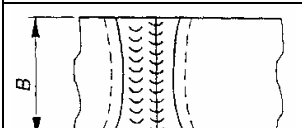
Diagram flow for these specimens match to large extent, except in the area of significant plastic deformation (part of the diagram from maximal force to the specimen fracture). However, clear differences are obtained when J_{Ic} value is determined by the regression line procedure.

From the critical J_{Ic} integral value, the critical stress intensity factor value or the fracture toughness at plane strain, K_{Ic}, can be calculated as:

$$K_{Ic} = \sqrt{\frac{J_{Ic} \cdot E}{1 - v^2}} .$$ (4)

J_{Ic} values determined from the diagrams and calculated values of the fracture toughness at plane strain, K_{Ic}, are given in Table 3 [10].

Table 2. Examples of notch position in specific parts of welded joint

Notch position scheme	Direction	Specimen geometry	Notch place
	NQ	B x B	Perpendicular to WM along the central line
	NQ	B x B	In the first weld of WM root
	NQ	B x B	Coarse grain composition of HAZ along WM
	NP	B x B or B x 2B	Through the largest volume of WM along the joint
	NP	B x B or B x 2B	Perpendicular to the largest volume of WM
	NP	B x B or B x 2B for specimens thicker than 50 mm	At least 15% of crack face in coarse grain HAZ composition

	NP	B x B or B x 2B	HAZ-5 mm from merging line

F-δ base metal

J-Δa base metal

F-δ weld metal

J-Δa weld metal

| F-δ heat affected zone | J-Δa heat affected zone |
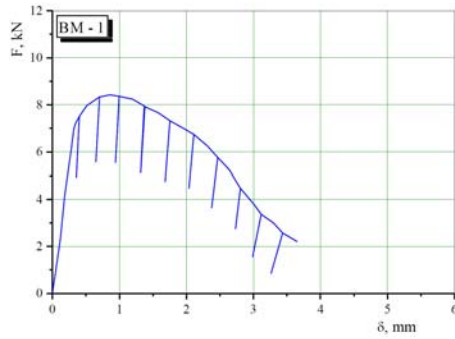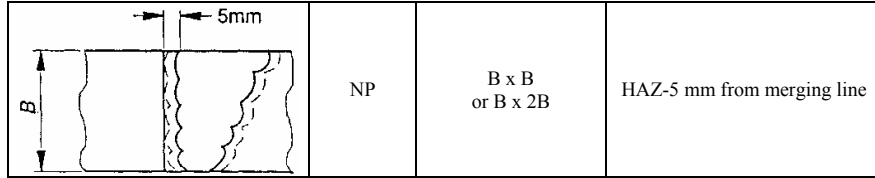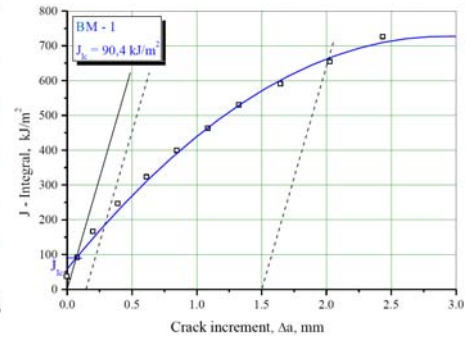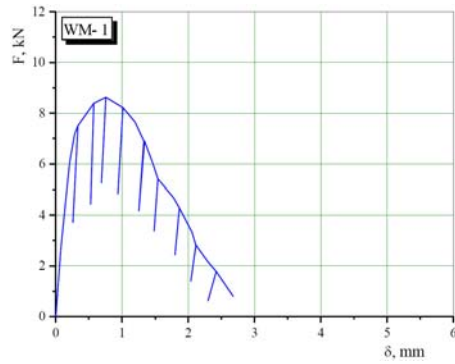
Figure 6. Diagrams of J integral determination by successive unload of a single specimen

The mechanical properties heterogeneity of welded joint or its components can clearly be seen from the obtained values of the fracture toughness at plane strain, K_{Ic}, determined indirectly by the critical J_{Ic} integral. Specimens with a notch in HAZ have the highest K_{Ic} value; however, in this particular case the differences are relatively small. These differences do not have to have more significant influence on structures submitted to static load in exploitation [10]. However, in case of structural elements submitted to constant variable load, changes of K_{Ic} are very significant because critical length of crack a_c directly depends on K_{Ic} value.

Table 3. Values of fracture mechanics parameters

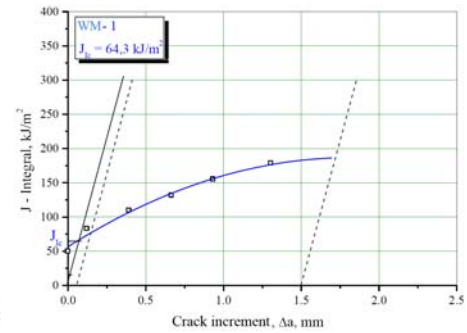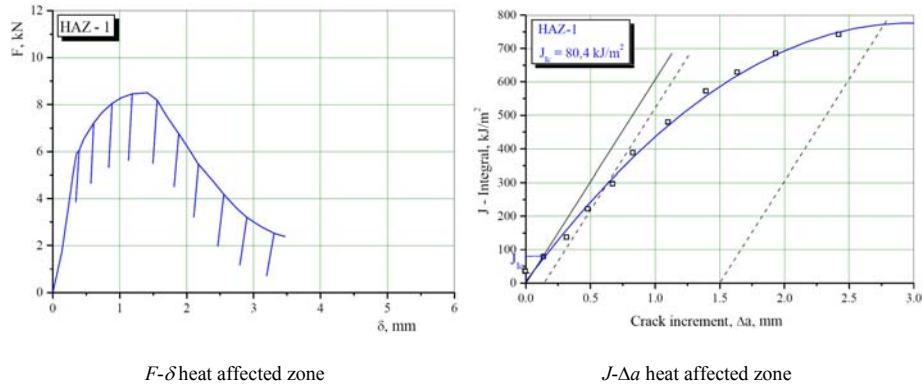| Specimen mark	Critical J-integral J_{Ic}, kJ/m^2	Critical stress intensity factor K_{Ic}, MPa m$^{1/2}$
BM-1	90,4	142,7
WM-1	64,3	119,2
HAZ-1	80,4	131,9

3. Conclusion

It is noticeable that structural and mechanical heterogeneity of the welded joint have significant influence on its resistance to crack development, both in the elastic and the plastic area. Therefore, during prescribing conditions for fracture mechanics testing, it is necessary to define not only the testing procedure and a fatigue crack placement, but the way of interpreting and the meaning of results as well.

It should be noted here that from structural aspect material properties can be estimated much better by individual values of K_{Ic} and $R_{p0,2}$ and their ratio (which is competent value in the standards ASTM E399 and BS 5447), than just by one of them. Using fracture mechanics basic expression:

$$K_{Ic} = \sigma \sqrt{\pi a_c} \, , \tag{5}$$

and setting values of conventional yield stress $R_{p0,2} = \sigma$, with presumption that the shape factor is equal to one, approximate values of the critical crack length a_c can be calculated.

It is obvious that permissible stress, that is lower than conventional yield stress, will give higher values of the critical crack length. That means that tested welded joint, or its components, in exploitation can have crack with length lower than specified without the danger of brittle fracture appearance. Due to that, and in order to ensure crack discovering before it reaches critical length, appropriate testing procedures without destruction should be applied. It is important to note that the calculated value of critical crack length a_c refers to the conditions of plane strain and structure with finite thickness, and that it must be corrected for every particular case in terms of the real thickness of structure material [10].

Fracture mechanics approached the problem of welded joints safety from the position of crack initiation control. In this case methodical and practical difficulties already appeared at initiation properties determination, due to the strict localization of dangerous place with critically low toughness. Once these difficulties are solved, in near or distant future, and reliable methods for rapid detection of that weakest place are strongly developed, conditions will be acquired to answer the key question, how much the existence of locally weak place is important for the safety of whole structure. Precise answer on the question formulated in such way, that earlier global approaches to brittle fraction was not up to, is rightfully expected from fracture mechanics. However, open problem will remain if the crack initiation approach will be sufficient for this purpose, or it will be necessary to go back again partly or completely to the position of crack restrain based on fracture mechanics.

References

[1] Gdoutos E E (2005) *Fracture Mechanics An Introduction*, Springer, Dordrecht.
[2] ASTM E399-89 (1986) Standard Test Method for Plane-Strain Fracture Toughness of Metallic Materials, *Annual Book of ASTM Standards*, **03.01**, pp. 522.
[3] Radović A (1984) Mogućnosti korišćenja kriterijuma mehanike loma u oceni sigurnosti zavarenih spojeva, *Letnja škola mehanike loma-Mehanika loma zavarenih spojeva*, Aranđelovac, pp. 15-43,.
[4] Sedmak A and Burzić Z (1999) *Izveštaj o kvalifikaciji tehnologije reparaturnog zavarivanja reaktora DC-301*, Mašinski fakultet, Beograd.
[5] Burzić Z and Sedmak S and Manjgo M (2001) Eksperimentalno određivanje parametara mehanike loma zavarenih spojeva, *Integritet i Vek Konstrukcija*, **2**, pp. 97.
[6] BS 7448 Part 1 (1991) *Fracture mechanics toughness tests-Method for determination of K_{Ic} critical CTOD and critical J values of metallic materials*, BSI.
[7] Sedmak S (1980-1981) *Istraživanje uticaja količine zavarivanjem unete toplote na promene u ZUT kompleksno legiranih čelika visoke čvrstoće*, TMF, Beograd.
[8] Brown W F and Srawley J E (1969) *Plane Strain Crack Toughness Testing of High Strength Metallic Materials*, Special Technical Publication STP 410, Philadelphia.
[9] BS 7448 Part 2 (1997) *Fracture mechanics toughness tests - Methods for determination of K_{Ic}, critical CTOD and critical J values of welds in metallic materials*, BBI.
[10] Čamagić I (2009) *Analiza napona i deformacija zavarenih spojeva niskolegiranih čelika povišene čvrstoće u prisustvu prslina*, magistarski rad, Fakultet tehničkih nauka, Kosovska Mitrovica.
[11] ASTM E813-89, Standard Test Method for J_{Ic}, A Measure of Fracture Toughness*, Annual Book of ASTM Standards*, **03.01**, pp. 651.
[12] ASTM E1152-91, Standard Test Method for Determining J-R Curve, *Annual Book of ASTM Standards*, **03.01**, pp. 724.

GEOMETRICALLY NONLINEAR ANALYSIS
OF LAMINATED COMPOSITE PLATES

M. Ćetković[1], Dj. Vuksanović[2]

[1] Faculty of Civil Engineering
The University of Belgrade, Bul. Kralja Aleksandra 73, 11000 Belgrade
e-mail: cetkovicm@grf.bg.ac.rs
[2] Faculty of Civil Engineering,
The University of Belgrade, Bul. Kralja Aleksandra 73, 11000 Belgrade
e-mail: george@grf.bg.ac.rs

Abstract. The low mass density and the high tensile strength, usually expressed through the specific modulus of elasticity and the specific strength, have made composite materials lighter and stronger compared with most traditional materials (such as steel, concrete, wood, etc.) and have increased their application not only for secondary, but during the last two decades also for primarily structural members in aerospace and automotive industry, ship building industry and bridge design. Although weight saving has eliminated constrain of slenderness and thickness and has made possible use of very thin plate elements, they have become susceptible to large deflections. In such cases, the geometry of structures is continually changing during the deformation and geometrically nonlinear analysis should be adopted. In this paper the geometrically nonlinear laminated plate finite element model is obtained using the principle of virtual displacement. With the layerwise displacement field of Reddy [1], nonlinear Green-Lagrange small strain large displacements relations (in the von Karman sense) and linear elastic orthotropic material properties for each lamina, the 3D elasticity equations are reduced to 2D problem and the nonlinear equilibrium integral form is obtained. The obtained displacement dependent secant stiffness matrix is utilized in Direct interation procedure for the numerical solution of nonlinear finite element equilibrium equations. The originally coded MATLAB computer program for the finite element solution is used to verify the accuracy of the numerical model, by calculating nonlinear response of plates with different mechanical properties, which are isotropic, orthotropic and anisotropic (cross ply and angle ply), different plate thickness, different boundary conditions and different load direction (unloading/loading). The obtained results are compared with available results from the literature and the linear solutions from the previous paper [2].

.

1. Introduction

The low mass density (ρ) and the high tensile strength (σ_u), usually expressed through the specific modulus of elasticity (E/ρ) and the specific strength (σ_u/ρ) have made composite materials lighter and stronger compared with most traditional materials (such as steel, concrete, wood, etc.) and have increased their application not only for secondary, but during the last two decades also for primarily structural members in aerospace and automotive industry, ship building industry and bridge design. The advanced

mechanical properties of composite materials, which are resulted in large weight savings, have given designers more flexibility in finding efficient solution for specific problem, but have also required formulation of mathematical model able to present their complex anisotropic nature. Although weight saving has eliminated constrain of slenderness and thickness and has made possible use of very thin plate elements, they have become susceptible to large deflections [4,5]. In such cases, the geometry of structures is continually changing during the deformation and geometrically nonlinear analysis should be adopted. The geometrically nonlinear analysis seems also to be necessary for obtaining the structural response of unsymmetrical laminated composite materials [6]. Namely, the nonlinear response of these laminates is present even for small displacements, due to complex coupling between in-plane and out-of plane deformation.

A considerable amount of research work has been carried out so far on the nonlinear analysis of laminated plates. Among the published works, the von Karman plate theory of plates undergoing large deflections has attracted outstanding attention and a number of papers have been published. The first authors investigating the nonlinear response using the von Karman nonlinear theory [7, 8] were: Leissa, Bennett, Bert, Chandra and Raju, Zaghloul and Kennedy, Chia and Prabhakara, Noor and Hartley, and in the last decades Han, Tabiei and Park, Singh, Lal and Kumar, Reddy and Chao, Zhang Kim and others.

Mechanical response of laminated composite material is generally 3D problem of nonlinear mechanics. However, due to its mathematical complexity, analytical solutions using 3D theory of elasticity are usually difficult and some times even impossible to achieve, while numerical solutions are computationally inefficient and constrained to very specific domains. Thus, whenever possible, refined simplified mathematical models, with acceptable accuracy in a field of applications, should be used. It is shown that the Equivalent Single Layer theories (ESL) may give acceptable results when analyzing global response, such as gross deflections and gross stresses, critical buckling loads and fundamental frequencies of thin to moderate thick laminated composite plates [9]. However, a continuous displacement function in ESL is not able to accurately present the discontinuous zigzag variation of displacements in highly anisotropic plates and give adequate stress distribution at local or ply level [2]. A compromise between 3D theory of elasticity and ESL theories is then achieved with the use of Layer Wise theories (LW). In LW theories the in-plane displacement field, assumed for each layer, is interpolated through the thickness by appropriate layerwise Lagrange interpolation function or Heaviside step function [3], thus replacing 3D laminated element with N+1 2D plate elements (N is number of layers), which fulfills the continuity of displacement functions at the interfaces between adjacent layers.

From the continuum mechanics it is known that two different level of geometrical nonlinearity may be modeled, which are: geometrically nonlinear models with small strain and large displacements (von Karman theory) and geometrically nonlinear models with large strains. In the first case, the geometry of the structure before deformation remains unchanged after the deformation. However, the structure is subjected to large displacements and the equilibrium is achieved on the configuration displaced from the undeformed one. In the second case the geometry of the structure is changing during the deformation and the equilibrium is achieved on the deformed configuration. In both cases equilibrium equations are nonlinear.

In order to formulate nonlinear finite element model of laminated structures, which will be able to represent two above mentioned levels of geometrical nonlinearity,

two distinct approaches have been reported in the literature [3]. The first approach is based on laminate theory, in which 3D elasticity equations are reduced to 2D equations through certain kinematical assumptions and homogenization through the thickness. In this approach only first type of nonlinearity or small strain, large displacement assumption may be included. The finite elements based on such an assumptions are named the laminated elements. The second approach is based on 3D continuum formulation (total and updated Lagrange formulation) and both types on nonlinearity may be included. Finite elements based on this approach are called the continuum elements.

The aim of the author's research on composite materials so far was to implement Layerwise theory of Reddy or Generalized Layerwise Plate Theory-GLPT [1] on different levels of analysis of laminated composite plates. The previous work has been concerned with the linear analysis [2], and the linear laminated plate element of GLPT has been formulated, while in the present paper the GLPT nonlinear laminated plate element with von Karman geometrical nonlinearity is presented.

In this paper the mathematical and numerical model for geometrically nonlinear, small strain, large displacements problem of laminated composite plates is presented. The 3D elasticity equations are reduced to 2D problem using kinematical assumptions based on layerwise displacement field of Reddy (GLPT). With the assumed displacement field, nonlinear Green-Lagrange small strain large displacements relations and linear orthotropic material properties for each lamina, the principle of virtual displacement (PVD) is used to derive the weak form of the problem. The weak form or nonlinear integral equilibrium equations are discretized using isoparametric finite element approximation. The obtained nonlinear incremental algebric equilibrium equations are solved using direct iteration procedure. The originally coded MATLAB computer program for the finite element solution is used to investigate the effects of geometrical nonlinearity on displacement and stress field of thin and thick, isotropic, orthotropic and anisotropic laminated composite plates with various boundary conditions and loading direction (loading/unloading). The accuracy of the numerical model is verified by being compared with available results from the literature and the linear solutions from the previous paper [2]. The appropriate conclusions are derived.

2. Theoretical formulation

2.1 Displacement field

In the LW theory of Reddy [1] or Generalized Layerwise Plate Theory (GLPT), in-plane displacements components (u, v) are interpolated through the thickness using 1D linear Lagrangian interpolation function $\Phi^I(z)$, while transverse displacement component w is assumed to be constant through the plate thickness.

$$
\begin{aligned}
u_1(x,y,z) &= u(x,y) + \sum_{I=1}^{N+1} U^I(x,y) \cdot \Phi^I(z) \\
u_2(x,y,z) &= v(x,y) + \sum_{I=1}^{N+1} V^I(x,y) \cdot \Phi^I(z), \\
u_3(x,y,z) &= w(x,y)
\end{aligned}
\tag{1}
$$

2.2 Strain-displacement relations

The Green Lagrange strain tensor associated with the displacement field Eq.(1) can be computed using von Karman strain-displacement relation to include geometric nonlinearities as follows:

$$\varepsilon_{xx} = \frac{\partial u_1}{\partial x} + \frac{1}{2}\left(\frac{\partial u_3}{\partial x}\right)^2 = \frac{\partial u}{\partial x} + \sum_{I=1}^{N+1}\frac{\partial U^I}{\partial x}\Phi^I + \frac{1}{2}\left(\frac{\partial w}{\partial x}\right)^2,$$

$$\varepsilon_{yy} = \frac{\partial u_2}{\partial y} + \frac{1}{2}\left(\frac{\partial u_3}{\partial y}\right)^2 = \frac{\partial v}{\partial y} + \sum_{I=1}^{N+1}\frac{\partial V^I}{\partial y}\Phi^I + \frac{1}{2}\left(\frac{\partial w}{\partial y}\right)^2,$$

$$\gamma_{xy} = \frac{\partial u_1}{\partial y} + \frac{\partial u_2}{\partial x} + \frac{\partial u_3}{\partial x}\frac{\partial u_3}{\partial y} = \frac{\partial u}{\partial y} + \frac{\partial v}{\partial x} + \sum_{I=1}^{N+1}\left(\frac{\partial U^I}{\partial y} + \frac{\partial V^I}{\partial x}\right)\Phi^I + \frac{\partial w}{\partial x}\frac{\partial w}{\partial y}, \qquad (2)$$

$$\gamma_{xz} = \frac{\partial u_1}{\partial z} + \frac{\partial u_3}{\partial x} = \sum_{I=1}^{N+1}U^I\frac{d\Phi^I}{dz} + \frac{\partial w}{\partial x},$$

$$\gamma_{yz} = \frac{\partial u_2}{\partial z} + \frac{\partial u_3}{\partial y} = \sum_{I=1}^{N+1}V^I\frac{d\Phi^I}{dz} + \frac{\partial w}{\partial y}.$$

2.3 Constitutive equations

For Hook's elastic material, the stress-strain relations for k-th orthotropic lamina have the following form:

$$\begin{Bmatrix}\sigma_{xx}\\\sigma_{yy}\\\tau_{xy}\\\tau_{xz}\\\tau_{yz}\end{Bmatrix}^{(k)} = \begin{bmatrix}Q_{11} & Q_{12} & Q_{13} & 0 & 0\\Q_{12} & Q_{22} & Q_{23} & 0 & 0\\Q_{13} & Q_{23} & Q_{33} & 0 & 0\\0 & 0 & 0 & Q_{44} & Q_{45}\\0 & 0 & 0 & Q_{45} & Q_{55}\end{bmatrix}^{(k)} \times \begin{Bmatrix}\varepsilon_{xx}\\\varepsilon_{yy}\\\gamma_{xy}\\\gamma_{xz}\\\gamma_{yz}\end{Bmatrix}^{(k)}. \qquad (3)$$

Where:

$\boldsymbol{\sigma}^{(k)} = \{\sigma_{xx}\quad \sigma_{yy}\quad \tau_{xy}\quad \tau_{xz}\quad \tau_{yz}\}^{(k)T}$ and $\boldsymbol{\varepsilon}^{(k)} = \{\varepsilon_{xx}\quad \varepsilon_{yy}\quad \gamma_{xy}\quad \gamma_{xz}\quad \gamma_{yz}\}^{(k)T}$ are stress and strain components respectively, and $\mathbf{Q}_{ij}^{(k)}$ are transformed elastic coefficients, of k-th lamina in global coordinates.

2.4 Equilibrium equations

Equilibrium equations may be obtained from the Principle of Virtual Displacements (PVD), in which sum of external virtual work done on the body and internal virtual work stored in the body should be equal zero:

$$0 = \int_{\Omega} \left[\left(\{\delta\varepsilon^0\}^T + \{\delta\varepsilon^m\}^T \right) \{N^0\} + \{\delta\varepsilon^I\}^T \{N^I\} + \delta u\, q_x^0 + \delta v\, q_y^0 + \delta w\, q_z^0 \right] dxdy$$
$$- \oint_{\Gamma} \delta u_n\, N_{nn}\, ds - \oint_{\Gamma} \delta u_s\, N_{ns}\, ds - \oint_{\Gamma} \delta w\, (Q_n + P_n)\, ds - \oint_{\Gamma} \delta U_n^I\, N_{nn}^I\, ds - \oint_{\Gamma} \delta U_s^I\, N_{ns}^I\, ds \qquad (4)$$

where $\left\{ q_x^0, q_y^0, q_z^0 \right\}$ is distributed load in x, y, z directons, while internal forces are:

$$\left\{ \begin{matrix} \{N^0\} \\ \{N^I\} \end{matrix} \right\} = \begin{bmatrix} [A] & [B^I] \\ [B^I] & \sum_{J=1}^{N} [D^{JI}] \end{bmatrix} \left\{ \begin{matrix} \{\varepsilon^0\} + \{\varepsilon^m\} \\ \{\varepsilon^I\} \end{matrix} \right\} \qquad (5)$$

Where A, B, B^I, D^{JI} matrices are given in [12], while internal force vectors are:

$$\{N^0\} = \left\{ N_{xx} \quad N_{yy} \quad N_{xy} \quad Q_x \quad Q_y \right\}^T, \qquad \{N^I\} = \left\{ N_{xx}^I \quad N_{yy}^I \quad N_{xy}^I \quad Q_x^I \quad Q_y^I \right\}^T$$

$$N_{nn} = N_{xx}n_x + N_{xy}n_y, \quad N_{ns} = N_{xy}n_x + N_{yy}n_y, \quad Q_n = Q_x n_x + Q_y n_y,$$

$$P_n = \left(N_{xx}\frac{\partial w}{\partial x} + N_{xy}\frac{\partial w}{\partial y} \right)n_x + \left(N_{xy}\frac{\partial w}{\partial x} + N_{yy}\frac{\partial w}{\partial y} \right)n_y,$$

$$N_{nn}^I = N_{xx}^I n_x + N_{xy}^I n_y, \quad N_{ns}^I = N_{xy}^I n_x + N_{yy}^I n_y.$$

and strain vectors are:

$$\{\varepsilon^0\} = \left\{ \frac{\partial u}{\partial x} \quad \frac{\partial v}{\partial y} \quad \frac{\partial u}{\partial y} + \frac{\partial v}{\partial x} \quad \frac{\partial w}{\partial x} \quad \frac{\partial w}{\partial y} \right\}^T,$$

$$\{\varepsilon^m\} = \left\{ \frac{1}{2}\left(\frac{\partial w}{\partial x}\right)^2 \quad \frac{1}{2}\left(\frac{\partial w}{\partial y}\right)^2 \quad \frac{\partial w}{\partial x}\frac{\partial w}{\partial x} \quad 0 \quad 0 \right\}^T,$$

$$\{\varepsilon^I\} = \left\{ \frac{\partial U^I}{\partial x} \quad \frac{\partial V^I}{\partial y} \quad \frac{\partial U^I}{\partial y} + \frac{\partial V^I}{\partial x} \quad U^I \quad V^I \right\}^T.$$
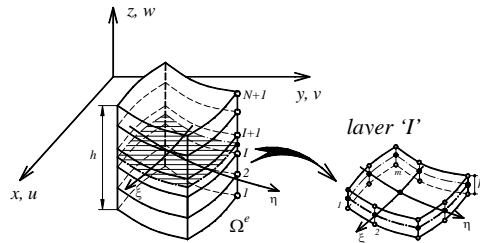
3. Finite Element Model

Figure 1. Plate finite element with n layers and m nodes

415

The GLPT finite element consists of middle surface plane and I=1, N+1 planes through the plate thickness Figure 1. The element requires only the C^0 continuity of major unknowns, thus in each node only displacement components are adopted, that are (u, v, w) in the middle surface element nodes and (U^I, V^I) in the I-th plane element nodes. The generalized displacements over element Ω^e can be expressed as:

$$
\left\{ \begin{matrix} u \\ v \\ w \end{matrix} \right\}^e = \left\{ \begin{matrix} \sum_{j=1}^{m} u_j \Psi_j \\ \sum_{j=1}^{m} v_j \Psi_j \\ \sum_{j=1}^{m} w_j \Psi_j \end{matrix} \right\}^e = \sum_{j=1}^{m} [\mathbf{\Psi}_j]^e \{\mathbf{d}_j\}^e \quad \left\{ \begin{matrix} U^I \\ V^I \end{matrix} \right\}^e = \left\{ \begin{matrix} \sum_{j=1}^{m} U_j^I \Psi_j \\ \sum_{j=1}^{m} V_j^I \Psi_j \end{matrix} \right\}^e = \sum_{j=1}^{m} [\overline{\mathbf{\Psi}}_j]^e \{\mathbf{d}_j^I\}^e
$$

(6)

where $\{\mathbf{d}_j\}^e = \left\{ u_j^e \quad v_j^e \quad w_j^e \right\}^T, \{\mathbf{d}_j^I\}^e = \left\{ U_j^I \quad V_j^I \right\}^T$ are displacement vectors, in the middle plane and I-th plane, respectively, Ψ_j^e are interpolation functions, while $[\mathbf{\Psi}_j]^e, [\overline{\mathbf{\Psi}}_j]^e$ are interpolation function matrix for the j-th node of the element Ω^e, given in [2].

Substituting element displacement field Eq.(6) in to weak form Eq.(4), the nonlinear laminated finite element is obtained:

$$
[\mathbf{K}_{NL}]^e \cdot \{\mathbf{d}\}^e = \{\mathbf{f}\}^e
$$

(7)

where secant stiffness matrix is:

$$
[\mathbf{K}_{NL}]^e = \begin{bmatrix} [\mathbf{K}^{11}]^e & [\mathbf{K}^{12}]^e \\ [\mathbf{K}^{12}]^e & [\mathbf{K}^{22}]^e \end{bmatrix}
$$

$$
[\mathbf{K}^{11}]^e = \sum_{i=1}^{m} \sum_{j=1}^{n} \int_{\Omega^e} [\mathbf{H}_i^e]^T \cdot [\mathbf{A}] \cdot [\mathbf{H}_j^e] + \underline{[\mathbf{H}_i^e]^T \cdot [\mathbf{A}] \cdot [\mathbf{H}_{j\,NL}^e]} + \underline{2[\mathbf{H}_{i\,NL}^e]^T \cdot [\mathbf{A}] \cdot [\mathbf{H}_j^e]} + \underline{2[\mathbf{H}_{i\,NL}^e]^T \cdot [\mathbf{A}] \cdot [\mathbf{H}_{j\,NL}^e]} \; d\Omega^e
$$

$$
[\mathbf{K}^{12}]^e = \sum_{i=1}^{m} \sum_{j=1}^{n} \int_{\Omega^e} \left([\mathbf{H}_i^e]^T \cdot [\mathbf{B}^I] \cdot [\overline{\mathbf{H}}_j^e] + \underline{2[\mathbf{H}_{i\,NL}^e]^T \cdot [\mathbf{B}^I] \cdot [\overline{\mathbf{H}}_j^e]} \right) d\Omega^e
$$

$$
[\mathbf{K}^{21}]^e = \sum_{i=1}^{m} \sum_{j=1}^{n} \int_{\Omega^e} \left([\overline{\mathbf{H}}_i^e]^T \cdot [\mathbf{B}^I] \cdot [\mathbf{H}_j^e] + \underline{[\overline{\mathbf{H}}_i^e]^T \cdot [\mathbf{B}^I] \cdot [\mathbf{H}_{j\,NL}^e]} \right) d\Omega^e
$$

$$
[\mathbf{K}^{22}]^e = \sum_{i=1}^{m} \sum_{j=1}^{n} \int_{\Omega^e} [\overline{\mathbf{H}}_i^e]^T \cdot [\mathbf{D}^{IJ}] \cdot [\overline{\mathbf{H}}_j^e] \; d\Omega^e
$$

(8)

and external force vectors $\left\{\mathbf{f}\right\}^e = \left\{\begin{array}{c} \left\{\mathbf{f^0}\right\}^e \\ \left\{\mathbf{f^I}\right\}^e \end{array}\right\}$ are:

$$\left\{\mathbf{f^0}\right\}^e = \sum_{i=1}^m \left[\int_{\Omega^e} \left[\mathbf{\Psi_i^e}\right]^T \left\{\begin{array}{c} q_x^0 \\ q_y^0 \\ q_z^0 \end{array}\right\} d\Omega^e + \oint_{\Gamma^e} \left[\mathbf{\Psi_i^e}\right]^T \left\{\begin{array}{c} N_{nn} \\ N_{ns} \\ Q_n + P_n \end{array}\right\} d\Gamma^e \right]$$

$$\left\{\mathbf{f^I}\right\}^e = \sum_{i=1}^m \left[\int_{\Omega^e} \left[\overline{\mathbf{\Psi}}_i^e\right]^T \cdot \left\{\begin{array}{c} q_x^I \\ q_y^I \end{array}\right\} d\Omega^e + \oint_{\Gamma^e} \left[\overline{\mathbf{\Psi}}_i^e\right]^T \cdot \left\{\begin{array}{c} N_{nn}^I \\ N_{ns}^I \end{array}\right\} d\Gamma^e \right]$$

(9)

while:

$$\left[\mathbf{H}_j^e\right]_j = \begin{bmatrix} \dfrac{\partial \Psi_j^e}{\partial x} & 0 & 0 \\ 0 & \dfrac{\partial \Psi_j^e}{\partial y} & 0 \\ \dfrac{\partial \Psi_j^e}{\partial y} & \dfrac{\partial \Psi_j^e}{\partial x} & 0 \\ 0 & 0 & \dfrac{\partial \Psi_j^e}{\partial x} \\ 0 & 0 & \dfrac{\partial \Psi_j^e}{\partial y} \end{bmatrix}, \quad \left[\mathbf{H}_{j\,NL}^e\right] = \frac{1}{2} \begin{bmatrix} 0 & 0 & \dfrac{\partial w}{\partial x}\dfrac{\partial \Psi_j^e}{\partial x} \\ 0 & 0 & \dfrac{\partial w}{\partial y}\dfrac{\partial \Psi_j^e}{\partial y} \\ 0 & 0 & \dfrac{\partial w}{\partial x}\dfrac{\partial \Psi_j^e}{\partial y} + \dfrac{\partial w}{\partial y}\dfrac{\partial \Psi_j^e}{\partial x} \\ 0 & 0 & 0 \\ 0 & 0 & 0 \end{bmatrix},$$

$$\left[\overline{\mathbf{H}}_j^e\right]_j = \begin{bmatrix} \dfrac{\partial \Psi_j^e}{\partial x} & 0 \\ 0 & \dfrac{\partial \Psi_j^e}{\partial y} \\ \dfrac{\partial \Psi_j^e}{\partial y} & \dfrac{\partial \Psi_j^e}{\partial x} \\ 1 & 0 \\ 0 & 1 \end{bmatrix}.$$

(10)

With the known displacement field, the stress field over the element may be obtained as a part of a postprocessor, using strain displacement and constitutive relations, Eqs. (2), (3) as:

$$\left\{\mathbf{\sigma}_b\right\}_U^{(\kappa)\,e} = \left[\mathbf{Q}_b\right]^{(k)} \sum_{j=1}^m \left(\left[\mathbf{H}_{bj}\right] + \left[\mathbf{H}_{bj}^{NL}\right] \right) \left\{\mathbf{d}_j\right\}^e + \left[\mathbf{Q}_b\right]^{(k)} \sum_{j=1}^m \left[\overline{\mathbf{H}}_{b_j}\right] \left\{\mathbf{d}_j^I\right\}^e$$

$$\{\sigma_b\}_O^{(\kappa)\,e} = [Q_b]^{(k)} \sum_{j=1}^{m} \left([H_{bj}] + [H_{bj}^{NL}] \right) \{d_j\}^e + [Q_b]^{(k)} \sum_{j=1}^{m} [\overline{H}_{bj}] \{d_j^{I+1}\}^e$$

$$\{\sigma_s\}_{const}^{(k)\,\,e} = [Q_s]^{(k)} \sum_{j=1}^{m} [H_{sj}] \{d_j\}^e + [Q_s]^{(k)} \sum_{j=1}^{m} [\overline{H}_{sj}] \left(\{d_j^{I+1}\}^e - \{d_j^{I}\}^e \right) / h_k \qquad (11)_{1,2,,3}$$

where $\{\sigma_b\}_U^{(\kappa)\,e}$ and $\{\sigma_b\}_O^{(\kappa)\,e}$ are in-plane normal stresses $\left(\sigma_{xx}, \sigma_{yy}, \tau_{xy} \right)$ at bottom and upper plane in k-th layer of plate element 'e', while $\{\sigma_s\}_{const}^{(k)\,\,e}$ are average transverse shear stresses $\left(\tau_{xz}, \tau_{yz} \right)$ in k-the layer of plate element.

4. Numerical results and discussion

Based on the previously derived laminated finite element model for the geometrically nonlinear analysis of laminated composite plates, the original computer program is coded using MATLAB programming language. The nonlinear finite element secant stiffness matrix is evaluated using Gauss–Legendre quadrature rule, which are 3x3 Gauss integration schemes or 2D quadratic Lagrange rectangular element for in-plane interpolation and 1D linear Lagrange element for through the thickness interpolation. The Direct iteration numerical method is used to solve nonlinear incremental equilibrium equations. The effects of plate thickness, lamination scheme, boundary conditions and load direction on nonlinear response of isotropic, orthotropic and anisotropic plates are analyzed. The accuracy of the present formulation is demonstrated through a number of examples and by comparison with results available from the literature.
The following boundary conditions at the plate edges are analyzed [10].
Simply supported (SS):

$$\textbf{SS:} \quad \begin{cases} x = 0, a: & v_0 = w_0 = V^I = N_{xx} = N_{xx}^I = 0 \\ y = 0, b: & u_0 = w_0 = U^I = N_{yy} = N_{yy}^I = 0 \end{cases} \quad I = 1,\ldots N+1 \qquad (12)$$

Simply supported-hinged (HH):

$$\textbf{HH:} \quad \begin{cases} x = 0, a: & u_0 = v_0 = w_0 = V^I = N_{xx}^I = 0 \\ y = 0, b: & u_0 = v_0 = w_0 = U^I = N_{yy}^I = 0 \end{cases} \quad I = 1,\ldots N+1 \qquad (13)$$

Clamped (CC):

$$\textbf{CC:} \quad \begin{cases} x = 0, a: & u_0 = v_0 = w_0 = U^I = V^I = 0 \\ y = 0, b: & u_0 = v_0 = w_0 = U^I = V^I = 0 \end{cases} \quad I = 1,\ldots N+1 \qquad (14)$$

When analyzing a quarter of a plate, boundary conditions in the plane of symmetry become:
For cross ply laminates:

$$\textbf{SS1:} \quad \begin{cases} x = a/2: & u_0 = U^I = N_{yy} = N_{yy}^I = 0 \\ y = b/2: & v_0 = V^I = N_{xx} = N_{xx}^I = 0 \end{cases} \quad I = 1,\ldots N+1 \qquad (15)$$

For angle ply laminates:

SS2: $\begin{cases} x = a/2: & v_0 = U^I = N_{xx} = N^I_{yy} = 0 \\ y = b/2: & u_0 = V^I = N_{yy} = N^I_{xx} = 0 \end{cases}$ $I = 1, \ldots N+1$ (16)

Example 4.1. A nonlinear bending of square, simply supported (SS1), isotropic plate, with $a = b = 10\,\text{in}$ and $h = 1\,\text{in}$ made of material:

$$E = 7.8 \cdot 10^6 \text{ psi}, \quad \nu = 0.3 \tag{17}$$

subjected to uniform transverse pressure is analyzed. Using the load parameter $\overline{P} = q_0 \cdot a^4 / (E_2 h^4)$, the incremental load vector is chosen to be:

$$\{\Delta P\} = \{6.25, 6.25, 12.5, 25.0, 25.0, 25.0, 25.0, 25.0, 25.0, 25.0\} \cdot \overline{P} \tag{18}$$

with convergence tolerance $\varepsilon = 0.01$ and acceleration parameter $\gamma = 0{,}8$. The displacements and stresses are given in following nondimensional form:

$$\overline{w} = w_0 \cdot E_2 h^3 / (q_0 \cdot a^4), \quad \overline{\sigma}_{xx} = \sigma_{xx} \cdot (a/h)^2 \cdot 1/E \tag{19}$$
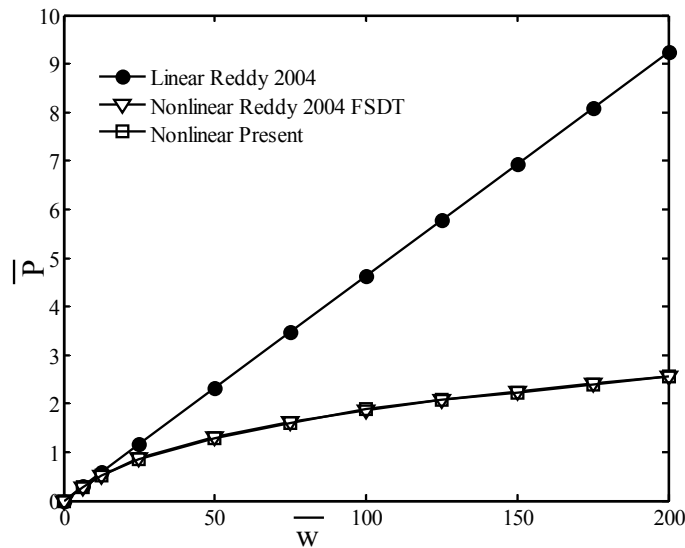

Figure 2. Nonlinear bending of square simply supported (SS1) isotropic plate with
$a/h = 10$; central displacement versus load parameter

A 3x3 quarter plate laminated GLPT model is compared with 4x4 quadratic FSDT model [3]. The results for linear and nonlinear deflections are presented on Figure 2. It is shown that proposed GLPT model closely agree with FSDT model. The Figure 2 also demonstrates the physical nature of geometrically nonlinear response. The study has proved that depending of applied load level, the plate goes from the state of pure bending, at small

displacement ($w \leq 0.30h$) to the phase of bending-stretching coupling, at large displacements. Namely, when the lateral displacement reaches approximately one half of plate thickness ($w \approx 0.5.h$), they take part in stretching, together with bending of the plate middle surface (nonlinear terms in Eq.(2)). This activates the tensile forces, thus enlarging the stiffness of the plates, and reducing displacements and stresses from the values predicted by linear theory. This may be the reason why this phenomena is also known as "plate stiffening" or "stress relaxation". Moreover, the activation of tensile forces in laminated composite plates is of utmost importance, due to their high available specific tensile strength.

Example 4.2. A nonlinear bending of square simply supported (SS1), orthotropic plate made of high modulus glass-epoxy fiber reinforced material:

$$E_1/E_2 = 25, G_{12}/E_2 = 0.5, G_{13}/E_2 = 0.5, G_{23}/E_2 = 0.2, \quad \nu_{12} = \nu_{13} = \nu_{23} = 0.25$$

(20)

subjected to uniform transverse pressure is analyzed. Using the load parameter $\overline{P} = q_0 \cdot a^4/(E_2 h^4)$, the incremental load vector is chosen to be:

$$\{\Delta P\} = \{10, 20, 30, 40, 50, 60, 70, 80, 90, 100, 110, 120, 130, 140\} \cdot \overline{P}$$

(21)

with convergence tolerance $\varepsilon = 0.01$ and acceleration parameter $\gamma = 0,3$. The displacements and stresses are given in following nondimensional form:

$$\overline{w} = w_0 \cdot E_2 h^3/(q_0 \cdot a^4)$$

$$(\overline{\sigma}_{xx}, \overline{\sigma}_{yy}, \overline{\tau}_{xy}) = (\sigma_{xx}, \sigma_{yy}, \tau_{xy}) \cdot \left(\frac{h}{a}\right)^2 \cdot \frac{1}{E_2}, \quad \overline{\tau}_{xz} = \tau_{xz} \cdot \frac{h}{a} \cdot \frac{1}{E_2}$$
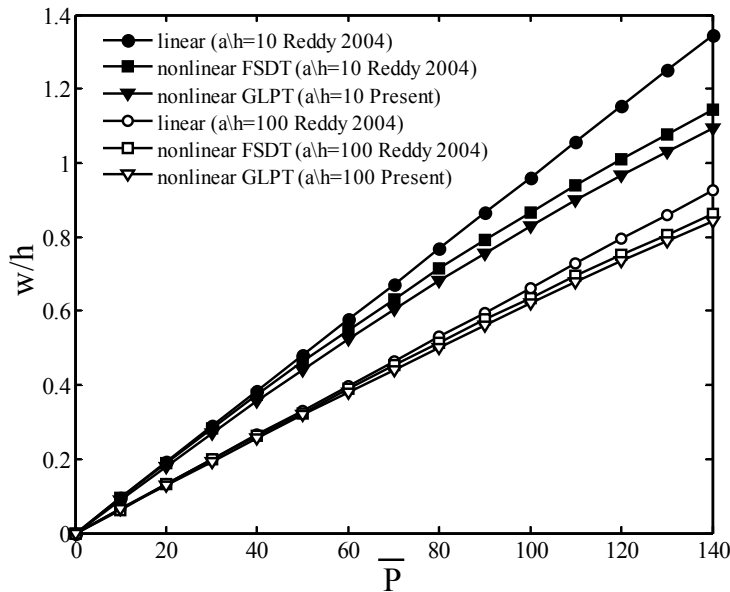
(22)[1,2]

Figure 3. Nonlinear bending of square simply supported (SS1) orthotropic plate; central displacement versus load parameter

A 2x2 quarter plate laminated GLPT model is compared with 8x8 CPT nonconforming and 4x4 quadratic FSDT models [4]. The results for thick and thin plates (a/h=10 and a/h=100) of linear and nonlinear deflections are presented on Figure 3. It is shown that proposed GLPT model closely agree with CLPT and FSDT models. The more significant difference between linear and nonlinear solutions is observed for thick plates, while in thick plates larger lateral deflections have greater influence on nonlinear response, as it can be seen from the underlined nonlinear terms in Eq. (2).

Example 4.3. A nonlinear bending of square cross ply 0/90 and angle ply 45/-45 plates, with $a = b = 1$ and $h = 0.1$, with three different boundary conditions (SS, HH and CC, Eqs. 12, 13, 14), made of material:

$$E_1/E_2 = 40, G_{12}/E_2 = 0.6, G_{13}/E_2 = 0.6, G_{23}/E_2 = 0.5, \nu_{12} = \nu_{13} = \nu_{23} = 0.25 \quad (23)$$

subjected to uniform transverse pressure $\overline{q} = q(x,y) \cdot \left(\dfrac{a}{h}\right)^4 \cdot \dfrac{1}{E_2}$ are analyzed. The incremental load vector is:

$$\{\Delta\overline{q}\} = \{-100, -20, -20, -20, -20, 40, 20, 20, 20, 20\} \quad (24)$$

with convergence tolerance $\varepsilon = 0.01$ and acceleration parameter $\gamma = 0,5$. The displacements and stresses are given in following nondimensional form:

$$\overline{w}_{LIN} = w \times \frac{h^3}{a^4} \frac{E_2}{q} \cdot 100, \quad (\overline{\sigma}_{xx}, \overline{\sigma}_{yy}) = (\sigma_{xx}, \sigma_{yy}) \times \left(\frac{a}{h}\right)^2 \cdot \frac{1}{E_2} \quad (25)$$
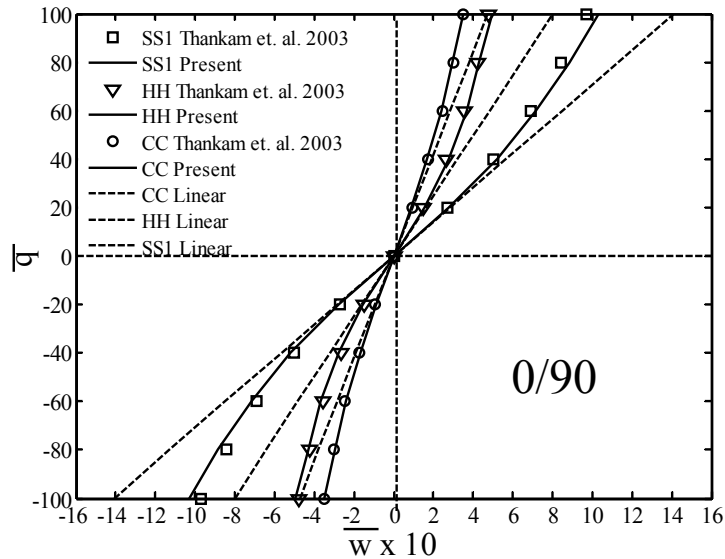
Figure 4. Nonlinear bending of square cross ply 0/90 plate with different boundary conditions and $a/h = 10$; central displacement versus load parameter
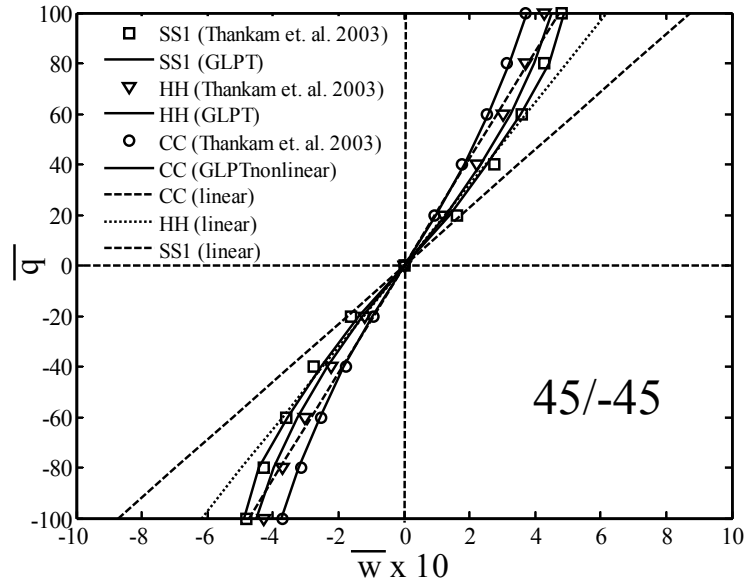

Figure 5. Nonlinear bending of square angle ply 45/-45 plate with different boundary conditions and $a/h = 10$; central displacement versus load parameter

A 2x2 quarter plate and 4x4 full plate laminated GLPT models are analyzed and compared with full 8x8 plate FSDT models (Thankam and Singh and Rao and Rath, A.K. 2003 [10]). The results for linear and nonlinear deflections are presented in Figures 4,5. It is shown that proposed GLPT model closely agree with FSDT model form literature, with the faster convergence. Also, the discrepancy between linear and nonlinear solutions are larger for flexible plates, which are the plates with simply supported boundary conditions, compared to hinged (HH) and clamped (CC) boundary conditions. The study has verified that the change in load direction gives symmetrical displacement field.

Example 4.4. A nonlinear bending of square simply supported (SS1) general quasi-isotropic $(0/45/-45/90)_s$, laminated plate with $a = b = 1$ and $h = 0.1$, made of material:

$$E_1/E_2 = 40, \ G_{12}/E_2 = 0.6, \ G_{13}/E_2 = 0.6, \ G_{23}/E_2 = 0.5, \ \nu_{12} = \nu_{13} = \nu_{23} = 0.25 \quad (26)$$

subjected to uniform transverse pressure is analyzed. Using the load parameter $\overline{P} = q_0 \cdot a^4 /(E_2 h^4)$, the incremental load vector is chosen to be:

$$\{\Delta q\} = \{50, 50, 50, 50, 50\} \cdot \overline{P} \quad (27)$$

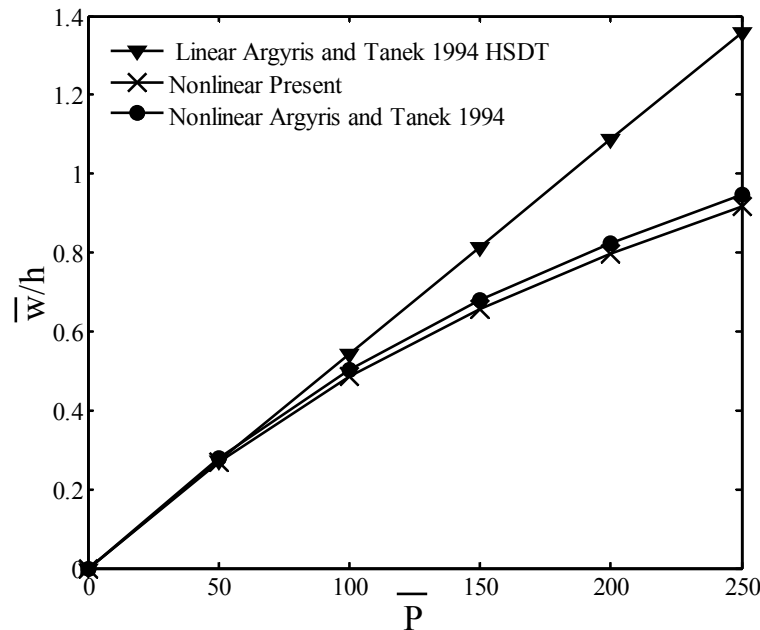with convergence tolerance $\varepsilon = 0.01$ and acceleration parameter $\gamma = 0,8$.

Figure 6. Nonlinear bending of square simply supported (SS1) general quasi-isotropic
$(0/45/-45/90)_s$ laminated plate with $a/h = 10$;
central displacement versus load parameter

A 2x2 quarter plate continuum GLPT model is compared with 8x8 full plate HSDT model [11]. The results for linear and nonlinear deflections are presented in Figure 6. It is shown that proposed GLPT model closely agree with HSDT model form literature, with the faster convergence.

5. Conclusion

In this paper a laminated layerwise finite element model for geometrically nonlinear small strain, large deflection analysis of laminated composite plates is derived using the PVD. The accuracy of the model is verified calculating nonlinear response of plates with different mechanical properties, which are isotropic, orthotropic and anisotropic (cross ply and angle ply), different plate thickness, different boundary conditions and different load direction (unloading/loading). In despite of its mathematical complexity, proposed model has shown better convergence characteristics than ESL models of CLPT, FDST and HSDT, still with less computational cost than 3D elasticity model. Moreover, present model has no shear locking problems, compared to ESL models, or aspect ratio problems, as the 3D finite element may have when analyzing thin plate behavior. The analysis has also shown that the discrepancy of nonlinear from linear response is greater for flexible plates, such as thick compared to thin plates, or plates with SS compared to hinged (HH) and clamped (CC)

boundary conditions. It is verified that the change of load direction (unloading/loading) gives symmetrical displacement field.

6. References

[1] Reddy JN, Barbero EJ, Teply JL. (1989), A plate bending element based on a generalized laminated plate theory, *International Journal for Numerical Methods in Engineering,* **28**, pp. 2275-2292

[2] Ćetković M, Vuksanović Dj (2009),, Bending, Free Vibrations and Buckling of Laminated Composite and Sandwich Plates Using a Layerwise Displacement Model, *Composite Structures*, **88**(2) pp. 219-227

[3] Reddy, J.N. (2004), Mechanics of laminated composite plates-theory and analysis, CRC press.

[4] Polat, C. and Ulucan, Z. (2007), "Geometrically non-linear analysis of axisymmetric plates and shells", *International Journal of Science and Technology*, **2**(1), pp. 33-40.

[5] Zhang, Y.X. and Kim, K.S. (2006), "Geometrically nonlinear analysis of laminated composite plates by two new displacement-based quadrilateral plate elements", *Composite Structures*, **72**, pp. 301-310.

[6] Zhang, Y. and Wang, S. and Petersson, B. (2003) "Large deflection analysis of composite laminates*", Journal of Materials Processing Technology*, 138, pp. 34-40.

[7] Tanriover, H. and Senocak, E. (2004), "Large deflection analysis of unsymmetrically laminated composite plates: analytical-numerical type approach", *International Journal of Non-linear Mechanics*, **39**, pp. 1385-1392.

[8] Reddy, J.N. and Chao, W.C. (1983), "Nonlinear bending of bimodular-material plates", *International Journal of Solids and Structures*, **19**(3), pp. 229-237.

[9] Vuksanović Dj. (2000), "Linear analysis of laminated composite plates using single layer higher-order discrete models", *Composite Structures*, **48**, pp. 205-211.

[10] Thankam, V.S. and Singh, G. and Rao, G.V. and Rath, A.K. (2003), "Shear flexible element based on coupled displacement field for large deflection analysis of laminated plates", *Computers and Structures*, **81**, 309-320.

[11] Argyris, J. and Tanek, L. (1994), "Linear and geometrically nonlinear bending of isotropic and multilayered composite plates by the natural mode method", *Computer methods in applied mechanics and engineering*, **113**, 207-251.

[12] Ćetković, M. (2005), *Application of finite element method on generalized laminated plate theory*, Master Thesis, in serbian, Faculty of Civil Engineering in Belgrade, Serbia.

[13] Ćetković, M. (2011), *Nelinearno ponasanje laminatnih kompozitnih ploca,* Doktorska disertacija, Građevinski fakultet u Beogradu, Srbija

ONE METHOD OF NON-CONTACT SHAFT TORQUE MEASUREMENT

Jovo Dautović [1], Vojkan Madić [2], Sonja Đurković [3]

[1] Technical Test Center, Belgrade,
Vojvode Stepe br. 445, R. Beograd, R. Srbija
e-mail: jovodaut@gmail.com
[2] Technical Test Center, Belgrade,
Vojvode Stepe br. 445, Belgrade, R. Srbija
E-MAIL: vmadic@gmail.com
[3] D. O. O. „Utva A.I." Avio indastry,
 Pančevo, Jabučki put br. bb, 26000 Pančev, R. Srbija
E-MAIL: svskom@scnet.rs

Abstract. In this paper torque shaft measurement using strain gages and non-contact transfer of the measurement signal is presented. The preparation, installation and calibration of measuring chain are also shown. This method is important because of possibility measuring torque during engine working in real condition. Based on measured torque, the power transferred from the rotating shaft is calculated, i.e. the consumer absorbed power. At the end, the proper choice of engine for given consumer or proper choice of consumer for given engine is proposed (in this paper the example of propeller choice for given engine is proposed).
Keywords:strain gages, torque, shaft power, absorbed power

1. Introduction

Development of measurement techniques of the first D'Arsonval instrument to modern electronic measuring instruments with complex treatment based on digital techniques and using special sensors and circuits of high integration has lasted for more than a hundred years [1]. However, the remarkable development of electronics in the last twenty years has brought significant changes in the approach to measurement at all in the technique.

The development of measuring methods, measuring methods and instruments as well as a science of measurement – metrology - were constantly perfected and used the new opportunities offered by the development of electrical engineering. The first electric instruments were electromechanical devices that measure the force between electric and magnetic load, or force between the conductors through which current flows and magnetic fields. Soon after the discovery of electronic tubes and measuring instruments are becoming more diverse, more sensitive and easier to apply, although structurally complex. Discovery of semiconductor elements that make the new size measurement technique, especially in electronics. Finally, the technique of integrated and highly integrated electronic circuits have become high automotive and complex processing of measurement results has become easy in practice due to the application of microprocessor in the measuring instrumentation.

2. Mechanical stress

Solids are deformed under the influence of external forces, molecular forces that hold the molecules of material on specific distances tend to prevent and limit the deformation and material stress.

Stress of the solid material can be varied depending on how the force acting on the body: normal σ, when the force acting normal to the surface of the body (tension, compression, bending), and tangentially τ, when the force in the respect the body section has a tangential direction (shear and torsional stress or twisting and buckling). By its nature, torsional stresses are shear stresses and the difference is only in the manner of their occurrence [2].

The resistance of the material, or force per unit area is called the stress. As a measure of deformation due to forces or stresses introduced the notion of relative deformation, which is the ratio of the shrinkage and the original dimensions. Stress in the material is determined from the measured strains by using Hooke's Law. In elastic body stress is proportional to the relative deformation.

The shaft is twisted under the acting of forces which planes are perpendicular to the longitudinal axis of the shaft. At torsion, stresses are called the shear stresses. The shaft is twisted around the longitudinal axis, and the strain appears as a shift-slide, rotating about the longitudinal axis of individual cross sections to one another. Shaft as a carrier of rotating element transmits the torque and therefore is exposed to twisting. Torsional stress is in proportion to moment. Torsional stress is determined indirectly by measuring strain along the direction of main stresses.

3. Strain gages measurement

The most common method of non-electrical values measuring is by using eletrical conductor.

The measurement is indirect and consists of from converting the measured value (in mechanical engenering non-electrical values are the most common) in the electrical value which is then compared with known electrical value. Measurement system includes the sensor - transmission system - measuring bridge, and contemporary measuring systems have A/D converter and a computer as part of the measuring system [3].

Sensors are an important part of the electrical measuring system and   in practice there are two groups of sensors - active and passive.

The most important characteristics of passive sensors are:
- powered by electrical energy,
- change of measuring values causes change of electrical values
- do not affect to the energy state of the object,
- complex installations (amplifying bridges) and

- more applicable.

    The most important characteristics of active sensors are:
- produce electromotive force under measuring value influence
- take power from the measuring object,
- require precise measuring instruments and
- less applicable.

Type of passive transducer that has been used are strain gauges (metal wire), which is applied for linear elongation measurement (stress states, force, torque).

Characteristics of strain gauges [4] are: very widely used for measuring the stress state as an independent, and as elements of force, torque, pressure sensors.

For measuring the strain, strain gauges which are mounted in the direction of maximum strain are used. For twisted shaft strain gages are placed at an 45° angle to the shaft main axes and measure elongation ε [5].

Strain gage is a passive resistive sensor of mechanical deformation, whose operation is based on the fact that the electrical resistance of the conductor changes when it is exposed to the elastic deformation. The most common strain gauges are in the form of foil, where is the resistive material applied to the plastic carrier which is bonded on the measurement place.

Torque is the ratio of power measured at the shaft and shaft revolution number:

$$M = \frac{P}{2 \cdot \pi \cdot n},$$

where are:

$M -$ torque $\left[\mathrm{N} / \mathrm{m} \right]$;

$P -$ shaft power $\left[\mathrm{W} \right]$;

$n -$ shaft revolution number [s⁻¹]

Shaft power is power that the engine deliver to the consumer or absorbed power of consumer.

3.1. Strain gages

Strain gages are the most common electrical resistance sensors which are applied or independently for elongation measurement, or like active elements of various sensors [6]. The principle of measuring is based on the effect that mechanical stress causes change in an electrical resistance of conductor. The most common types of strain gages are shown at Figure 1.

Strain gauges resistance is changed in function of elongation according to:

$$\frac{\Delta R}{R} = K \frac{\Delta l}{l} = K\varepsilon \,,$$

where are:

$\dfrac{\Delta R}{R}$ – relative change of resistance,

$\dfrac{\Delta l}{l} = \varepsilon$ – relative elongation of strain gages
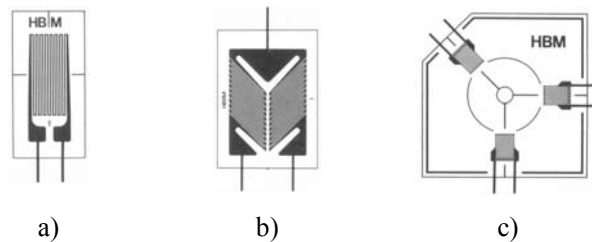
$K - K$ factor of strain gauge.

Figure 1. Strain gauges a) for linear elongations measurement, b) for torque measurement c) for elongation measurement on surface were main stresses directions are unknown

K factor is the sensitivity of strain gauges, which is the most important characteristic of its, and producer declares it for each strain gages. Usually its value for the strain gages with a metal-resistant element ranges from 1.8 to 2.5.

Strain gages are made of metal resistance element (wire and cellophane) and semiconductor elements. Own resistance of strain gauges are 120 Ω, 350 Ω, 700 Ω or 1000 Ω. It is desirable that the measuring bridge used strain gages as much as possible of their own resistance to obtain higher output signal [6,7].

Strain gauges in the Wheatstone bridge can have multiple roles as follows:
- active strain gages – strain gages bonded to the measuring object whose deformation is measured,
- passive strain gages – strain gages as added resistance and serve to complete a branch of the bridge and
- compensation strain gages – strain gages that are designed for temperature compensation of the active strain gauges.

Since the strain gages are considered like external resistances there are the following ways of connecting the strain gages in the Wheatstone bridge [6]:

- full bridge connection: all resistances are external and consist of active, passive or compensation strain gages,

- half bridge connection: two resistances are external (strain gauges), and two internal (inside the measuring-bridge amplifier) and

- quarter bridge connection: one external resistance (active strain gauge) and three internal resistances.

4. Testing

4.1. Measuring instruments

Measurement of consumers absorbed power is done with the acquisition measurement systems. In this paper acquisition measurement system of the German manufacturer HBM (Figure 2) is shown and it consists of:

- measuring amplifier SPIDER8 (item 1);
- PC notebook for data collection and visualization (item 2);
- carrier of signal transmitter and battery unit (item 3);
- a system for non-contact signal transmission BLM, which consist of a transmitter signal (item 5) and signal receiver (item 4);
- battery unit (item 6);
- photo-sensitive sensor of shaft revolution number (item 7);
- strain gauges HBM producer Type: 6/350XY21, connected in a Wheanstone bridge circuit (item 8).
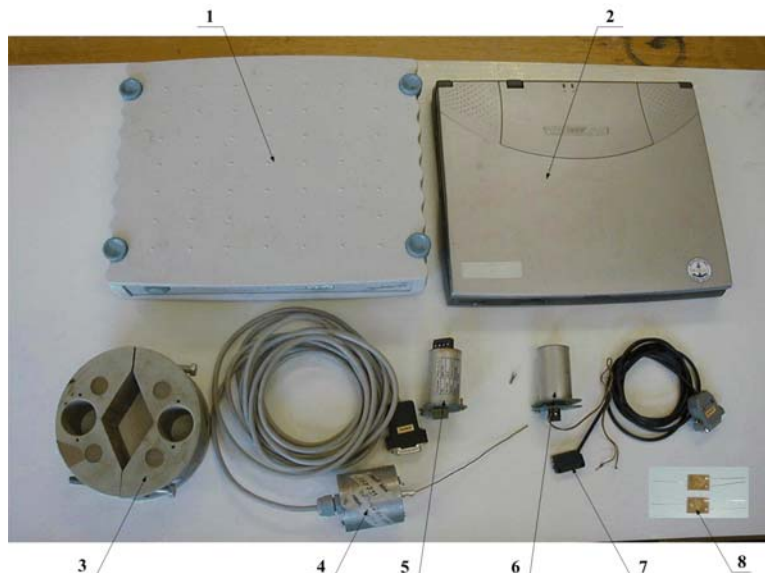
Figure 2. Acquisition measurement system for torque measuring

Battery unit is used for power supply of strain gages, and non-contact measuring system type BLM, produced by TRC from Petrovaradin [8] is used for signal transmission. Non-contact measuring system type BLM consists of transmitter and receiver signal. Voltage signal from the receiver transmit to the amplifier SPIDER-8 produced by German company HBM, which is connected to the PC notebook. Software module for measurement and data processing is CATMAN 3.1, produced by HBM, which operates in Windows XP environment.

For shaft revolution number measurement photo-sensitive sensor is used, whose signal is transmitted to the measuring amplifier SPIDER-8.

4.2. Measuring conditions

The measurement is performed during operating conditions. Loading condition of consumers depends of the needs of measurement.

4.3. Measurement process

4.3.1. Preparatory works

Preparatory works for measurement carrying out (Fig. 3) are follows:
- strain gauges mounting,
- transmitter signal and battery unit mounting,
- checking of strain gauges correct mounting,
- strain gauges electrical connecting in Wheastone bridge circuit and connecting with signal transmitter,
- transmitter signal and battery unit electrical connecting,
- receiver signal mounting,
- shaft revolution number photo-sensitive sensor mounting,
- calculate preparation for measurement and
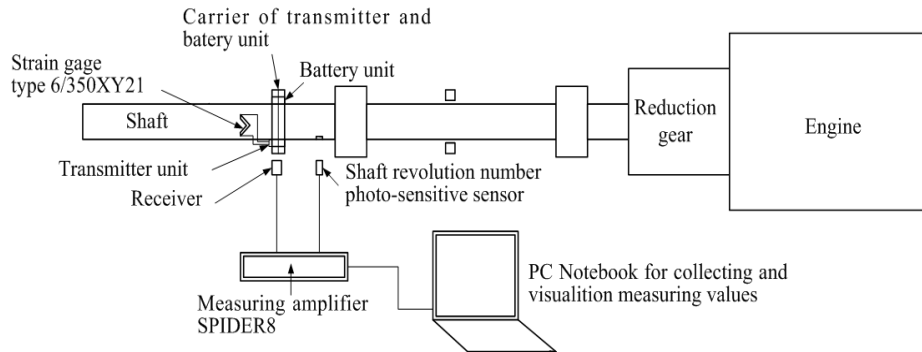- calibration of the system.

Figure 3. Schematic of measurement configuration mounted on the shaft

4.3.2. Strain gauges mounting

Strain gauges are mounted on the free part of the propeller shaft symmetrically arranged around the edges (Figure 4).

Mounting includes the following:
- preparation of two strain gauges type 6/350HY (X rossets),
- measuring place surface preparation,
- strain gauges fixing by special glue,
- preparation of soldering terminal and strain gauges wires
- cables connecting.

All actions are performed according to the strain gages producer introduction : "An Introduction to Measurements using Strain Gages" .
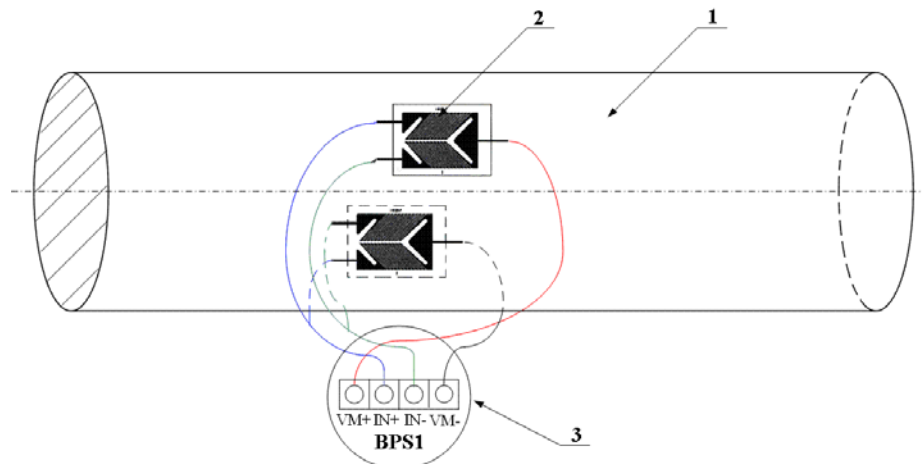

Figure 4. Gaging and connecting the transmitter signal:
1 – propeller shaft, 2 – measuring tape, 3 – transmitter signal

After strain gages mounting their protection are done. Protection, if it is possible, is done immediately after strain gages fixing.

The protection is done by applying a protective kit AK 22 and AVM75. Surface around the strain gages must be clean.

4.3.3 Signal transmitter and battery unit mounting

Signal transmitter and battery unit carrier (Figure 5, item 3) is mounted on the shaft close to the strain gages.
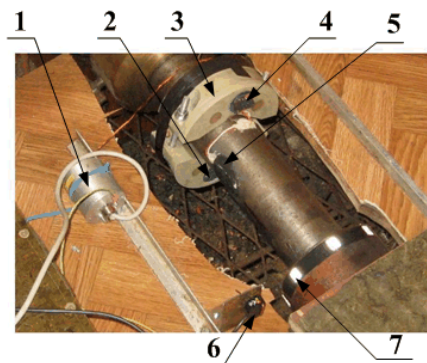

Figure 5. Strain gauges and carrier mounted on the shaft:
1 – signal receiver, 2 – battery unit, 3 –signal transmitters and battery units carrier, 4 – signal transmitter; 5 – strain gage covered with a protective coating; 6 – photo sensitive sensor of shaft revolution number, 7- markers at the shaft

4.3.4. Checking of mounted strain gauges

It is necessary to perform two types of checks:

a) Visual test

The application is checked using magnifying glass to detect the following defects generated by strain gages fixing and soldering:
- air bubbles (can be identified by a light-colored surfaces or channels) or particles under the strain gauges net,
- lack of built-in glue, at the strain gauges ends,
- poorly soldered joints at the ends of cables and
- remains of solder.

b) Electrical test

After installation is done check the strain gauges resistance with a digital multimeter:

- insulation resistance strain gauges should be greater than 10 GΩ at test voltage 20V and
- on the diagonal of the bridge resistance value should be 350 Ω ±0.35%, and the resistance of any branch of the bridge should be 262.5 Ω ± 0.35%.

4.3.5. Electrical connection of strain gauges in Wheatstone bridge and connecting to transmitter signal

Connecting is carried out in accordance with the scheme in Figure 4.

4.3.6. Electrical connection of the transmitter signal and battery unit

Signal transmitter antenna is solid piece of copper wire which is mounted on the transmitter antenna connector (marked as ANT) and is coiled up 2 to 3 laps around the transmitter and battery unit carrier. After mounting signal transmitter is connected with battery unit.

4.3.7. Signal receiver mounting

Signal receiver is mounted at the hull structure. Receiving antenna is located 3 to 5 cm from the signal transmitting antenna (Figure 5, item 1).

4.3.8. Mounting the photo-sensitive sensor of shaft revolution number

Photo-sensitive sensor is mounted at the hull structure (Fig. 5, Pos. 6) and connected to channels 1 or 2 of amplifier SPIDER-8. Sensor is mounted between 3 to 5 cm from the shaft and the shaft is wrapped with black sticky tape with required number of bright labels, „marker" attached on it (Fig. 5, Pos. 7).

4.3.9. Computational preparation for measurement

Computational preparation for measurement involves collecting data about engine and shaft. The information that is necessary to collect are:

P − Nominal motor power $[\mathrm{kW}]$,

n − nominal shaft revolution number $\left[\mathrm{min}^{-1}\right]$,

d − diameter shaft $[\mathrm{mm}]$,

E − Young 's modulus of shaft elasticity $\left[\mathrm{N}/\mathrm{mm}^2\right]$ and

G − shear modulus of material $\left[\mathrm{N}/\mathrm{mm}^2\right]$.

The values for these parameters are entered into the form for calculating torque transducer in the XLS file.

4.3.10. Calibration system

Calibration of the system is done by shunt resistance. Shunt resistance is connected to the transmitter terminals VM - IN- or VM + IN + (Fig. 4, Pos. 3). The measured values are entered in the form of the calibration system with a parallel resistor.

4.4. Measurements performing

Software module CATMAN 3.1 is used for measurement and data processing, according to the instructions „User's Manual for Windows 95/98/N". Torque and shaft revolution number are directly measured.

Measurement is performed at defined rpm in the range from idling to 100% engine power. Time recording signals should be in the range of 5 to 10 seconds.

Data is automatically stored on a PC notebook for data collection and visualization [10]. Shaft power, ie. absorbed power of consumers, is calculated based on measured values according to the formula:

$$P = \frac{2 \cdot \pi \cdot n}{60} \cdot M \cdot i \text{ [W]},$$

where are:

$M -$ torque $\left[\text{N} / \text{m} \right]$,

$n -$ shaft rotating speed $\left[\text{min}^{-1} \right]$

$i -$ gear transmission ratio.

For the purposes of torque and torsional vibration measurement and practice in the laboratory of the Technical Testing Center, according to the design by Mr. Jovo Dautović, BSc. Eng., is made the model. Model is shown in Figure 6.
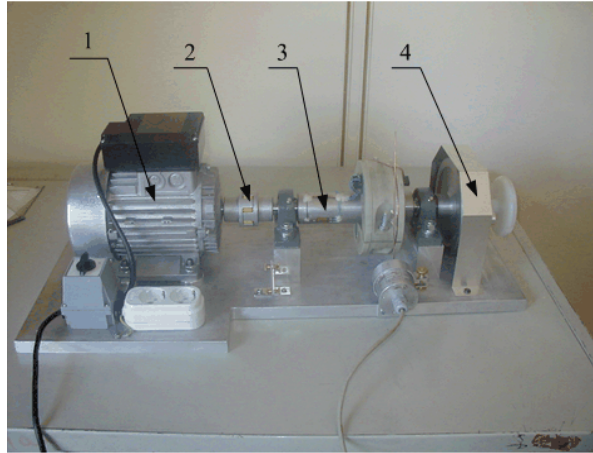
Figure 6. Model for training and practice:
1 – Electromotor; 2 - flexible coupling; 3 - shaft, 4 – brake

Electromotor is loaded with brake. Brake consists of disk and brake mechanism with which it is possible to change load. Purpose of this model is training of strain gage fixing, other equipment mounting and measuring process.

In Figure 7 is shown model with installed measurement equipment.

The measurement was made by loading gradually increasing. During measurement shaft revolution number and torque was measured. Time recording signals should be in the range of 5 to 10 seconds.

Figure 7. Model with installed equipment for measurement:
1 - model; 2 – shaft rotating speed sensor, 3 - strain gauge; 4 - signal transmitter and battery unit carrier; 5 –
measuring amplifier SPIDER 8; 6 – signal receiver; 7 - notebook.

Data is automatically stored on a PC notebook for data collection and visualization. [10].

4.5. Analysis of measurement results

The analysis includes a drawing diagram of shaft power (consumer absorbed power) as a function of shaft revolution number and estimation about consumer or engine choice regularity. Shaft power diagram is compared with the diagram of engine power on the test bench.

In this paper power measurement results on model and ship propeller shafts are shown.

Comparing the diagram of shaft power and a diagram of engine power on the test bench it can be concluded:

- engine condition according which it can be decided about engine overhaul beginning

- compatibility engine and propeller (preferably after replacing engine or propeller) and

- Overhaul performance (very important in a situation where there isn't enough great test bench for large marine engines in our country).

Torque and power measurement is crucial because without delay in ship operation valuable information is received. This information and some other measurement can be used for reach conclusion about general condition of engine.

The measurement results on the model are shown in Figure 8. It is shown a torque-shaft revolution number diagram.
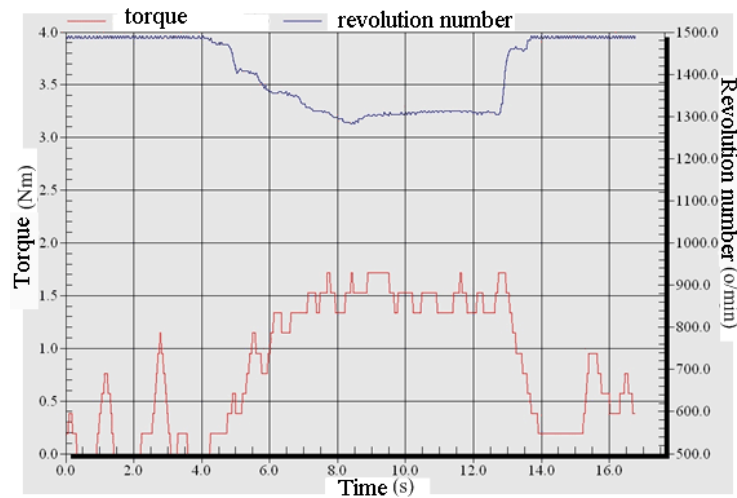

Figure 8. Torque-shaft revolution number diagram

Figure shows that shaft revolution number decreasing and shaft torque increasing with increasing of electro-motor load because of electro-motor has not possibility of revolution number regulation.

Figure 9 shows the diagram obtained by measuring the power of the left main engine on warship RTOP-404 performed by the Naval Test Center.
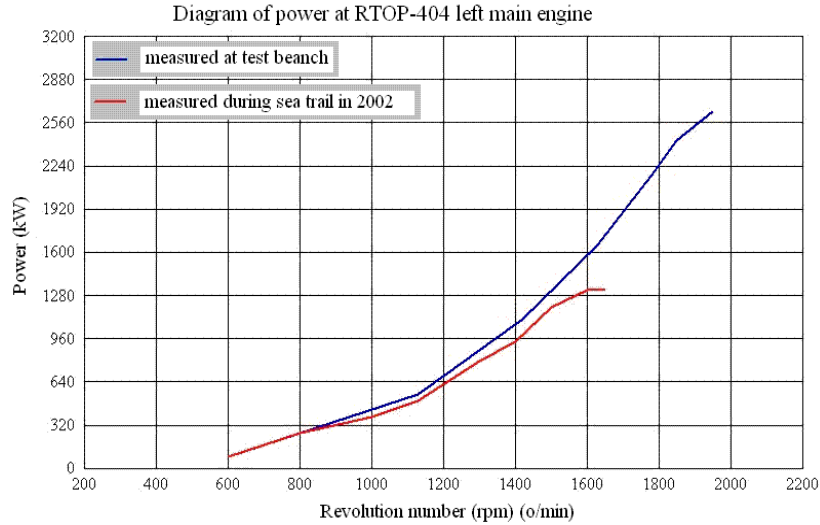
Figure 9. Comparative diagram of the engine power measured on the test bench and power measured during sea trail at RTOP-404

By comparing the curves it can be concluded that the diesel engine after 23 years of work and around 3,800 operating hours can not achieve more than 1650 min^{-1} and it's power on that rpm is lower approximately 15% than designed power.

Figure 10 shows the diagram obtained by measuring the power of the left and right shaft on ship ISTRAJNI performed by the Technical Test Center.
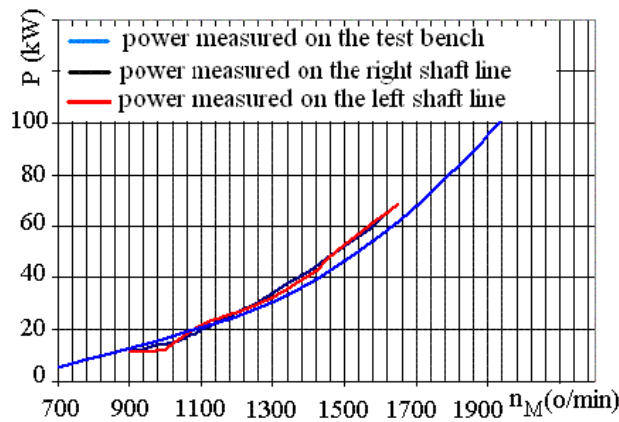

Figure 10. Comparative diagram of the engine power measured on the test bench and power measured during sea trail at Iatrajni

In an ideal condition propeller absorbs 100% of engine power at maximum RPM. In

practice it is acceptable that propeller absorbs 100% of engine power at shaft rotating speed lower than maximal, up to 95% of it. (Propeller Handbook – The Complete Reference for Choosing, Installing and Understanding Boat Propellers).

If the propeller absorbs 100% of engine power at shaft rotating speed lower than 95% of the maximal, propellers are not appropriate for a ship, i.e. there are too heavy. The diagram shows the engine power measured on the test bench and power measured at the ship propeller shaft.

Comparing measured absorbed power of the propeller and engine power measured on the test bench, it is evident that at the engine revolution number 1650 min^{-1} propeller absorbs 107.8% of the engine power, measured on the test bench.

It can be concluded that on 1650 min^{-1} engine run overloaded. The propeller absorbed power is too high, ie. propellers are „too heavy" for the engine.

5. Conclusion

This paper shows that the non-contact method of measuring torque, ie. shaft power; allow successful measuring power absorbed by the consumer during the exploitation of the engine. Based on this fact it can be concluded about correct consumer choice for given engine.

6. References

[1] V. Mamula, Mjerenja u elektronici, SSNO, RM-1669, Split, 1986.

[2] T. Nikolić, Otpornost materijala, CENERG, Zrenjanin, 1995.

[3] Ž. Adamović, Tehnička dijagnostika u mašinstvu, Privredni pregled, Beograd, 1986.

[4] HBM - An Introduction to Measurements using Strain Gages.

[5] HBM - catman 3.1, User's Manual for Windows 95/98/NT.

[6] S. Muždeka, Merenje neelektričnih veličina električnim putem, Ministarstvo odbrane, Sektor za ljudske resurse, Uprava za školstvo, Vojna akademija, Beograd, 2006.

[7] Propeller Handbook – The Complete Reference for Choosing, Installing and Understanding Boat Propellers, Dave Gerr, International Marine.

[8] Janković S., Jovanović M., Đurković P.V.: Tehnička dijagnostika u prediktivnom održavanju složenih tehničkih sistema, VIII međunarodno–stručni skup o dostignućima elektrotehnike, mašinstva i informatike, DEMI 2007, Mašinski fakultet Banja Luka od 25. do 26. maja 2007., p.841–848.

[9] Merenje snage na propelerskim vratilima na brodu „ISTRAJNI-I" - Izveštaj o izvršenoj usluzi merenja, TOC-12-3331;

[10] Uputstvo za merenje obrtnog momenta na propelerskim vratilima broda, TOC, C.33.003.

THE BEHAVIOR OF THE INTERFACIAL CRACK BETWEEN THE TWO LAYERS UNDER CONDITIONS OF A STATIONARY TEMPERATURE FIELD

Jelena M. Djokovic[1]

[1] Technical Faculty of Bor
The University of Belgrade, Vojske Jugoslavije 12, 19210 Bor
e-mail: jelenamdjokovic@gmail.com

Abstract. Thin films, coatings or multi-layer samples, made of different materials, are used for various purposes. When brittle coatings function in the presence of thermal gradients and high heat flux, they are susceptible to delamination. The most widely investigated examples are thermal barrier coatings used in turbines for power generation. In the layers made of different materials, during the temperature loading, as a result of the difference in the thermal expansion coefficients, appear thermal stresses. In this paper is presented the theoretical basis for determining the driving forces of interface fracture in a two-layer bimaterial specimen under conditions when the temperature of the outer surface layers are different. The analysis in this paper is limited to the fact that two-layer bimaterial sample exposed to a stationary temperature field. The driving force of the interfacial fracture in this case is the energy release rate G. The energy release rate is determined depending on the loads of temperature. It was noted that the energy release rate tends to increase with increasing temperature difference. This relationship can be used to predict the maximum temperature differences the two-layer sample can sustain without delamination. For future analysis remains the case when the two-sample bimaterial subjected to unsteady temperature field.

Keywords: Interfacial crack, Thermal stresses, Two-layered sample, Delamination

1. Introduction

Thin films, coatings or multi-layer samples, made of different materials, are used for various purposes. The most common examples of application are the ceramic coatings on the metal substrate, metal layers on the polymer substrate, where the temperature at which these layers are applied is significantly higher than the working temperature; the thermo-insulating coatings like Al_2O_3 on Ni-Cr-Al and Fe-Cr-Al allows, hard transparent coatings on optic polymers, metal fibers on the polymer substrate in electronic modules or the photo-electric actuators.

When brittle coatings function in the presence of thermal gradients and high heat flux, they are susceptible to delamination and spalling. The most widely investigated examples are thermal barrier coatings used in turbines for power generation. Articles that analyze the mechanisms capable of providing sufficient energy release rate to drive delamination have been presented in [1,2]. Thermal barrier coating systems are susceptible to delamination failures in the presence of a large thermal gradient. Three possible causes of internal delamination are analyzed in [3]. Delamination of coatings initiated by small cracks

paralleling the free surface are investigated in [4] under conditions of high thermal flux associated with a through-thickness temperature gradient.

In the layers made of different materials, during the environmental temperature change, as a result of the difference in the thermal expansion coefficients, appear thermal stresses. Those stresses are causing the appearance of an interfacial crack. When such a crack is formed, the energy release rate needed for the crack propagation depends on stresses' intensities in both layers. If one assumes that the layers are made of the elastic isotropic materials, the stresses will depend upon the elastic and thermal characteristics of the layers' materials, as well as on the temperature variations. The driving force of the interfacial fracture in this case is the energy release rate G.

2. Problem formulation

Let $2a$ be the lenght of the crack under plane strain conditions, which is located at a distance H_1 from the upper surface and at a distance H_2 from the bottom surface of infinity two-layer plate of thickness $H=H_1+H_2$, as shown in Figure 1.
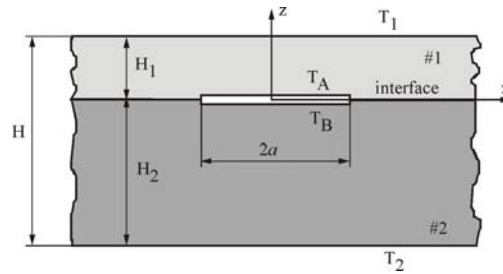

Figure 1. Two-layer sample with crack under thermal loading.

The upper surface of the sample is exposed to a uniform temperature T_1 and lower surface to temperature T_2. This means that the crack is opened. Heat flow across the surface crack at any point satisfies the equation:

$$q_z = h_c(T_B - T_A),\tag{1}$$

where $T_A = T(x, 0^+)$, $T_B = T(x, 0^-)$ and h_c is the conductivity across the interface. The conductivity depends on the heat conduction mechanisms across the crack and will depend on the crack opening. Here will be made the assumption that h_c is constant along the crack. Thuse, h_c should be average quantity. With k_z as thermal conductivity of the body in the z direction, the temperature gradient of each surface cracks must satisfy the equation $-k_z \partial T / \partial z = q_z$. Two-layer sample has homogeneous characteristics and be orthotropic in relation to the axis (x, y, z). The stress-strain equations for the given problem are:

$$\varepsilon_{xx} = \frac{1}{E_x}\sigma_{xx} - \frac{\nu_{xy}}{E_y}\sigma_{yy} - \frac{\nu_{xz}}{E_z}\sigma_{zz} + \alpha_x\Delta T$$

$$\varepsilon_{yy} = -\frac{\nu_{xy}}{E_y}\sigma_{xx} + \frac{1}{E_y}\sigma_{yy} - \frac{\nu_{yz}}{E_z}\sigma_{zz} + \alpha_y\Delta T$$

$$\varepsilon_{zz} = -\frac{\nu_{xz}}{E_z}\sigma_{xx} - \frac{\nu_{yz}}{E_z}\sigma_{yy} + \frac{1}{E_z}\sigma_{zz} + \alpha_z\Delta T$$

$$\varepsilon_{xz} = \frac{1}{2G_{xz}}\sigma_{xz}$$

(2)

where without loss of generality the temperature on the lower surface is taken as a reference such that $\Delta T = T - T_2$.

The problem shown in Figure 1 is discussed under constraint of plane strain, i.e. $\varepsilon_{yy} = 0$. The stress σ_{yy} does not induce any change in the crack tip fields, so for the problem shown in Figure 1, Equations (2) are reduce to:

$$\varepsilon_{xx} = (\frac{1}{E_x} - \frac{\nu_{xy}^2}{E_y})\sigma_{xx} + (\alpha_x + \nu_{xy}\alpha_y)\Delta T \equiv \frac{1}{\overline{E}}\sigma_{xx} - \overline{\alpha}\Delta T .$$

(3)

The idea of analysis is to determine the boundaries for which the crack is long enough such that the temperature and stress distribution ahead of the crack tip depends only on z. By determining the dependence of energy release rate and stress intensity factor can be calculated to the application of the concept of linear elastic fracture mechanics to the interface. In areas of two-layer sample ahead of the crack tip the temperature distribution is linear in z within each layer. In the sample without a crack near to the right of the tip:

$$T = \frac{(T_1 - T_2)z}{H} + \frac{(H_1 T_2 + H_2 T_1)}{H} .$$

(4)

In the area with central crack away from the crack tip:

$$T = \frac{(T_1 - T_A)z}{H_1} + T_A \quad za \quad z > 0$$

$$T = \frac{(T_B - T_2)z}{H_2} + T_B \quad za \quad z < 0$$

(5)

where T_A and T_B are the temperatures at the upper and lower surface of crack. There are:

$$T_A = \frac{T_1(1+\eta) + B_c(T_1 + \eta T_2)}{(1 + B_c)(1+\eta)}$$

$$T_B = \frac{T_2(1+\eta) + B_c(T_1 + \eta T_2)}{(1 + B_c)(1+\eta)}$$

(6)

where $\eta = H_1 / H_2$ and $B_c = Hh_c / k_z$. The temperature jump across the crack is given by:

$$T_A - T_B = \frac{T_1 - T_2}{1 + B_c} \,, \tag{7}$$

such that the heat flow impeded by the crack is $q_z/(1+B_c)$. The dimensionless Biot number, B_c, controls the heat flow through surface crack. When $B_c=0$ the crack is perfectly insulated so that $T_A=T_1$ and $T_B=T_2$. When B_c tends to infinity the crack does not interrupt the heat flow so it is $T_A = T_B = (T_1 + \eta T_2)/(1+\eta)$, and (5) is reducet to (4).

Based on [5] and [8] the energy release rate and stress intensity factors for the problem shown in Figure 1 can be written as:

$$G = \frac{\eta(1+\eta^3)}{2(1+B_c)^2(1+\eta)^5} \overline{E} H [\,\overline{\alpha}(T_1 - T_2)]^2$$

$$K_I = \overline{E}\sqrt{H}\overline{\alpha}(T_1 - T_2)F\sqrt[4]{\lambda}\left[\frac{\cos\omega}{\sqrt{U}} - \frac{\eta^2(1+\eta)}{2(1+\eta^3)}\frac{\sin(\omega+\gamma)}{\sqrt{V}} \right], \tag{8}$$

$$K_{II} = \overline{E}\sqrt{H}\overline{\alpha}(T_1 - T_2)F\left[\frac{\sin\omega}{\sqrt{U}} + \frac{\eta^2(1+\eta)}{2(1+\eta^3)}\frac{\cos(\omega+\gamma)}{\sqrt{V}} \right]$$

where: $F = \dfrac{\sqrt{\lambda}}{\sqrt[4]{2(1+\rho)}}\dfrac{\sqrt{\eta(1+\eta^3)}}{(1+B_c)\sqrt{(1+\eta)^9}}$, $\lambda = \dfrac{E_z}{E_x}$, $\rho = \dfrac{1}{G_{xz}\sqrt{\lambda}} - \nu_{xz}$, $\omega \cong 52.1 - 3\eta \,[\circ]$,

$V = \dfrac{1}{12(1+\Sigma\eta^3)}$, $U = \dfrac{1}{1+\Sigma(4\eta+6\eta^2+3\eta^3)}$ and $\gamma = arcsin(6\Sigma\eta^2(1+\eta)\sqrt{UV})$.

The mode mixity measured the relative size of the Mode II to Mode I and is given by:

$$\psi = arctg\frac{K_{II}}{K_I} = arctg\left[\sqrt[4]{\lambda}\,\frac{2(1+\eta^3)\sqrt{V}\sin\omega + \eta^2(1+\eta)\sqrt{U}\cos(\omega+\gamma)}{2(1+\eta^3)\sqrt{V}\cos\omega - \eta^2(1+\eta)\sqrt{U}\sin(\omega+\gamma)} \right]. \tag{9}$$

In order to eliminate the Biot's number, Bc as an unknown from the equation (8) uses the relationship that exists between the energy release rate, G, and the size of crack opening, δ. The relationship between the energy release rate and size of crack opening for a crack of length $2a$ lying along one of the main axis in an infinite orthotropic body is:

$$\delta = \frac{4n\cos\psi}{\sqrt[4]{\lambda^3}\sqrt{\pi}}\sqrt{\frac{Ga}{E}} \,, \tag{10}$$

where $n = \sqrt{(1+\rho)/2}$. The factor $cos\psi$ reflects the fact that the only component of K_I, the stress intensity factor for Mode I, at the crack tip, influence on the opening. If the sample is isotropic i.e. $\lambda=\rho=1$, and is based on equation (9):

$$B_c = \frac{k_g H}{k_z \delta} = \frac{k_g H\sqrt[4]{\lambda^3}}{4k_z n\cos\psi}\sqrt{\frac{\pi\overline{E}}{Ga}} \,, \tag{11}$$

where k_g the conductivity of the gas. Eliminating B_c in (8) gives the relation between the energy release rate, G and the temperature loading, (T_1-T_2), such as:

$$\left(1+\frac{k_g H \sqrt[4]{\lambda^3}}{4k_z n\cos\psi}\sqrt{\frac{\pi\overline{E}}{Ga}}\right)^2 G = \frac{\eta(1+\eta^3)}{2(1+\eta)^5}\overline{E}H\left[\overline{\alpha}(T_1-T_2)\right]^2 . \tag{12}$$

3. Results and discussion

The energy release rate curves as a function of crack distance from the upper surface of the sample, on the basis of equation (8), and for different values of B_c are shown in Figure 2. Diagrams were obtained with the help of programming package *Mathematica*®, and in case of an isotropic sample.
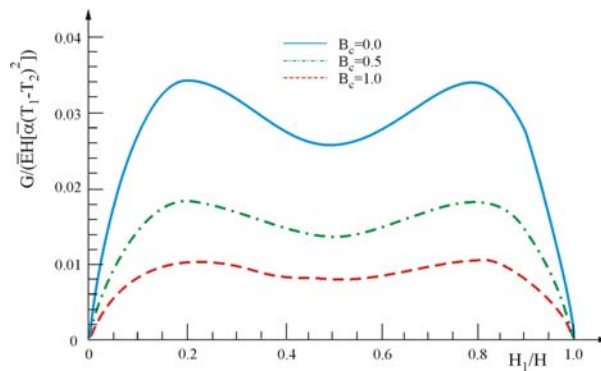

Figure 2. Dependence of the energy release rate of crack distance from the upper surface of the sample for different values of B_c.

Figure 3 shows the results of the mode mixity that does not depend on the Biot's number for $T_1>T_2$.
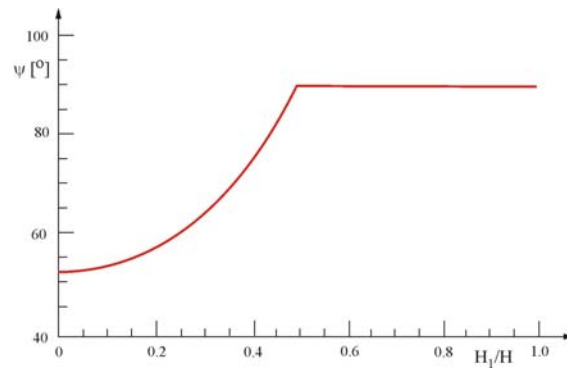

Figure 3. The dependence of the mode mixity to the distance of crack from the upper surface of the sample.

As shown in Figure 3 the crack tip is opened with a positive stress intensity factor for Mode I as long as the crack is above or in the middle of the sample. Crack tip is closed in terms of pure Mode II when the crack is below the mid-thickness of the sample, i.e. when $H_1/H>0.5$. In Figure 2 shows that the highest value of the energy release rate for a crack located at approximately quarter thickness of the sample, ie. for $H_1/H=0.211$, which means that it is likely that at this distance is crack, which causes delamination of the sample.

Figure 4 shows the dependence of the energy release rate, G, of the temperature loading T_1-T_2 for $H_1/H=0.211$, and different values of B_c.
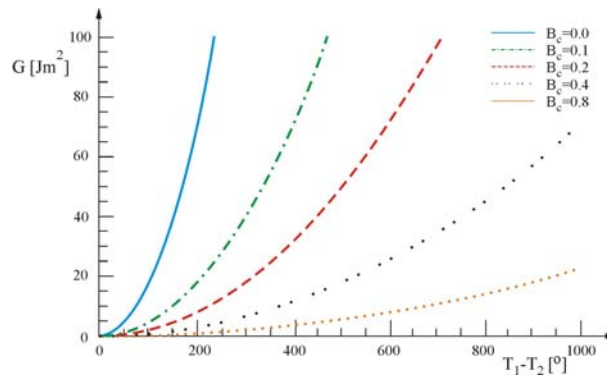

Figure 4. Dependence of the energy release rate of the temperature loading for different values of B_c.

As shown in Figure 4, an important role in heat flow through the crack has Biot's number, B_c. At themperatures below 1500K the dominant mechanism of heat transfer through the crack is due to gaseous transport. Approximate formula for B_c when the size of the crack opening, δ, is larger than 0.1μm, is $B_c = k_z H / k_g \delta$, where k_g gas conductivity. From Figure 4, it follows that for large values of the Biot's the energy release rate, G has a relatively lower value, which means that the crack opening is a small. On the other hand when B_c is small the energy release rate will be large and crack opening will be large, i.e. crack is completely and totally isolated, and as such is suitable for delamination of the sample if the temperature gradient is sufficiently large.

The relationship between the energy release rate and temperature loading is shown in Figure 5, for three different values of k_g for the isotropic sample. The crack length $2a$ is equal to the thickness of the sample H. A surprising feature of these curves is that when one reaches the threshold of T_1-T_2, below which the energy release rate becomes zero, and for a very small increase in the difference T_1-T_2, the energy release rate becomes large very quickly.

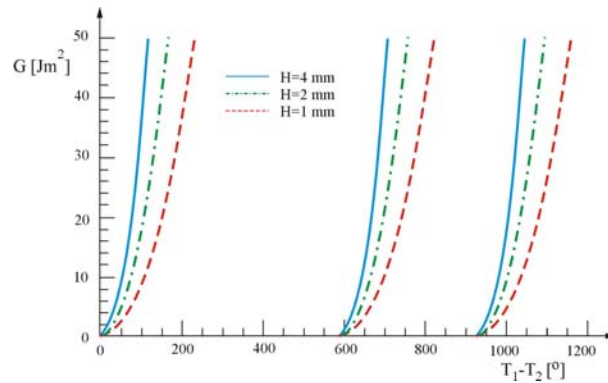**Figure 5**. Dependence of the energy release rate of the temperature loading
for different values of the thickness of the sample.

In Figure 5 shows that with increasing temperature at the crack grows the threshold temperature difference, while k_g increases with temperature. If the threshold exceeds the temperature difference which is exposed to the sample should not be expected delamination of the sample. Heat flow through the cracks, can be significant and the assumption of a perfectly isolated the crack can be wrong. Another loading that caused a significant crack opening and further reduce the heat transfer through the cracks.

4. Conclusion

In this paper is presented the theoretical basis for determining the driving forces of interface fracture in a two-layer bimaterial specimen under conditions when the temperature of the outer surface layers are different. The analysis in this paper is limited to the fact that two-layer bimaterial sample exposed to a stationary temperature field. The driving force of the interfacial fracture in this case is the energy release rate G. The energy release rate is determined depending on the loads of temperature. It was noted that the energy release rate tends to increase with increasing temperature difference. This relationship can be used to predict the maximum temperature differences the two-layer sample can sustain without delamination. For future analysis remains the case when the two-sample bimaterial subjected to unsteady temperature field.

5. References

[1]   Evans, A.G. and J. W. Hutchinson, (1995), The thermo mechanical integrity of thin film and multilayers, *Acta Metall. Mater.*, Vol. **43**, 7, pp. 2507-2530.
[2]   Evans, A.G. and J. W. Hutchinson, (2007), The mechanics of coating delamination in thermal gradients, *Surface&Coatings Technology*, **201**, 18, pp. 179-184.
[3]   Hutchinson, J. W. and A.G. Evans, (2002), On the delamination of thermal barrier coatings in thermal gradients, *Surface&Coatings Technology*, **149**, 2-3, pp. 7905-7916.
[4]   Xue, Z., Evans, A.G., Hutchinson, J.W., (2009), Delamination Susceptibility of coatings under high thermal flux, *J. Appl. Mech.*, **76**, , 4, pp. 1-7.

[5]   Hutchinson, J. W. and Suo Z., (1992), "Mixed mode cracking in layered materials",
       Advances in Applied Mechanics, Vol. **29**, pp. 63-191.
[6]   Dundurs J, (1969), Elastic Interaction of Dislocations with Inhomogeneities,in
       Mathematical Theory of Dislocations, T. Mura ed. ASME, New York, pp. 77-114.
[7]   Rice J.R., (1988), Elastic fracture mechanics concepts for interfacial cracks,
       J.Appl.Mech., vol.**55**, 1, pp. 98 - 103.
[8]   Veljkovic J.M., Nikolic, R.R., (2003), Application of the interface crack concept to
       the problem of a crack between a thin layer and a substrate, *Facta universities*, Vol**.
       3**, pp. 573-581.
[9]   Djokovic J.M., R.R. Nikolic, S.S. Tadic, "Influence of temperature on behavior of the
       interfacial crack between the two layers", *Thermal Science*, Vol. **14** (2010), pp. ,